Defence Research and Development Canada
Recherche et développement pour la défense Canada

DEFENCE R&D DÉFENSE

Polarimetric SAR Interferometry: Investigations using EC CV-580 SAR data

Karim E. Mattar, Chen Liu and Ramin Sabry

Defence R&D Canada – Ottawa
TECHNICAL REPORT
DRDC Ottawa TR 2005-165
March 2005

Canada

Polarimetric SAR Interferometry: Investigations using EC CV-580 SAR data

Karim E. Mattar
DRDC Ottawa

Chen Liu
DRDC Ottawa

Ramin Sabry
DRDC Ottawa

Defence R&D Canada – Ottawa

Technical Report

DRDC Ottawa TR 2005-165

March 2005

Abstract

This study examines the potential applications of polarimetric SAR interferometry (Pol-InSAR). Pol-InSAR combines the capabilities of polarimetric synthetic aperture radar (PolSAR) for target classification with interferometric SAR (InSAR) for height discrimination. In this report, the Pol-InSAR literature is first reviewed. Then, two field trials in Ottawa and Petawawa in 2002 are described in which Pol-InSAR data were acquired using Environment Canada's Convair-580 C-band SAR in repeat-pass mode. Calibration and processing of the data are detailed. Finally, data analysis and potential application are discussed, particularly in view to the upcoming RADARSAT-2 and PALSAR missions.

Résumé

La présente étude examine les applications potentielles de l'interférométrie polarimétrique RSO (Pol-InSAR). La Pol-InSAR combine les capacités du radar polarimétrique à synthèse d'ouverture (PolSAR) pour la classification des cibles à celles du radar interférométrique à synthèse d'ouverture (InSAR) pour la discrimination en hauteur. Dans ce rapport, on passe d'abord en revue la littérature sur la Pol-InSAR. Suit la description de deux essais sur le terrain, à Ottawa et à Petawawa en 2002, au cours desquels des données Pol-InSAR ont été acquises au moyen du RSO en bande C installé à bord du Convair-580 d'Environnement Canada en mode à passage répété. L'étalonnage et le traitement des données sont décrits en détail. Finalement, l'analyse des données et les applications potentielles sont examinées, particulièrement en vue des missions RADARSAT-2 et PALSAR à venir.

Executive summary

Polarimetric SAR interferometry (Pol-InSAR) is an emerging technology. It began to attract the attention of the Synthetic Aperture Radar (SAR) R&D community in the past few years for its unique detection and classification capabilities. It combines the two important technologies of polarimetric SAR (PolSAR) and interferometric SAR (InSAR), and enables applications that neither PolSAR nor InSAR alone can achieve. PolSAR enables characterisation of scatterers based on their polarimetric signature. InSAR is used for (among other applications) digital elevation mapping. Pol-InSAR combines both, potentially enabling target characterisation as well as extracting and filtering scatterers based on their polarimetric signature **and** height above the ground.

This report concludes a Technology Investment Fund (TIF) project that addressed developing the technology and software for, and examining the potential applications of, polarimetric SAR interferometry. For this study, Pol-InSAR data were collected during two trials using Environment Canada's Convair 580 (EC CV-580) polarimetric C-band SAR. In June 2002, as part of the CAMEVAL 2002 trial, 14 overlapping polarimetric passes were collected over CFB Petawawa over two days. In September 2002, 8 overlapping polarimetric passes were collected over the cities of Ottawa and Gatineau. Out of all these passes, a few pairs from each site fulfilled the requirements for interferometry, and were selected for further processing and analysis.

Processing of the Pol-InSAR data combines the complexity of both PolSAR and InSAR. Code developed at the Canada Centre for Remote Sensing (CCRS) was used for the Polarimetric portion of the processing. Specialized InSAR and Pol-InSAR code was developed for the remaining portions of the process.

Analysis of the resulting Pol-InSAR data was divided into several sections according to potential areas of application. These include vegetation and forest cover, buildings and the urban environment, isolated manmade structures, and velocity estimation.

Most potential Pol-InSAR applications are highly dependent on the sensor characteristics: its wavelength, resolution, temporal decorrelation, and InSAR baseline are among the critical elements. Potential applications discussed in the literature include vegetation and forest cover measurement. This includes height and biomass estimation, as well as characterisation of scatterers hidden beneath a forest canopy. These applications require long wavelength radar waves capable of penetrating the tree canopy. With its C-band radar, the EC CV-580 SAR was found to be largely unsuited for these applications. The C-band wavelength (5.6 cm) cannot penetrate dense forest cover. Deciduous trees in the winter months, or low-density forests may be the exceptions (this is the subject of ongoing research). Instead, potential applications related to urban areas, buildings, and characterization of other manmade structures were explored, and found some success distinguishing different scatters within a footprint or within a layover region on the basis of their polarimetric signatures and heights. The coarse resolution of the CV-580 data was found to be a critical limitation.

Three different ways of extracting target velocity from PolSAR are explored. The velocity of a target can be estimated from a track analysis, apparent azimuth shift of the target due to its motion, and by using a velocity matched filter. Results from each method are presented.

Pol-InSAR will probably reach its fullest potential only in the horizon 2 (6-10 years) or even horizon 3 (greater than 10 years) timeframe when polarimetric satellite SAR constellations (either in Tandem or Cartwheel modes) may become available. But with the advent of the polarimetric RADARSAT-2 (C-band) and PALSAR (L-band) satellites within the next year or so, and the dual polarization SAR-Lupe constellation and TerraSAR-X within the next few years, all of which are also capable of repeat-pass interferometry, satellite Pol-InSAR data will soon be readily available. Consequently, important applications could see fruition within the horizon 1 (2-5 year) timeframe.

Mattar, K., Liu, C., Sabry, R. 2005. Polarimetric SAR Interferometry: Investigations using EC CV-580 SAR data. DRDC Ottawa TR 2005-165. Defence R&D Canada – Ottawa.

Sommaire

L'interférométrie polarimétrique RSO (Pol-InSAR) est une technologie en émergence. Ces dernières années, elle a commencé à attirer l'attention de la collectivité R et D du radar à synthèse d'ouverture (RSO) en raison de ses capacités uniques de détection et de classification. Elle combine les deux technologies de RSO polarimétrique (PolSAR) et de RSO interférométrique (InSAR) et permet des applications que ni la PolSAR ni l'InSAR ne peuvent réaliser à elles seules. La PolSAR permet la caractérisation de diffuseurs d'après leur signature polarimétrique. L'InSAR est utilisée (entre autres) pour la topographie numérique. Grâce à la combinaison de ces deux technologies, la Pol-InSAR a le potentiel de permettre à la fois la caractérisation des cibles et l'extraction et le filtrage des diffuseurs d'après leur signature polarimétrique **et** la hauteur au-dessus du sol.

Le présent rapport met fin à un projet dans le cadre du Fonds d'investissement technologique (FIT) qui visait le développement de la technologie et du logiciel pour l'interférométrie polarimétrique RSO et l'examen des applications potentielles connexes. Aux fins de cette étude, des données Pol-InSAR ont été collectées au cours de deux essais faisant appel au RSO polarimétrique en bande C installé à bord du Convair-580 d'Environnement Canada (EC CV-580). En juin 2002, dans le cadre de l'essai CAMEVAL 2002, les données de 14 passages polarimétriques chevauchants ont été collectées au-dessus de la BFC Petawawa en deux jours. En septembre 2002, les données de 8 passages polarimétriques chevauchants ont été collectées au-dessus des villes d'Ottawa et de Gatineau. Parmi tous ces passages, quelques paires de chaque endroit répondaient aux exigences relatives à l'interférométrie et elles ont été sélectionnées aux fins d'un traitement et d'une analyse ultérieurs.

Le traitement des données Pol-InSAR combine la complexité de la PolSAR et de l'InSAR. Un logiciel élaboré au Centre canadien de télédétection (CCT) a été utilisé pour la partie polarimétrique du traitement. Un logiciel InSAR et Pol-InSAR spécialisé a été élaboré pour le reste du processus.

L'analyse des données Pol-InSAR résultantes a été divisée en plusieurs parties selon les domaines d'application potentiels. Ceux-ci comprennent la végétation et la couverture forestière, les bâtiments et l'environnement urbain, les structures artificielles isolées et l'estimation de la vitesse.

La plupart des applications Pol-InSAR potentielles dépendent fortement des caractéristiques du capteur : la longueur d'onde, la résolution, la décorrélation temporelle et le référentiel InSAR comptent parmi les éléments critiques. Les applications potentielles dont il est question dans la littérature comprennent la détection de la végétation et la mesure de la couverture forestière. Cela comprend l'estimation de la hauteur et de la biomasse, ainsi que la caractérisation des diffuseurs cachés sous le couvert forestier. Ces applications exigent des ondes radar de grande longueur capables de pénétrer le couvert forestier. Le RSO en bande C de l'EC CV-580 s'est avéré peu adapté à ces applications. La longueur d'onde en bande C (5,6 cm) ne peut pas pénétrer un couvert forestier dense. Les exceptions possibles (qui font l'objet de recherches en cours) sont les arbres à feuilles caduques en hiver ou les forêts à faible densité. Par contre, des applications potentielles en rapport avec des zones urbaines, des

bâtiments et la caractérisation d'autres structures artificielles ont été explorées, et un certain succès a été obtenu à distinguer différents diffuseurs à l'intérieur d'une empreinte ou d'une région de repliement d'après leurs signatures polarimétriques et leurs hauteurs. La résolution grossière des données du CV-580 s'est avérée une limitation critique.

On explore trois façons différentes d'extraire de la PolSAR la vitesse de la cible. La vitesse d'une cible peut être estimée à partir d'une analyse de la route, du décalage d'azimut apparent de la cible dû à son déplacement et en utilisant un filtre en vitesse. Les résultats de chaque méthode sont présentés.

La Pol-InSAR n'atteindra probablement son plein potentiel qu'à moyen terme (6-10 ans) voire à long terme (plus de 10 ans), lorsque des constellations de satellites polarimétriques SRO (soit en configuration tandem, soit en configuration de tonneau) pourront devenir disponibles. Cependant, grâce à l'avènement des satellites polarimétriques RADARSAT-2 (en bande C) et PALSAR (en bande L) dans un an ou deux et de la constellation SAR-Lupe à double polarisation et de TerraSAR-X d'ici quelques années, qui permettent tous également l'interférométrie à passage répété, les données Pol-InSAR seront bientôt grandement disponibles. Par conséquent, d'importantes applications pourraient profiter des résultats à court terme (2-5 ans).

Mattar, K., Liu, C., Sabry, R. 2005. Polarimetric SAR Interferometry: Investigations using EC CV-580 SAR data. DRDC Ottawa TR 2005-165. R & D pour la défense Canada – Ottawa.

Table of contents

List of figures

List of tables

This page intentionally left blank.

Acknowledgements

This study was made possible by the support from the Technology Investment Fund. Maureen Yeremy originally proposed the TIF project and was the principal investigator for the first two years of the project, till her departure from DRDC Ottawa in March 2003. She organized and oversaw all the 2002 trials. Dr. Chuck Livingstone was a project team member and provided valuable advice. This work could not have been accomplished without a team effort and diligent contributions of many DRDC employees and supporting contractors. This included support during the trials, processing of the GPS and radar data, and development of specialized code. In particular the authors wish to thank Terry Potter, Allan Meek, Fred Fletcher, and Craig Williams for their assistance with the polarimetric and GPS processing, and Marina Dragosevic for her work developing polarimetric-interferometric processing code. The authors also wish to thank The City of Ottawa for their permission for use of their aerial photographs. Finally, the authors wish to thank Paris W. Vachon for his many helpful comments while reviewing the paper.

This page intentionally left blank.

Introduction

Polarimetric SAR interferometry (Pol-InSAR) combines the technologies of polarimetric SAR (PolSAR) and interferometric SAR (InSAR), and enables applications that neither PolSAR nor InSAR alone can achieve.

Polarimetric SAR has been an active field of research in the SAR community since at least the 1960's. It enables detection of the polarimetric signature of a scatterer. With the important exception of SIR-C, airborne platforms have been the sole source of polarimetric SAR data. The first two polarimetric satellites will be launched within the next year or so: RADARSAT-2 operating at C-band, and PALSAR operating at L-band.

Interferometric SAR has been a very important technology since the early 1990's. Both airborne and space borne platforms have been used to collect single-pass InSAR data for accurate elevation mapping. Satellite repeat-pass interferometric (SRI) data is an important source of data for centimetre-level terrain deformation mapping. Interferometric coherence has also been used for terrain classification.

Polarimetric SAR interferometry is currently and has been at the forefront of SAR research for a few years. It combines technologies of PolSAR and InSAR, enabling detection and characterization of scatterers based on their polarimetric signature and elevation above the terrain, and hence provides more complete structural information about the scatterer or target. Pol-InSAR also combines the data collection and processing requirements and exigencies of both technologies. It requires good polarimetric calibration, a suitable interferometric baseline, and is potentially subject to temporal, baseline, and volume decorrelation.

Recent, Pol-InSAR research has been primarily orientated towards InSAR applications that distinguish, and indeed highlight, different distributed targets located at the same position but at different elevations. In particular, most current research attempts to exploit the difference in the scattering mechanism between the floor of a forest and its canopy to measure the height of the forest canopy, and help estimate its biomass. Good forest height estimates have been obtained predominantly by the same team of researchers for simple forest structures using the L-band (approximately 24 cm wavelength) to P-band (68 cm wavelength) radar frequency bands. At these long radar wavelengths, Pol-InSAR has also been recently used to detect and characterize targets hidden beneath a forest canopy. By contrast, at X-band (3.24 cm wavelength), where the main scatterer from a tree are its leaves [81], movement of the leaves will be enough to cause a loss of coherence. At C-band (approximately 5.6 cm wavelength) the main scatter from a tree is from its outer branches; movement of the branches will cause a loss of coherence of the tree.

Currently Pol-InSAR data has relied on airborne platforms to collect data. Pol-InSAR data collection is difficult and expensive to obtain. With the upcoming launch of RADARSAT-2 (C-band) and PALSAR (L-Band), Pol-InSAR data will become much more readily available. Both RADARSAT-2 and PALSAR are polarimetric and capable of repeat-pass satellite interferometry, though with a large temporal baseline of 24 and 46 days, respectively.

The challenge for Pol-InSAR research at Defence Research and Development Canada (DRDC) is to: a) research the current methods for sensors and frequency bands available to Canada, b) develop the technology and software for processing Pol-InSAR data, and c) investigate the exploitation of Pol-InSAR data suitable for military applications.

This report is divided into five major sections. In the first, a brief theoretical overview of PolSAR, InSAR and Pol-InSAR will be presented. The second will summarize the two Pol-InSAR data collection trials. The third will provide an overview of the data processing. The fourth will detail analysis of the data, with particular emphasis on potential applications, based on the CV-580 data analysis and survey of the literature. The applications are divided into four general areas: Vegetation and forest cover, buildings and the urban environment, isolated manmade structures, and velocity estimation. The report ends with a summary and conclusions.

Study Motivation and Objective

The principal goal of this project was to acquire Pol-InSAR data sets and develop processing expertise to explore potential military applications to enable DND to take full advantage of this emerging technology.

Pol-InSAR has quickly emerged at the forefront of SAR investigation. Recent R&D using airborne SAR platforms has already demonstrated the importance of Pol-InSAR, particularly in forestry mapping applications and detection, as well as characterisation of targets hidden beneath foliage. Future development of Pol-InSAR is largely dependent on readily available Pol-InSAR data at various wavelengths, resolutions, and interferometric baselines.

With the launch of the C-band RADARSAT-2 and L-band PALSAR expected within the next year or so (the first two polarimetric satellites, also capable of satellite repeat-pass interferometry (SRI)), and the X-band SAR-Lupe constellation within the next few years (dual polarization and SRI capable), there will be ample opportunity to collect Pol-InSAR data at a variety of wavelengths and resolutions with which to further explore this new technology within the horizon 1 (2-5 years) timeframe. This upcoming new capability for satellite repeat-pass Pol-InSAR will help shape the horizon 2 (6-10 years) and horizon 3 (greater than 10 years) era, when it is expected that micro-satellite cartwheel SAR constellation will become available. It is only with a polarimetric cartwheel constellation, capable of single-pass interferometry, that Pol-InSAR will reach its fullest potential.

Theoretical Overview

Pol-InSAR combines the technologies, as well as data collection, calibration requirements and processing requirements of both interferometric SAR and polarimetric SAR. It also combines the exigencies of both fields. It is, therefore, useful to begin a brief review of the theory. This overview will cover interferometric SAR and polarimetric SAR, before summarising the essential elements of Pol-InSAR.

Interferometric SAR

Across-track SAR interferometry was first proposed as a means to extract topographic information in the mid 1970's [2, 68]. The technology is now commonly used for accurate Digital Elevation Model (DEM) generation. Across-track interferometry requires that two SAR images are acquired from nearly the same perspective, separated in both the range and azimuth directions. The images can be acquired simultaneously using two antennas on a single platform (single-pass interferometry) or by repeated passes of a single antenna (repeat-pass interferometry). The transmit and received polarizations of the radar are usually identical, either both HH (e.g. RADARSAT-1) or VV (e.g. ERS-1/2).

Consider a mathematical approach. Two antennas separated by a baseline vector B, image a point P on the ground, a distance r and $r+\Delta r$ from the each antenna, respectively. The received signals, S_1 and S_2 after SAR processing, consist of a terrain reflectivity $u(r)$ modulated by a phase term due to the range distance to the scatterer:

$$s_1(r) = u(r)e^{i\varphi_1}, \tag{1}$$

and:

$$s_2(r+\Delta r) = u(r+\Delta r)e^{i\varphi_2}. \tag{2}$$

Multiplying the first signal with the complex conjugate of the second signal forms the interferogram:

$$s_1(r)s_2^*(r+\Delta r) = \left|s_1 s_2^*\right| e^{i(\varphi_1-\varphi_2)} = Se^{i\phi}, \tag{3}$$

where S is the amplitude of the interferogram, and ϕ the phase.

The phase of the interferogram is not only proportional to terrain topography, but can also include other factors such as geometric effects, tropospheric and ionospheric effects, displacement of the radar footprint, and noise [2]. The change in topographic component of the phase between two points in an interferogram can be related to the difference in their heights Δh, by the following expression [2]:

$$\Delta\varphi_{topo} = \frac{4\pi B_\perp}{\lambda R \sin(\theta)}\Delta h \tag{4}$$

The height ambiguity can be calculated by substituting 2π for the phase change in the above equation and solving for the height change:

$$\Delta h_{2\pi} = \frac{\lambda R \sin(\theta)}{2B_{\perp}} \tag{5}$$

A measure of the phase noise of an interferogram is the coherence γ defined as the absolute value of the normalized cross-correlation between both signals:

$$\gamma \equiv \frac{\left|\left\langle s_1 s_2^* \right\rangle\right|}{\sqrt{\left\langle s_1 s_1^* \right\rangle \left\langle s_2 s_2^* \right\rangle}}. \tag{6}$$

The interferometric coherence varies between 0 and 1. When the two signals are completely uncorrelated, $\gamma = 0$. Then they are identical, $\gamma = 1$. Consequently the achieved accuracy of the measured interferometric phase is reduced by any loss of coherence. The total observed coherence, γ_{total}, can be given in terms of the product of some of the more significant correlation factors [48]:

$$\gamma_{total} = \gamma_{thermal} \times \gamma_{temporal} \times \gamma_{baseline} \times \gamma_{troposphere} \times \gamma_{ionosphere} \times \gamma_{coregistration} \times \gamma_{volume}. \tag{7}$$

where: $\gamma_{thermal}$ is the thermal noise correlation coefficient and is a function of the thermal noise of the two systems; $\gamma_{temporal}$, is temporal correlation; $\gamma_{baseline}$ is the baseline correlation; $\gamma_{troposphere}$ is the correlation due to the troposphere; $\gamma_{ionosphere}$ is the correlation due to the ionosphere; $\gamma_{coregistration}$ is dependent on the accuracy of the registration between image pairs; γ_{volume}, is the correlation coefficient due to volume scatterering.

For the current application, namely airborne repeat-pass interferometry, three of these correlation factors deserve greater attention. $\gamma_{temporal}$ is the correlation factor for non-stationary scatterers. Any movement or temporal change of scatterers within the footprint of the radar and in proportion to the wavelength of the radar may cause a decrease in the temporal correlation coefficient. Rain or snow between acquisitions will also cause a loss of coherence. The movement of trees may cause a loss of temporal correlation and coherence, depending on the wavelength of the radar and the movement of the scatterers within the radar footprint [62]. At X-band (approximately 3.24 cm wavelength), where the main scatterer from a tree are its leaves [81], movement of the leaves will be enough to cause a loss of coherence. At C-band (approximately 5.6 cm wavelength) the main scatter from a tree is from its outer branches; movement of the branches will cause a loss of coherence of the tree. At L-band (approximately 24 cm wavelength), movement of the thicker branches and trunk of the tree would be necessary for a loss of coherence.

The baseline correlation factor, $\gamma_{baseline}$, decreases with increasing separation of the imaging platforms. Specifically, the distance between the platforms perpendicular to both the reference platform track as well as the range direction (referred to as the perpendicular baseline, $B_{\perp}$) is an important distance in question. As the perpendicular baseline increase, the ground reflectivity spectra acquired by the two antennae becomes increasingly divergent. At a certain critical distance, referred to as the critical baseline, the spectra from the two antennae

are completely separated leaving to a complete loss of coherence. In theory, the critical baseline assuming level ground and in the absence of volume scattering, is given by [21]:

$$B_{\perp cr} = \lambda R \tan\theta / 2R_r, \tag{8}$$

Where R_r is the slant range resolution, λ is the wavelength, R is the slant range distance between the antenna and the target, and θ is the nominal incidence angle. The largest perpendicular baseline the can be used for most interferometric applications is always less than its theoretical counterpart.

Finally, volume scattering within the radar footprint, γ_{volume}, can reduce the overall observed coherence. Volume scatterers include fresh water lake ice, and depending on the wavelength of the radar, trees and bushes.

Polarimetric SAR

While interferometric SAR employs a single polarization, polarimetric SAR takes advantage of the full electromagnetic vector field [86]. It is capable of simultaneously imaging a target with both horizontally (H) and vertically (V) oriented electric field vectors, and to record both the like- and cross-polarized returns. This permits the synthesis of the target's polarization signature, potentially providing information about the target's structures or environment that the electromagnetic waves have interacted with through reflection or refraction processes [83].

Polarimetric SAR systems typically provide four channels that are described by the scattering matrix,

$$S = \begin{bmatrix} S_{HH} & S_{HV} \\ S_{VH} & S_{VV} \end{bmatrix}. \tag{9}$$

Here, the channels of the scattered data, S are denoted by a subscript, AB, for the polarization of the transmitted signal, A and the received signal, B. H and V represent respectively, horizontal and vertical orientation relative to the antenna. Reciprocity of the cross-channels is normally assumed, i.e.,

$$S_{HV} = S_{VH}. \tag{10}$$

This reduces the scattering matrix to three channels.

The exploitation of PolSAR data received considerable attention during the 1980's. Significant developments included methods like Van Zyl's which decomposed S into three types of dominant scattering mechanisms [83]. This method was similar to Freeman's decomposition [19], both of these methods were more suitable for **distributed** targets such as ocean and forested surfaces. They were used primarily for distinguishing between rough flat surfaces such as the ocean, volume scatterers such as the forest, and dihedral corner reflections, which can either be associated with man-made objects or which do occur in nature (e.g. at the intersection of a tree trunk with the ground). Ulaby also conducted work on determining SAR signatures and has written extensively on the characterization and statistics of these data [81]. Of note, is the variability of these signatures as a function of season,

environmental conditions, and events. In addition, errors associated with calibration are an important issue. Nevertheless this work is valuable in terms of establishing some reference information. Considerable research was devoted to establishing that from the scattering matrix, *S*, any orientation or basis can be achieved. In this way, by rotating the polarimetric ellipse, an optimal orientation can be achieved that maximizes the signal to noise ratio (e.g. Swartz [74]).

There was also a significant amount of attention directed towards **point target** applications. This work focused on military targets that cannot be described by statistical averages due to the size of these targets and the spatial variability of the scattering type from these targets. In particular, Huynen's work focussed on elemental structure signatures and the detection of these elements that are the building blocks of these targets [31]. This was an area that attracted considerable attention and debate. Many scientists rejected these techniques, because typical statistical confidence tests were not achievable without a large number of pixels associated with a large surface area for a particular structure, which is the case for many military targets. These types of arguments have delayed progress in SAR military target recognition applications. There is the dichotomy that these target sizes are too small to provide meaningful statistics. Yet, there is information which can be used, provided the SNR is high, that is often the case for military targets in many background clutter environments. In particular, a military target's spatial variability effectively provides an increase in the statistical samples when a model of the target is matched or correlated in several dimensions with the SAR data. Alternatively, another method of improving the statistical results is by using more traditional array methods, where the analysis is applied to the original signal data instead of the detected pixel. The work of Huynen and others represent a turning point in SAR analysis methods.

In the mid-1990's, an increase in PolSAR activity and developments progressed. In particular, the primary development was Cloude's coherence method that is also the foundation for later work with Pol-InSAR [1,12]. Cloude developed a coherence method based on the Pauli spin matrices. The coherency matrix T_i for the ith pixel is given by [12, 14]:

$$\vec{T}_i = \vec{k}_i \vec{k}_i^{*T} . \tag{11}$$

Where the superscript T denotes the matrix transpose, and k_i is known as the 3-D Pauli scattering vector and is given by:

$$\vec{k}_i = \frac{1}{\sqrt{2}} \begin{bmatrix} S_{HH} + S_{VV} \\ S_{HH} - S_{VV} \\ 2S_{HV} \end{bmatrix} . \tag{12}$$

The parameters, $|S_{HH}+S_{VV}|$, $|S_{HH}-S_{VV}|$, $|S_{HV}|$, are connected respectively with the symmetry (odd number of bounce), irregularity/double bounce (or even number of bounce) and non-symmetry physical properties in the case of a pure target (strong scatterer), or related to surface scattering, double-bounce scattering and volume scattering in the case of a distributed target (natural media) [31,64].

For multilook data the coherency matrix becomes:

$$\langle T \rangle = \frac{1}{n} \sum_{i=1}^{n} \vec{k}_i \vec{k}_i^{*T} \cdot \tag{13}$$

Cloude's coherence method is utilized for many applications including discriminating different distributed target types and for the Pol-InSAR method. The coherency matrix is effectively a matrix decomposition method relating to underlying physical scattering mechanisms of the scatterer. It can be decomposed to determine information in two dimensions, H and α. H is a measure of the entropy or the statistical randomness of the target types. H varies from 0 (for isotropic scattering) to 1 (for totally random scattering). α is an angle between 0° and 90°, and represents the averaged scattering mechanisms. Three general classes of scattering mechanism are identified. Small values of α are associated with isotropic surface (or Bragg) scattering, where the surface roughness is much smaller than a wavelength. Large values of α are associated with isotropic dihedral or helical scattering. Intermediary values represent anisotropic scattering characterized by a large imbalance between *HH* and *VV*. The H and α form a plane that can be subdivided into 8 zones characterizing the various random media scattering mechanisms. The H and α plane has been studied in further detail by several researchers (e.g. Pottier [64], Lee *et al* [38]) for unsupervised classification, distributed target recognition applications and the detection of man-made targets (usually found in the dihedral, low entropy region of this plane).

Polarimetric SAR Interferometry

Pol-InSAR is an area of research that currently is attracting considerable attention in the remote sensing world. It combines the technologies and advantages of both interferometry and polarimetry, permitting the separation of different types of scatterers within a high resolution cell. Most of the recent research and development has been associated with Cloude's coherence methods [12, 13, 14] and the related Pol-InSAR work of Cloude and Papathanassiou [11, 54, 57]. They and their collaborators are devoting their efforts primarily towards applications that determine distributed target heights. In particular, for certain types of forest cover, they have been successful in determining forest heights and estimating forest biomass from polarimetric interferometric pairs, using both airborne and spaceborne data. Other potential applications of this new technology include soil moisture estimation, surface roughness measurement, and vertical obstruction detection.

An outline of the techniques employed is introduced below, with emphasis on Cloude and Papathanassiou's methodology since their approach is the most common method studied hitherto by researchers.

Pol-InSAR methods (Cloude, Papathanassiou)

The Pol-InSAR methods of Cloude and Papathanassiou are an extension of Cloude's work with the coherence matrix [11, 54, 57]. A monostatic polarimetric interferometry system measures each scatterer in the scene from two slightly different perspectives. This results in two scattering matrices S_1 and S_2. The 3-D scattering vectors can now be written as:

$$\vec{k}_1 = \frac{1}{\sqrt{2}}\begin{bmatrix} S_{1HH}+S_{1VV} \\ S_{1HH}-S_{1VV} \\ 2S_{1HV} \end{bmatrix}, \vec{k}_2 = \frac{1}{\sqrt{2}}\begin{bmatrix} S_{2HH}+S_{2VV} \\ S_{2HH}-S_{2VV} \\ 2S_{2HV} \end{bmatrix} \tag{14}$$

The complex information measured by the SAR system can now be represented in the form of a 6x6 matrix known as a Hermitian positive semidefinite matrix:

$$[T_6] = \begin{bmatrix} \vec{k}_1 \\ \vec{k}_2 \end{bmatrix}\begin{bmatrix} \vec{k}_1^{*T} & \vec{k}_2^{*T} \end{bmatrix} = \begin{bmatrix} [T_{11}] & [\Omega_{12}] \\ [\Omega_{12}]^{*T} & [T_{22}] \end{bmatrix}. \tag{15}$$

T_{11} and T_{22} are the coherency matrices given by (7) or (9) that describe the polarimetric properties for each dataset separately. Ω_{12} contains polarimetric and interferometric information and is a nonhermitian complex matrix that is given by:

$$\Omega_{12} = \vec{k}_1 \vec{k}_2^{*T}. \tag{16}$$

This leads directly to a generalized vector expression for the coherence given by [11]:

$$\vec{\gamma} = \frac{\left\langle \vec{w}_1^{*T}[\Omega_{12}]\vec{w}_2 \right\rangle}{\sqrt{\left\langle \vec{w}_1^{*T}[T_{11}]\vec{w}_1 \right\rangle \left\langle \vec{w}_2^{*T}[T_{22}]\vec{w}_2 \right\rangle}}. \tag{17}$$

w_1 and w_2 are normalized complex vectors that describe the vectorial scattering mechanisms related to image 1 and 2 respectively. Although choice of w_1 and w_2 is arbitrary, it can be assigned in a way to optimize the coherency. This expression for coherence includes both the interferometric (γ_{int}) and polarimetric (γ_{pol}) components of the coherence:

$$\vec{\gamma} = \vec{\gamma}_{\text{int}} \vec{\gamma}_{pol}. \tag{18}$$

In the special case where $w_1 = w_2$, this leads to $\gamma_{pol} = 1$, and $\gamma = \gamma_{int}$.

To extract physical parameters from polarimetric interferometric data, scattering models are generated that relate the desirable parameters to measurable quantities. In this case the measurable quantities are the complex polarimetric interferometric coherences. Most of the work in this area has been devoted to estimation of forest (or crop) height and canopy density. The forest is modelled very simplistically as a vertically uniform spatial density of scatterers extending from the ground to a certain height above the ground [56, 60]. The unknowns to be determined are the forest height and the average extinction coefficient. The extinction coefficient can then be used as an input to a biomass estimation model. As long as there is a return from the volume scatterer and from the ground, and to the degree that the forest conforms to the model, this is a solvable problem. This condition precludes C-band radar for such forest applications, since radio waves at that frequency don't penetrate the canopy of most tree species. Hence for such applications, SARs with the longer wavelength of the L-, S- or P-bands are required. If the model is complicated slightly by adding a gap between the uniform scatterer and the ground, then a dual baseline polarimetric SAR interferometry system is required to solve for all the unknowns (and a careful choice of baseline ratio is required to avoid poorly conditioned inversions) [7, 56]. As the number of baselines increase, polarimetric tomography becomes feasible as was demonstrated by Reigber and Moreira [67]. A polarimetric and interferometric micro-satellite concept has been proposed for global scale forest ecosystem monitoring [51]. A single baseline, but dual-frequency (e.g. L-band and P-

band) Pol-InSAR system would also provide enough parameters to solve for the unknowns [10]. Both JPL's Airsar and DLR's E-Sar experimental airborne platforms are capable of collecting multi-frequency polarimetric data.

Other investigations into the application of polarimetric interferometry found that such a system was highly sensitive to surface moisture and roughness variations (especially in the low roughness domain) [22, 25]. They found that polarimetric interferometry coherence complemented the amplitude information to provide better estimation accuracy of surface parameters.

A number of Pol-InSAR experiments have been undertaken with the French ONERA RAMSES system [15, 18]. This aircraft has X-band and Ku-band systems that can be flown in a polarimetric-interferometry mode. Since neither the X- or Ku-bands penetrate the forest canopy, they are not suitable for forest height or biomass estimation. Instead the envisaged applications include detection of vertical obstruction such as electric lines and other similar urban structures. Preliminary experimental results demonstrated the potential for Pol-InSAR to detect vertical obstructions such a light poles in a parking lot and large electrical support structures [18].

Motion Estimation and Characterization

Polarimetric SAR and Polarimetric SAR interferometry are powerful remote sensing techniques for applications concerning target recognition and change detection. The polarimetric approach explores radar target features (e.g., structure, change) by making use of the full vector properties of the electromagnetic (EM) field while interacting with the target scatterers [34]. Thus, exploitation of polarimetric radar data using appropriate algorithms, results in enhanced target detection and classification capability compared to single channel, single polarization data exploitation [35, 86, 89]. Considering the ability of a polarimetric approach to echo the structural characteristics of a target, one concludes that remote sensing using polarimetry provides comprehensive target motion information. The latter may be better understood through the following observations. In a backscattering mode of operation, effects of the target scatterer movement are contained in both the phase and polarization of the backscattered wave due to variations of line of sight (LOS) or look direction. In other words, the change of illumination angle that is associated with the target motion is manifested as a change of polarimetric signature. The above variations in polarimetric properties contribute to smearing effects in SAR images using conventional high-resolution processing techniques. These nonstationary characteristics within the image space can be studied to analyze target motion and may be compensated to produce the proper image.

In general, the trajectory of a moving target is characterized by a 3-dimensional motion vector. The observation vector that represents the motion can be reconstituted by collecting the echoed waves with different orientations, and may be exploited for motion characterization by analyzing their amplitude and phase relations. According to classical physics and electrodynamics, the above description is the solution of Maxwell's equations for a moving scatterer or source. Therefore, an electromagnetic observation (EM) contains the necessary information to characterize vector motion. Another way of viewing the importance of polarimetric reception is the diversity that improves the signal to clutter ratio (SCR). The SCR improvement is more evident in a moving scatterer scenario (moving target being the

signal and the stationary background being the clutter) [39, 84]. The latter is partly due to variations in polarimetric properties/signature being more significant for nonstationary and non-natural targets as compared to a stationary and natural scatterer. There are also methods to achieve an optimal polarization adapted to the environment under study [11] that maximizes the coherence and, therefore, indicates the direction of the moving target.

According to the above observations, analysis of the coherent scattering matrix can theoretically provide the necessary information to characterize nonstationary and polarimetrically variant effects (e.g., motion).

Basic Theory

In general, a scatterer (stationary or moving) can be characterized as a space-time dependent source or current distribution for an electromagnetic scattering modeling. In classical electrodynamics, the spectral fluence or radiation spectrum of a moving electron is formulated by using retarded potentials as [32]:

$$\mathbf{E}(\omega) = \left(\frac{\varepsilon^2 \omega^2}{2\pi c^4 R} \right)^{1/2} \int dt \; \mathbf{n} \times [\mathbf{n} \times \mathbf{v}(\mathbf{x},t)] e^{j\omega[t-(\mathbf{n}\cdot\mathbf{x})/c]} \tag{19}$$

where $\mathbf{E}(R,t)$ is the received electric vector signal at the observation point R, and $\mathbf{v}(\mathbf{x},t)$ represents the instantaneous velocity of the electron with trajectory $\mathbf{x}(t)$. In (19), ε and c are the particle charge and speed of light. Relation (19) is the canonical equation at the core formulation of radiation and scattering from moving sources.
For moving source distributions, the relation may be generalized as:

$$\mathbf{E}(\omega) = \left(\frac{\omega^2}{2\pi c^4 R} \right)^{1/2} \int dt \int d^3x \; \mathbf{n}(\mathbf{x}) \times [\mathbf{n}(\mathbf{x}) \times \mathbf{J}(\mathbf{x},t)] e^{j\omega[t-(\mathbf{n}\cdot\mathbf{x})/c]} \tag{20}$$

In (20), the unit vector $\mathbf{n}(\mathbf{x})$ denotes a unit vector connecting observation to the source and $\mathbf{J}(\mathbf{x},t)$ represents the source current distribution. Relation (20), which is consistent with the solution of the inhomogeneous wave equation [32], provides insight into EM emission from stationary and moving source distributions. As was addressed, one advantage is the possibility of treating both stationary and non-stationary sources or scatterers within the same frame of approach through proper introduction of distribution functions. For instance, in case of moving or non-stationary distributions, the latter can be achieved by substituting the current distribution in (20) with a shifted distribution $\mathbf{J}_0(\mathbf{x} - \mathbf{r}_m(t), t)$, where $\mathbf{J}_0(\mathbf{x},t)$ is the source distribution in the moving frame, i.e., source distribution without movement, and $\mathbf{r}_m(t)$ is the

trajectory of the distribution motion. In the above approach, the velocity of motion must be non-relativistic. Another significant insight from (20) is the inclusion of source or scatterer instantaneous position and motion in the polarization of the received field signal. Hence, the location information of the scatterer at each instant (embedded in the analytic behaviour of the source distribution) is included in both the phase and vector orientation of the received field signal.

In order to view (20) in the context of scattering formulation, one observes that the backscattering matrix of a target can be found through an EM solution of scattering and may be formulated as the relation between the incident field and the excited scattering source:

$$\mathbf{J}(\mathbf{x}) = \ddot{\chi}(\mathbf{x}) \cdot \mathbf{E}^{i}(\mathbf{x}) \tag{21}$$

where the dyadic $\ddot{\chi}$ represents the mechanism of EM scattering at the target. One can see that the polarimetric reciprocity of the scatterer is manifested as the symmetry of the above dyadic.

Coherent Scattering Matrix Analysis

According to the above discussions, targets with polarimetric identity/nature (e.g., moving targets) can be better studied through polarimetric scattering analysis. The described source formulation can serve as a general analytic frame of reference. In practice, for motion analysis using SAR, however, one should develop more specific and tailored techniques to exploit the coherent scattering matrix.

The required scattering matrix analysis can be viewed in two layers; phase considerations and vector analysis of the echoed field signal. Although closely related, certain degrees of motion estimation may be achieved through either investigation. If the relative scattering matrix remains unchanged (or negligible) within a certain time interval, the scatterer can be assumed to be polarimetrically invariant within the respective illumination interval, and the absolute matrix phase can be used to model motion and the SAR image spread. In this case, application of the scattering matrix span which contains the necessary information about the target reflective function, results in the enhanced SCR [39]. In theory, the aperture processing function can be modified for, or be compared to, the function reflecting the motion for velocity estimation or moving target image correction. Techniques such as time-frequency analysis could also be employed to study the time variations of the Doppler shift. If polarimetric properties vary within the aperture integration time, the relative scattering matrix should be analyzed in conjunction with the absolute phase to extract the correct motion information. In this case, subaperture based techniques can be employed to analyze and correlate low-resolution or subaperture images [27, 51].

Formulation of Motion

To characterize the motion and estimate the velocity of a moving scatterer based on a coherent theory, phase variations of the received radar signal (or image) should be correlated to an

appropriate model for motion. In a polarimetric scenario, the so-called absolute phase of the scattering matrix can be analyzed to extract the motion parameters. It is also possible to take advantage of the relative phase information (i.e., correlation between scattering matrix components) offered by a polarimetric and/or polarimetric interferometry technique to estimate velocity. The latter provides additional information on the motion of the scatterer due to variations of the polarimetric properties caused by motion of the scatterer within the scene. Hence, it is reasonable to utilize the relative phase information in conjunction with the absolute phase to investigate and characterize the motion.

Assuming invariant characteristic boundary conditions (e.g., passive), the instantaneous EM field scattering from a moving object can be viewed as a combination of the instantaneous distance to the sensor and the instantaneous mode of incidence or incident angle. Adopting Huynen's normalized $\mathbf{H}$ formalism (also known as the *Huynen Polarization Fork*) for target scattering [31], the target matrix characteristic operator or scattering matrix is expressed as:

$$\mathbf{H} = m\, U^{*}(\psi, \tau_m, \upsilon)\, \mathbf{S}_c(\gamma)\, U^{*T}(\psi, \tau_m, \upsilon)\, e^{j\xi} \,, \tag{22}$$

where

$\mathbf{S}_c(\gamma) = \begin{bmatrix} 1 & 0 \\ 0 & \tan^2(\gamma) \end{bmatrix}$: eigenmatrix representing target characteristics,

γ : target characteristic angle,

ψ : target tilt,

υ : target multibounce angle,

m : target size or polarimetric excess parameter,

τ_m : target ellipticity angle of principle co-pol max,

ξ : absolute phase

with the transformation:

$$U(\psi, \tau_m, \upsilon) = e^{-j\psi\bar{\sigma}_3}\; e^{j\tau_m\bar{\sigma}_2}\; e^{-j\upsilon\bar{\sigma}_1} \tag{23}$$

In (23), $\bar{\sigma}_1, \bar{\sigma}_2, \bar{\sigma}_3$ are the standard Pauli spin matrices.

In general, we can technically express (assuming invariance of the boundary conditions) the scattering operator at each instance by (22). In other words, the scatterer motion is embedded in time variation of the transformation and the absolute phase in (22)-(23). Coherent analysis of the scattering operator in (22) in conjunction with an appropriate model yields the complete motion characteristics.

As addressed, coherent analysis of the overall scattering matrix or operator is required to analyze the motion. On this basis, there exist various conventional SAR techniques to characterize motion (e.g., GMTI) using time domain, spectral domain or time/frequency approaches [49, 74, 76]. In addition to moving target phase information, a polarimetric approach provides metrics based on the relation between scattering components (relative phase) that contain motion information. Invariance of some such quantities for a given scatterer during the motion can be effectively used to estimate velocity.

For a general bistatic (BSA) case under the change of basis transformation, the span and symmetry of the scattering matrix is conserved. Hence, for a naturally reciprocal target, the scattering matrix remains symmetric at each instant during the motion. The scattering matrix itself is transformed at each instant based on the motion characteristics of the scatterer. To formulate the above observation:

$$S_{VH}(\mathbf{X}_m(t);\mathbf{X}_o(t)=\mathbf{x}_0)=S_{HV}(\mathbf{X}_m(t);\mathbf{X}_o(t)=\mathbf{x}_0) \tag{24}$$

In (24), $\mathbf{X}_m(t)$ represents vector motion of the moving scatterer, and $\mathbf{X}_o(t)=\mathbf{x}_0$ states that the observation or sensing is made at the point $\mathbf{x}_0$ on the aperture. In practice, the two channels are not measured at the same instant. Instead, they are detected at different instants and registered by interpolation in the image space. Thus, a decorrelation is manifested:

$$S_{VH}(\mathbf{X}_m(t+\tau);\mathbf{X}_o(t+\tau)-\mathbf{X}_{shift}(\tau)=\mathbf{x}_0)\neq S_{HV}(\mathbf{X}_m(t);\mathbf{X}_o(t)=\mathbf{x}_0) \tag{25}$$

where $\mathbf{X}_{shift}$ denotes the required vector shift in the image space to register the two channels. As can be seen, for $\tau=0$ and the case of a stationary target, i.e., $\mathbf{X}_m(t)=$ constant, the reciprocity is recovered. Inspection of (24)-(25) shows that the phase difference between S_{HV} and S_{VH} (after co-registration) corresponds to the difference between the overall shift for a target moving from temporal point t (observed at the spatial point $\mathbf{X}_o(t)$ on the aperture) to point $t+\tau$ (observed at spatial point $\mathbf{X}_o(t+\tau)$ on the aperture) and shifted in image space. Accordingly,

$$Arg\left(S_{VH}/S_{HV}\right)\left(\left|\mathbf{X}_m(t+\tau)-\mathbf{X}_o(t+\tau)\right|-\left|\mathbf{X}_m(t)-\mathbf{X}_o(t)\right|\right)-x_{shift}(t;\tau)=\Delta R \tag{26}$$

with,

$$x_{shift}(t;\tau)=\left(\left|\mathbf{x}_0+\mathbf{X}_{shift}(\tau)-\mathbf{X}_m(t)\right|-\left|\mathbf{x}_0-\mathbf{X}_m(t)\right|\right) \tag{27}$$

Considering the above discussion, we may relate the motion to the cross polarization correlation (decorrelation):

$$\frac{S_{HV}S_{VH}^{*}}{|S_{HV}||S_{HV}|}=e^{j2k\Delta R}=e^{j\phi} \tag{28}$$

In (28), $k=\frac{2\pi}{\lambda}$ is the free space wave number, and ΔR (as given by (26)-(27)) represents the displacement of the scatterer during the time τ. According to (28), the cross-correlation or asymmetry of a reciprocal scatterer at each point on the aperture is caused by reception of the two components at the two endpoints of a baseline with length $B=V_a\tau$ (V_a being the sensor velocity) and co-registering them in the image plane. According to (26)-(28), the slant range velocity can be estimated by:

$$\phi=\frac{4\pi}{\lambda}V_r\tau \tag{29}$$

In a polarimetric scenario containing moving and stationary reciprocal scatterers, decorrelation of the instantaneous cross-pol scattering components (S_{HV} and S_{VH}) can be attributed to the moving scatterers and the presence of a virtual baseline. This baseline can be physically designed as the separation between antennas on the sensor platform. In a conventional polarimetric scenario, however, a small virtual baseline is created as the result of alternate transmission of polarization pulses. Length of this virtual baseline is inversely proportional to the pulse repetition frequency (PRF). In brief, cross-correlation of the scattering components or asymmetry of the scattering matrix for a reciprocal scatterer, contains change information that can be exploited in the range/azimuth stage (i.e., raw data), the subaperture stage, or in the processed image stage to characterize target velocity.

Temporal (at different instants along the aperture) decorrelation of the cross-pol scattering elements will be transformed to the processed image as decorrelation between S_{HV} and S_{VH} of the respective image pixels shift as a function of target movement. The phase difference between S_{HV} and S_{VH} of the image pixels containing the change effects are, in general, related to temporal decorrelation of such elements through a nonlinear transformation depending on the motion characteristics and processing system kernel function. For uniform motion (i.e., invariant during the aperture slow time), one can show that the phase difference between image pixels is (theoretically) the same as the instantaneous phase decorrelation. Thus, (28)-(29) may be applied to estimate the velocity from the image.

The effect of the target motion appears in the SAR image as a shifting and smearing of the target image. The smear is mainly due to the scatterer displacement within the SAR image integration time. Other processing related issues might also contribute to the smearing effects. The shift in the image plane is essentially due to the shift of the Doppler centroid as a result of change in relative velocity between the sensor and the scatterer. To evaluate the azimuth shift, consider the range function:

$$R(x)=\sqrt{(X-x+v_x t)^2+(Y+v_y t)^2+H^2} \tag{30}$$

where (X,Y) denote the position of a moving target at the reference time instant $(t=0)$, (v_x, v_y) are the velocity components of the moving target in the azimuth and ground range directions, $x=V_a t$ and H represent the sensor cross-range position and altitude.

At the target reference broadside, $\frac{\partial R}{\partial x}=0$ $(v_y=0)$ and

$$x_b=\frac{X}{1-\frac{v_x}{V_a}} \tag{31}$$

The imaged broadside position, however, is observed at a different location due to movement in the range direction $\left(\frac{\partial R}{\partial x}=0\right)$:

$$x_{bm}=\frac{X\left(1-\frac{v_x}{V_a}\right)-\left(\frac{v_y}{V_a}\right)Y}{\left(1-\frac{v_x}{V_a}\right)^2+\left(\frac{v_y}{V_a}\right)^2} \tag{32}$$

The azimuth shift can be found by using (31) and (32) as:

$$\Delta x=\frac{\left(\frac{v_y}{V_a}\right)Y}{\left(1-\frac{v_x}{V_a}\right)^2+\left(\frac{v_y}{V_a}\right)^2}=\frac{\left(\frac{v_r}{V_a}\right)R_b}{\left(1-\frac{v_x}{V_a}\right)^2+\left(\frac{v_y}{V_a}\right)^2} \tag{33}$$

where R_b and v_r are the slant range and the slant range velocity at the target broadside location.

The set of equations (28)-(29) and (33) can be used to estimate the moving target velocity by measuring the scattering components and the along track shift caused by the target motion.

Experimental Trials

Two trials conducted in 2002 collected polarimetric repeat-pass interferometric data using Environment Canada's CV-580 C-band SAR [40]. The first trial was part of the CAMEVAL (CAMouflage EVALuation) trial and was held in Petawawa, Ontario on June 5 and 8, 2002. The second trial was held in Ottawa on September 24, 2002. A detailed description of the trials is available elsewhere [73, 85].

A detailed description of the EC CV-580 has been previously published [39]. Repeat-pass interferometry using the EC CV-580 was first attempted in 1993 [22]. That study collected repeat-pass interferometry at both X-band and C-band, but only in one channel. The aim of that study was to improve understanding of repeat-pass interferometry, and to measure the centimetre level displacement of a corner reflector between passes. For this study, the CV-580 was operated at C-band in its polarimetric mode. Pertinent parameters are given in Table 1.

Table 1: Some parameters for the EC CV-580 Pol-InSAR system [39]

PARAMETER	VALUE
Frequency	5.3 GHz
Wavelength	5.66 cm
3dB Range Resolution	5.7 m
Slant Range Pixel spacing	4 m
(PRF/V)	2.567
Along-track Pulse Spacing (nominal)	0.39 m
Azimuth Beamwidth	3.1°
Image Data Recording	4096 range pixels
Swath Width in Nadir Mode (approximate)	22 km
Cross-Polarization Coupling (vertical and horizontal)	<–35 dB

Pol-InSAR Experiment at the CAMEVAL Trial

The CAMEVAL trial spanned four days, from June 5 to June 8, 2002. The polarimetric interferometric data collection formed only one component of a series of experiments. These Pol-InSAR experiments were carried out during the first and last days of the trial. The main objective of this component of the trail was to collect Pol-InSAR pairs for forest and military target discrimination. This would provide evidence of Pol-InSAR capabilities at frequencies similar to those of RADARSAT-2. The Petawawa site provided for a variety of forest covers and forest densities; both evergreen and deciduous. Military vehicles were deployed in several locations in the area [73]. The vehicles were deployed in open fields, along the tree line, and under forest canopy. This included both coniferous and deciduous forest types.

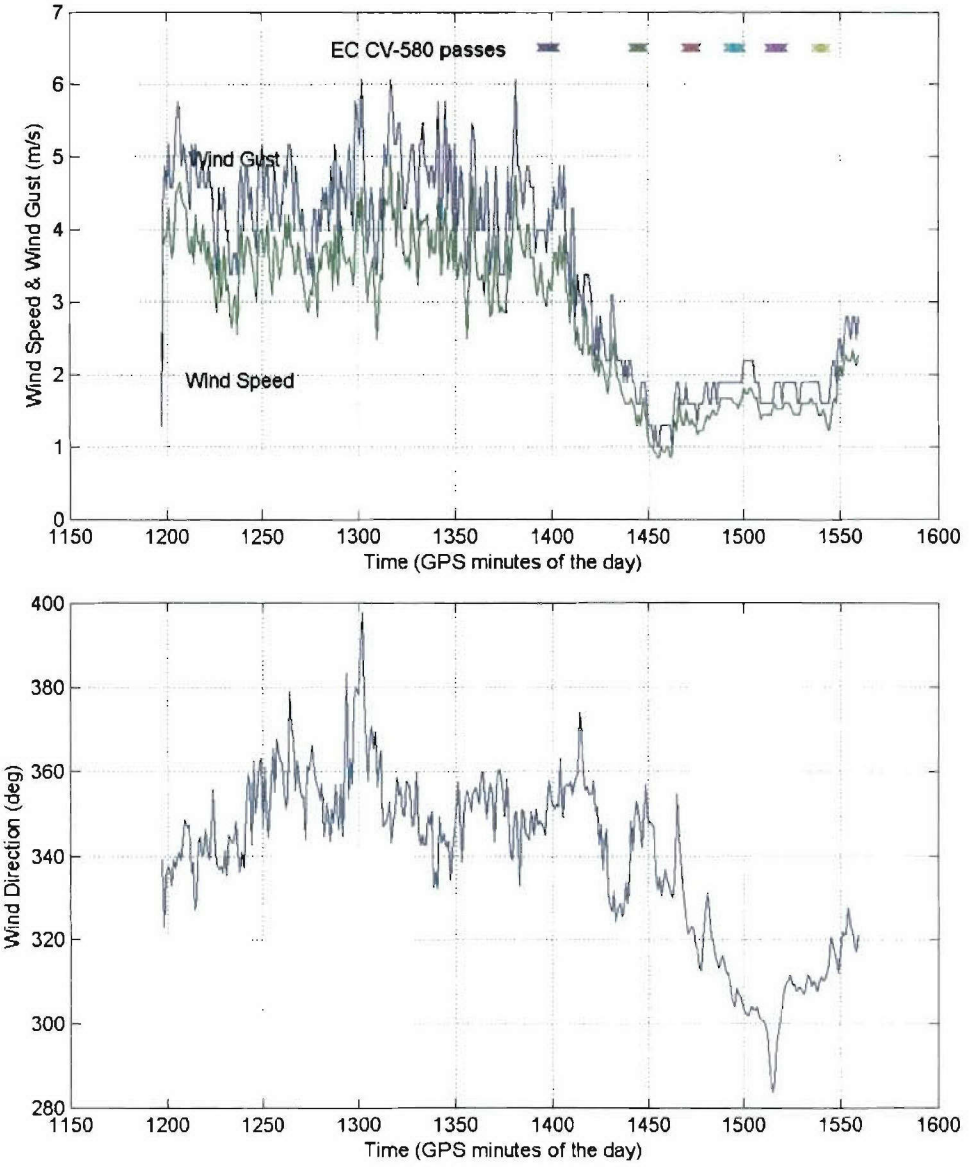

Figure 1: Wind speed, wind gust, and wind direction during June 5, 2002 Petawawa trial.

Only one flight track was designed for the Pol-InSAR trial; it was flown repeatedly in order to increase the chances of acquiring suitable Pol-InSAR image pairs. For successful interferometry, the flight line separation (or baseline) needed to be less than approximately 35 meters. On June 5, 6 polarimetric passes were collected before the mission was aborted due to equipment problems. Of these, the first pass was accidentally flown with the wrong flight track. This left only 5 passes for possible Pol-InSAR studies.

Environmental conditions also proved difficult. Although there was no precipitation reported during the flight lines, there were variable wind conditions. The surface wind data for June 5 in the Petawawa region is plotted in Figure 1, together with the timeline for the 6 passes. For a variety of reasons, another trial date for Pol-InSAR was set for June 8.

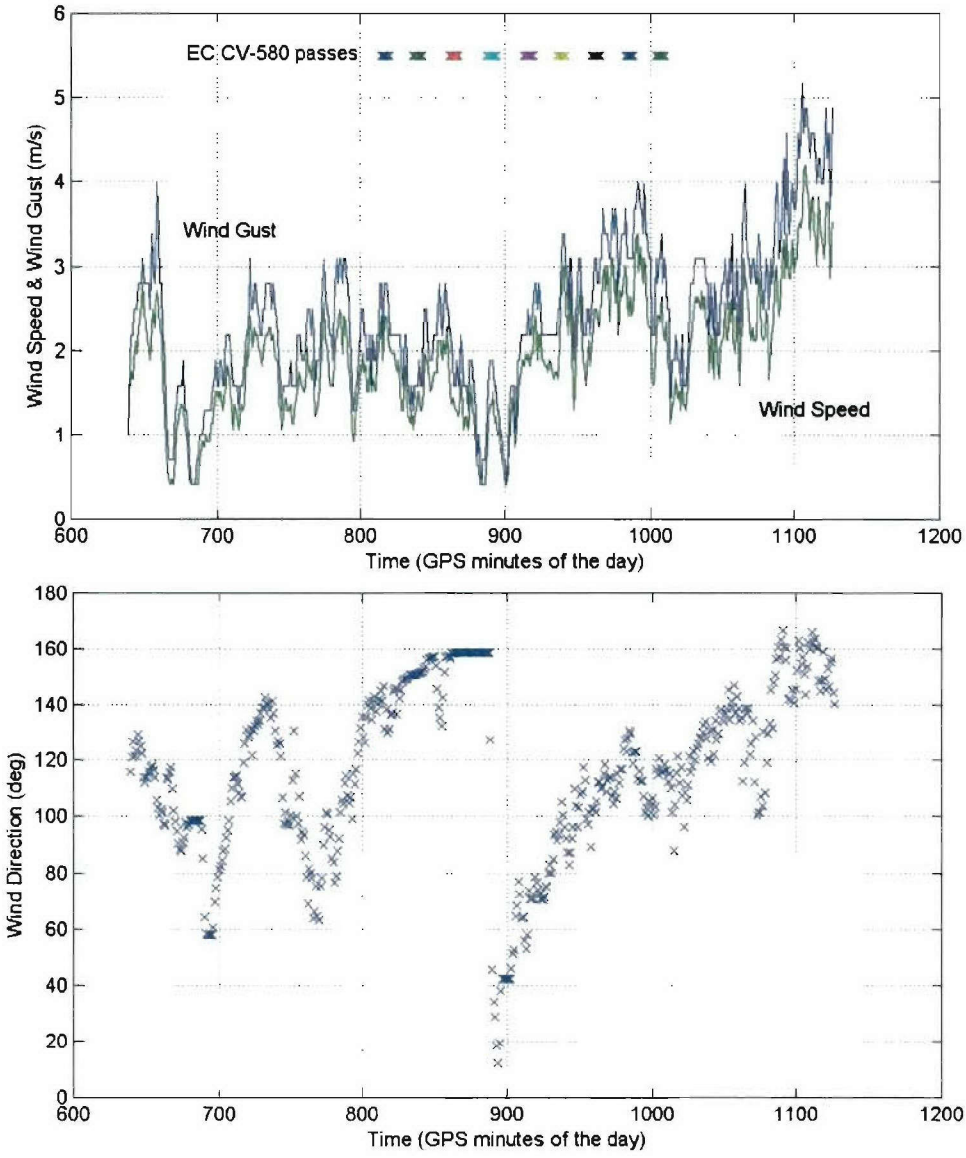

Figure 2: Wind speed, wind gust, and wind direction during June 8, 2002 Petawawa trial.

On June 8, 9 polarimetric passes were collected. Light rain was reported almost throughout the trial. Figure 2 shows the surface wind conditions, and the timeline for the 9 passes for Petawawa on June 8, 2002. Wind gusts and wind direction were markedly variable throughout the day's data collect.

An extensive ground truthing effort paralleled the radar data acquisition. A calibration site was setup to permit polarimetric and radiometric calibration of the SAR image data. The calibration site was located on the open and relatively flat terrain of the CFB Petawawa. Five reorientable corner reflectors (CRs) and three polarimetric Active Radar Calibrators (ARCs) were deployed. Clusters of 4 CRs were also setup at other deployment sites in the region. All

the CRs and ARCs were surveyed using GPS, permitting them to serve as ground control points (GCPs).

Other ground truthing included environment information collects, such as wind speed, wind gust, wind direction, and soil moisture. An Ashtek Z12 GPS base station collected geopositional data for determining the Differential GPS (DGPS) position of the SAR. Extensive photographs were collected of the calibration site and deployed vehicles.

A variety of military vehicles were deployed during the CAMEVAL trial [73]. Although these were not part of the Pol-InSAR experiments, they were on site during both the June 5 and 8. In all, nine vehicles were deployed at each of two sites: at the edge of a coniferous forest and at the edge of a deciduous forest. Both of the forest sites border on ranges that are clear of trees, and were selected for their homogeneous and well-studied tree lines. In each case, vehicles were deployed in triplicate under forest canopy, along the tree lines and in open field.

A secondary objective of this Pol-InSAR trial was to determine if motion could be extract from PolSAR data [85]. The manner in which the CV-580 SAR collects PolSAR data, i.e. by alternating transmit H and V, created a short along-track displacement between the cross polarization channels [6]. Analysis similar to along-track InSAR can take advantage of this information and extract velocity information. For this portion of the experiment, a CR was placed on board of a pickup truck (facing backward). Just before each of the flight lines, the truck processed along Clement Lake Road at a constant velocity in a direction perpendicular to and away from the flight line. The speeds of the trucks were held fixed during each pass, varying between 5 km/hr and 15 km/hr between passes.

Ottawa Trial

The CV-580 data collect over Ottawa occurred on September 24, 2002. The objectives for this trial were several. The City of Ottawa and its surrounding was ideally suited to the study and exploitation of Pol-InSAR capability in an urban and semi-urban environment. The city of Ottawa offers a variety of urban signatures that could be used to examine Pol-InSAR applications. Ottawa valley's greenbelt is the site of several forests, including single species forests. The Ottawa trial also served as an opportunity to test how accurately motion could be derived from PolSAR data. In contrast with the CAMEVAL trials, this time four different types of radar reflectors were deployed on four moving trucks, which served to augment this portion of the trial.

Repeat-pass Polarimetry Experiment

On September 24, eight passes of the CV-580 operating in the polarimetric mode at C-band were collected over Ottawa. In order to maximize opportunities for repeat-pass InSAR, attempts were made to collect all eight passes following exactly the same track. Surface wind conditions, together with the timeline for the nine passes, are shown in Figure 3. Both were relatively moderate compared with those observed during the CAMEVAL trial.

An extensive ground truth effort paralleled the radar data collect [85]. The site of the permanently stationed trihedral corner reflectors at Connaught Range in Ottawa was used as the calibration site. To permit polarimetric calibration, two ARCs were also deployed at the

site. A newly designed ARC and two more corner reflectors were also deployed on the DRDC Ottawa campus. All the corner reflectors and ARCs were surveyed using GPS.

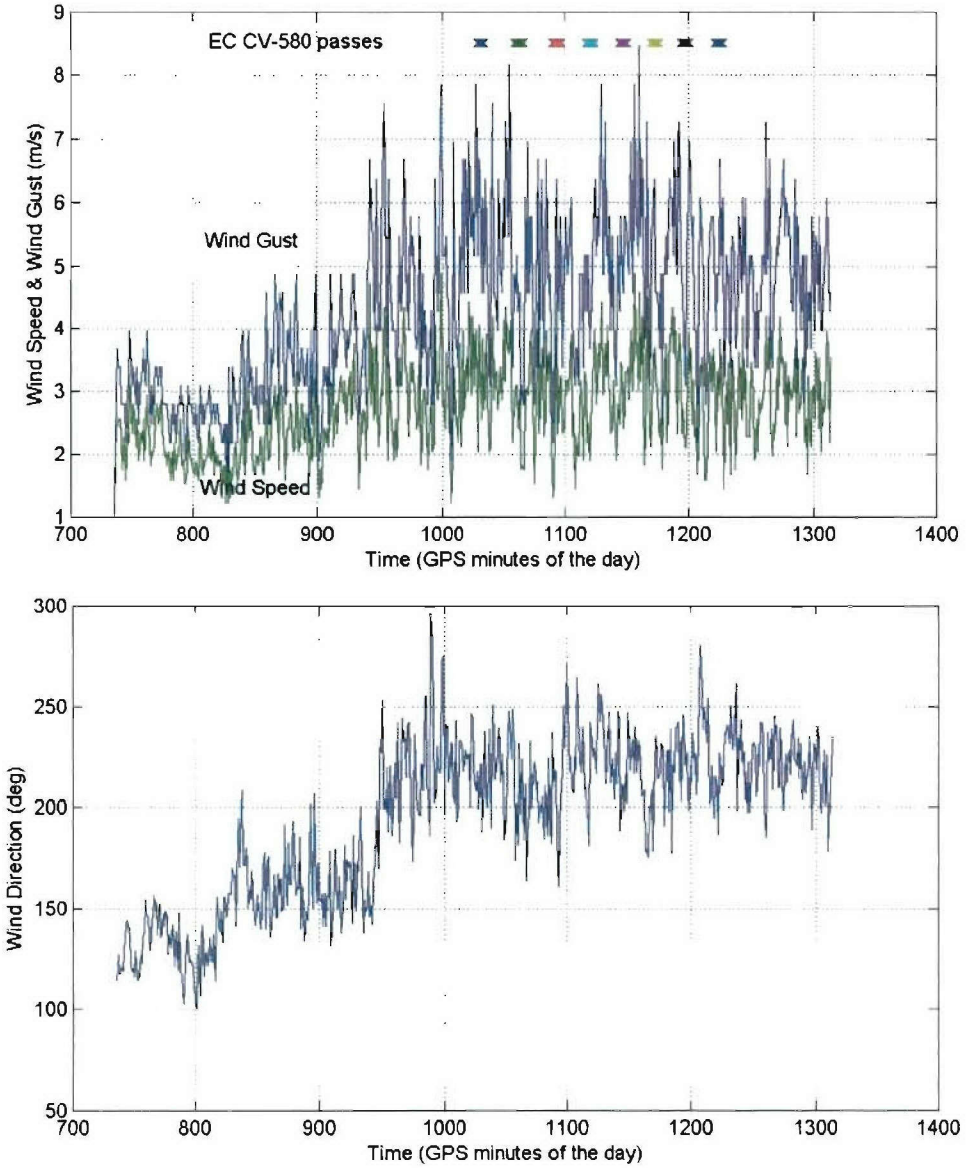

Figure 3: Wind speed, wind gust, and wind direction during September 24, 2002 Ottawa trial.

Environmental data were collected during the image acquisition and included wind speed, wind gusts, wind direction, and precipitation. Soil moisture measurements were collected at the calibration site.

GPS data were collected with an Ashtek receiver. GPS data from the NRCan stations were also requested; the Algonquin station data was the only one received. These served as the base station for the differential GPS processing for the motion compensation analysis.

A photographic record complemented the image collect of urban signatures in the Ottawa area and targets of opportunity. Key urban areas were photographed during the image acquisition of September 24, including Tunney's pasture and downtown Ottawa, with the National Gallery and Parliament Hill. Capturing any event out of the ordinary that may impact the radar signature in these selected areas was of particular interest. At this time, for example, the Parliament Hill Library was partly enclosed by scaffolding. Furthermore, a fully deployed crane was seen near the National Gallery; another deployed crane was seen near one of the buildings at Tunney's Pasture. Photographs also documented the ground truthing, including the site of the ARC, corner reflectors, and moving target experiment.

A second set of photographs was collected post-mission, after some of the PolSAR data had been analysed. Key areas of interest here were some of the bridges between cities of Ottawa and Gatineau, the lampposts along these bridges, and the lampposts near the Casino de Lac-Leamy (see Figure 4).

Figure 4: Photographs of various streetlights on several of the streets and bridges of the cities of Ottawa and Gatineau. Clockwise from the top left are Champlaine Bridge, Portage Bridge, Boulevard de la Carrier (Gatineau), and Highway 5 (Gatineau).

Moving Target Experiment

The moving target experiment was designed to provide each flight line with a series of radar reflectors moving at a constant velocity away from the radar. Four trucks were mounted with four different types of radar reflectors (see Figure 5). These were:

1. A dihedral mounted at an orientation of +45° relative to a z-x plane where z is altitude and x is aligned with the rear of the truck and parallel to the ground. Dihedrals orientated at ±45° provide large cross polarized returns to the SAR.

2. A dihedral mounted at an orientation of −45° relative to the z-x plane.

3. A trihedral corner reflector which provides a large co-polarized return.

4. A vertical grate chosen to provide a dipole signature.

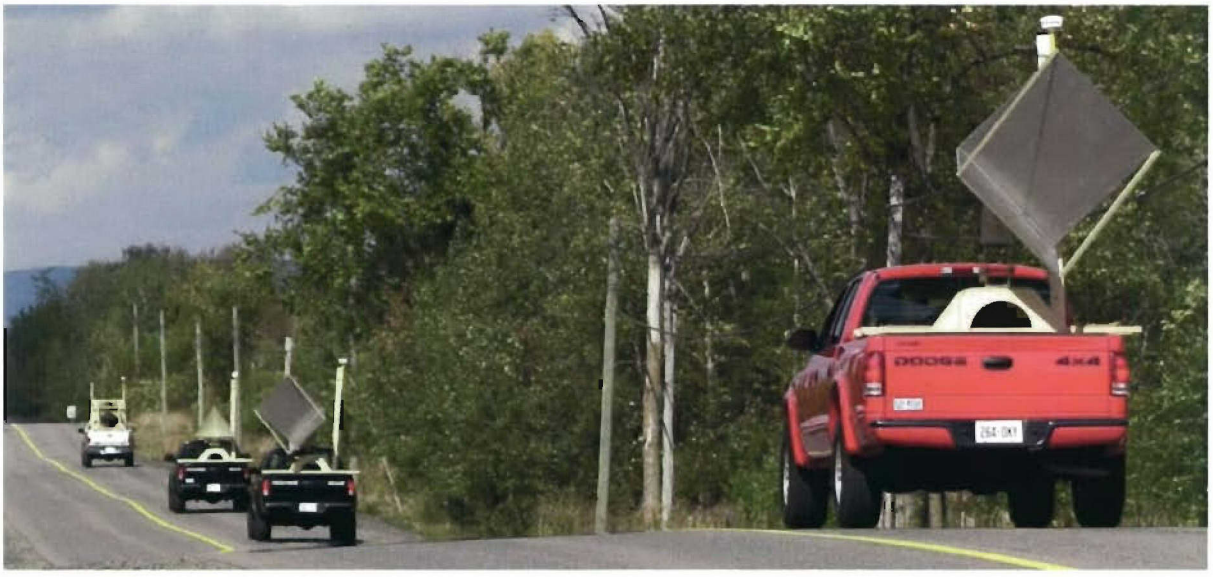

Figure 5: Photographs of the four trucks with radar reflectors moving north on Rifle Road during moving target experiment.

With 50 meters of separation, the trucks were driven north on Rifle Road in a direction nearly perpendicular to, and away from, the flight line. Rifle Road is oriented approximately 338° from North. The trucks were driven at a constant speed; a different constant speed for each flight line (see Table 2). The drivers of the trucks were in constant contact with the CV-580. A few seconds before the estimated time that Rifle Road would come within view of the radar, the drivers would start driving from Carling Avenue at the prescribed velocity for the pass in question. The velocity and timing was measured with a GPS receiver on board each of the trucks. The timing between the departure of the trucks from Carling Avenue and imaging of the road was critical. The maximum distance the trucks could travel on Rifle Road was less than 2 km. A delay in the departure of the trucks could mean that by the time the CV-580 was imaging the road, the truck would already have reached the end of Rifle Road and the opportunity for imaging the moving target would be lost for that pass. This did occur in at least one of the passes.

Table 2: Moving Target interval times relative to September 24, 2002 SAR image acquisitions.

PASS	VEHICLE SPEED (*km/hr*)	LEAD VEHICLE DEPARTS (UT)	LEAD VEHICLE FINISH (UT)	LAST VEHICLE FINISH (UT)	SAR ACQUISITION TIMES (UT)	
Test	20	16:40:42	16:46:18			
1	30	17:05:58	17:10:08	17:10:33	17:09:44	17:14:13
2	35	17:37:48	17:41:20	17:41:49	17:39:10	17:43:12
3	20	18:09:18	18:14:53	18:15:18	18:10:50	18:15:35
4	30	18:37:48	18:41:48	18:42:15	18:37:38	18:42:32
5	35	19:04:43	19:08:16	19:08:48	19:05:07	19:09:25
6	20	19:31:03	19:36:33	19:37:13	19:30:58	19:35:50
7	30	19:54:53	19:58:50	19:59:21	19:54:39	19:59:20
8	35	20:20:18	20:23:48	20:24:18	20:20:50	20:25:43

Data Processing

Processing of the polarimetric interferometry data is a relatively complex procedure. It requires polarimetric and interferometric processing, as well as Pol-InSAR processing. The utility of the polarimetric interferometry data depends on the accuracy with which each of these steps are carried out. The EC CV-580 SAR data in particular, required specialized software for motion compensation. The processing steps are outlined in Figure 6. A functional description of each of these steps follows.

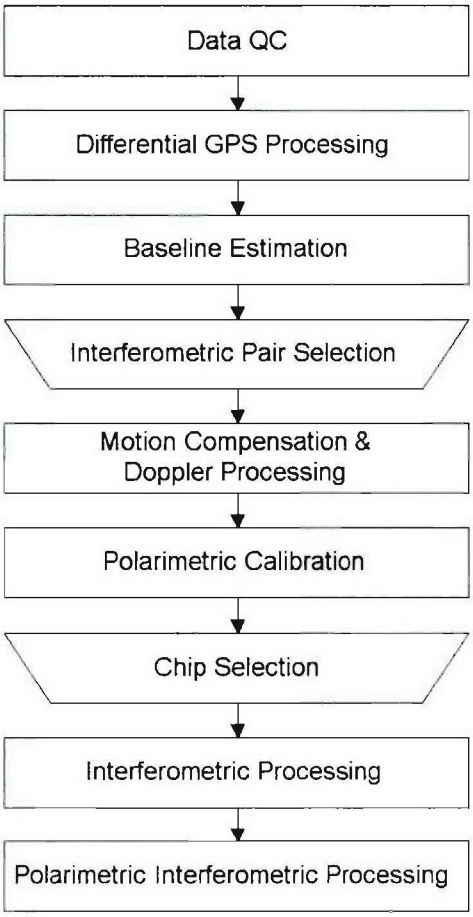

Figure 6: Pol-InSAR processing flowchart.

Data Quality Control

The first step in any data processing is quality control (QC). In this case, the quality of the GPS, the inertial navigation system (INS), and the radar data were carefully scrutinized for glitches that could adversely affect the subsequent processing. Some quality control is undertaken automatically through the software. But manual checking is also necessary. "Glitches" in either the GPS or INS data that can arise from list GPS satellite coverage can

directly impact the motion compensation of the radar data, and consequently impact the final output.

Differential GPS Processing

Commercial software is used in the second step, for downloading and processing the GPS data. Besides the use of Matlab™, this is the only portion of the processing chain where commercial software is used. All other portions of the software chain were either programmed in house or obtained licensed from Canada Centre for Remote Sensing (CCRS).

At least one surveyed GPS base station is required for use with the GPS receiver on board the EC CV-580 to derive the accurate differential GPS (dGPS) information required for processing of the SAR imagery. For the Ottawa dataset, three surveyed base stations were available, and all were for dGPS processing [85]. For CAMEVAL, only one base station was used for the dGPS processing [73].

Baseline Estimation

The third step in the processing chain is baseline estimation. The crucial component for the baseline in interferometry is the perpendicular baseline, $B_{\perp}$, the component of the baseline perpendicular to both the velocity vector of the master platform and the line-of-sight from the platform to the target. The length of the perpendicular baseline limits the maximum possible coherence of the interferometric pair. This will dictate which of the flight lines collected would be suitable for interferometric processing, and therefore which of the flight lines should be considered for further processing. The theoretical critical perpendicular baseline that achieves total decorrelation between the interferometric pair can be calculated using (8). The critical perpendicular baselines for a target at the centre of the swath for the CAMEVAL 2002 trial of June 8 and the Ottawa trial of September 24, 2002 are given in Table 3. For the calculation, flat-earth geometry was assumed; 0.056 m was used as the wavelength of the C-band, and 5.7 m for the nominal slat-range resolution of the EC CV-580 SAR [39].

Table 3: The nominal theoretical critical perpendicular baseline for June 8 (CAMEVAL 2002) and September 24 (Ottawa) trials.

TRIAL DATE (2002)	MEAN PLATFORM ELEVATION *(m)*	NOMINAL INCIDENCE ANGLE TO CENTRE OF SWATH (DEGREES)	RANGE FROM PLATFORM TO TARGET AT CENTRE OF SWATH *(m)*	THEORETICAL CRITICAL PERPENDICULAR BASELINE FROM EQ (8) *(m)*
June 8	6,600	57.5	12,284	96
Sep 24	5,230	57.5	9,734	76

The practical limit for the perpendicular baseline that provides for usable coherence levels is less than the critical baseline. Empirically, the usable limit of the perpendicular baseline is on the order of 1/2 to 1/3 of the critical baseline; as will be shown later, it is roughly 35 m for the geometry in these trials.

Interferometric Pair Selection

With a few approximations to the geometry, the critical baseline between any two flight lines can be estimated using only the differential GPS measurement of the aircraft's position. Figure 7 and Figure 8 show the passes with the best perpendicular baseline for the June 8 CAMEVAL 2002 trial. Plotted on the abscissa is the distance, in kilometres, from the calibration site. The eight parallel passes that make up the trial offer 28 possible interferometric pairs. The figures show the only three of the pairs have perpendicular baselines less than 20 m near the calibration site. Pass 6 and 9 were the best, with a perpendicular baseline of 9 metres at the calibration site. Passes 1 and 3 and passes 1 and 6 have perpendicular baselines of 12 and 18 metres respectively at the calibration site. A couple of the other passes have suitable baselines 10 to 30 km west of the calibration site, but that is outside the immediate site of interest. Based on these results, passes 1, 6, and 9 were selected for further processing. These would provide a range of baselines within the limits acceptable for interferometry, and consequently based on (5) and Table 4, a range of $h_{2\pi}$ height ambiguities.

Figure 9 and Figure 10 show the corresponding baseline estimates for September 24 Ottawa passes. Plotted on the abscissa is the distance in kilometres from Connaught Range, the calibration site. Also indicated for reference is the site of the Parliament. The sites of immediate interest to this study lie between Connaught Range and Parliament. Within this range, 4 pairs of passes offered a range of perpendicular baselines suitable for interferometry and a range of height ambiguities (see Table 4), and therefore were selected for further processing. These pairs are passes 1 and 3, 5 and 8, 6 and 8, and 5 and 6.

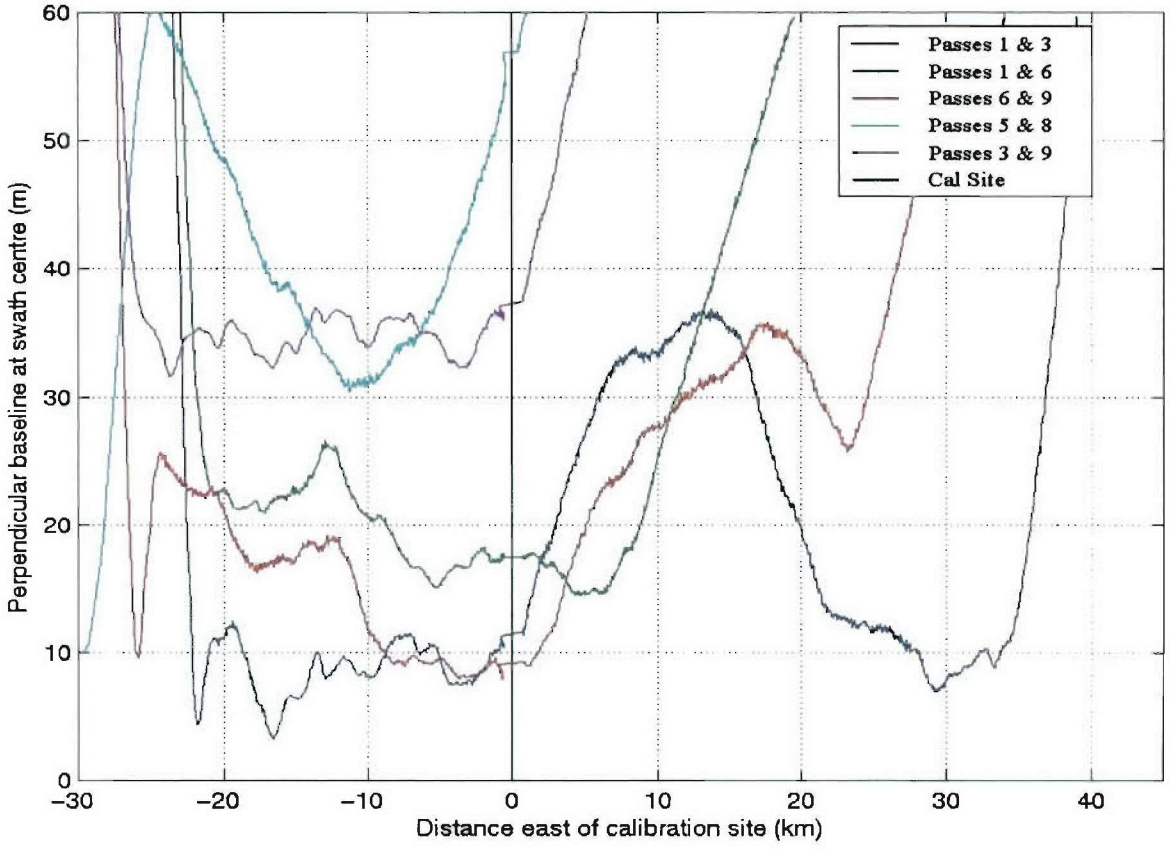

Figure 7: Passes with the smallest perpendicular baseline estimates for June 8, 2002 trial relative to the calibration site.

Table 4: Calculated $h_{2\pi}$ height ambiguity using (5) as a function of the perpendicular baseline for the June 8 and September 24 trials given the parameters of Table 3.

PERPENDICULAR BASELINE *(m)*	$h_{2\pi}$ HEIGHT AMBIGUITY *(m)*	
	June 8, 2002	*Sep 24, 2002*
2	146	116
5	59	46
10	29	23
15	19.5	15.4
25	11.7	9.3
35	8.4	6.6
50	5.9	4.6
75	4.0	3.1

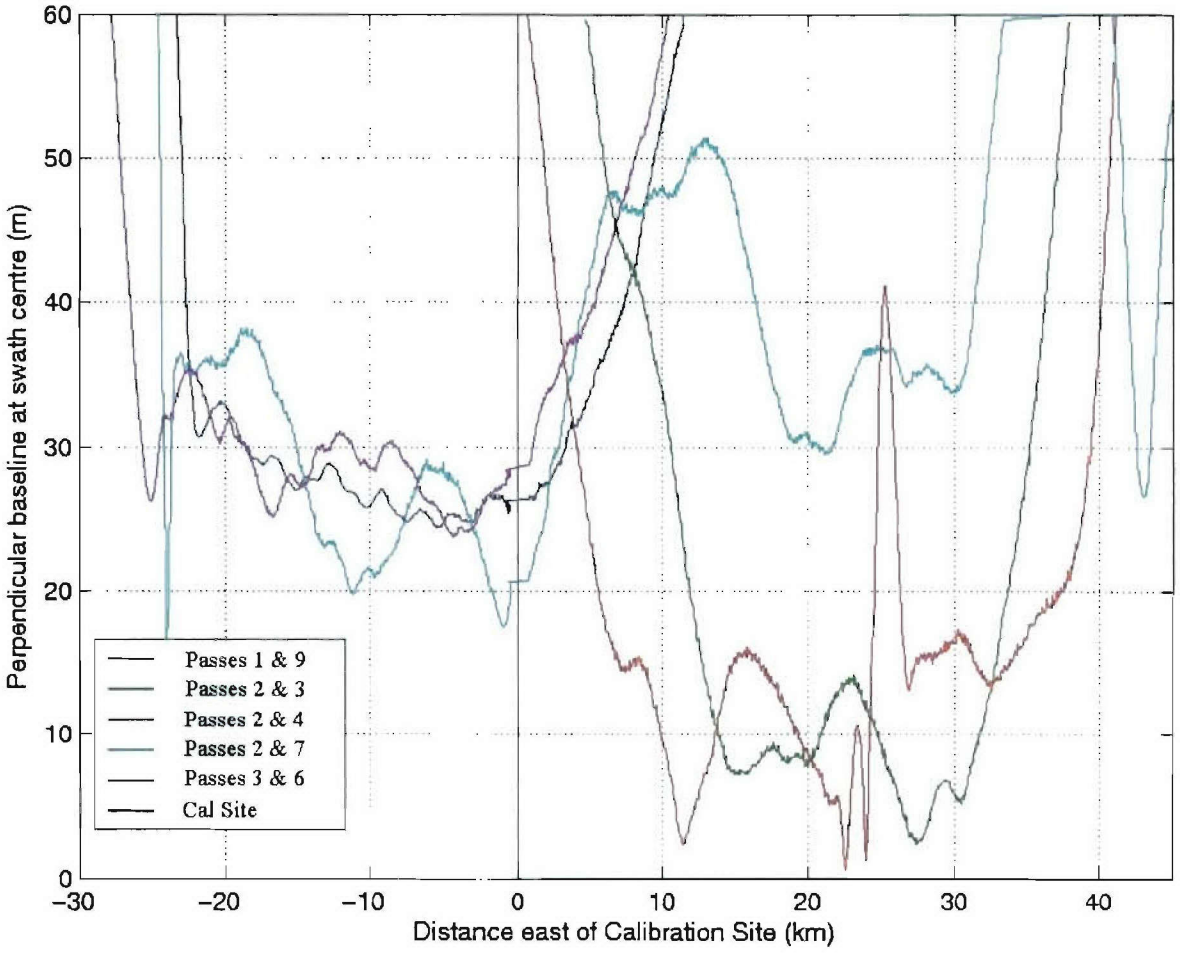

Figure 8: Perpendicular baseline estimates for other passes from June 8, 2002 trial relative to the calibration site.

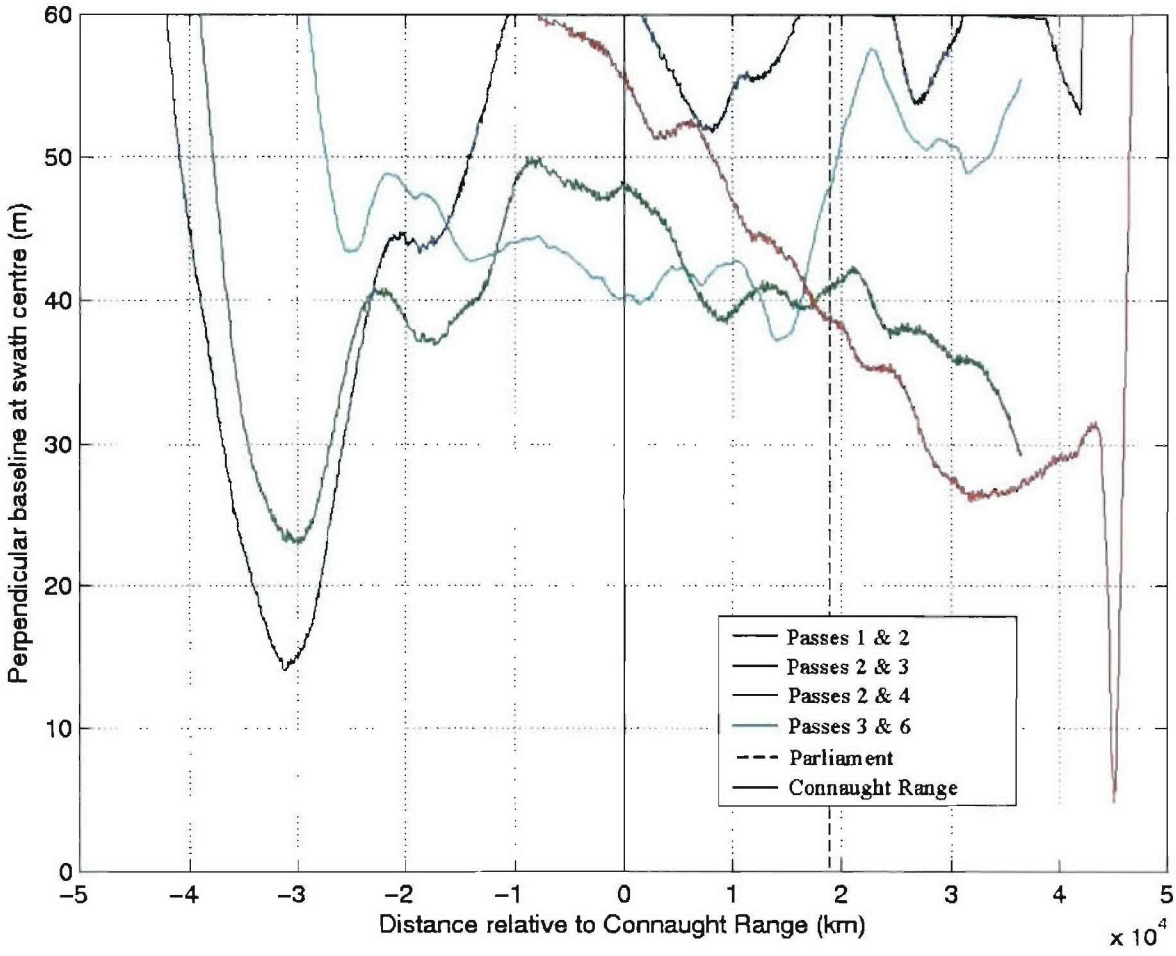

Figure 9: Passes with the smallest perpendicular baseline estimates for September 24, 2002 trial plotted relative to the the calibration site at Connaught Range.

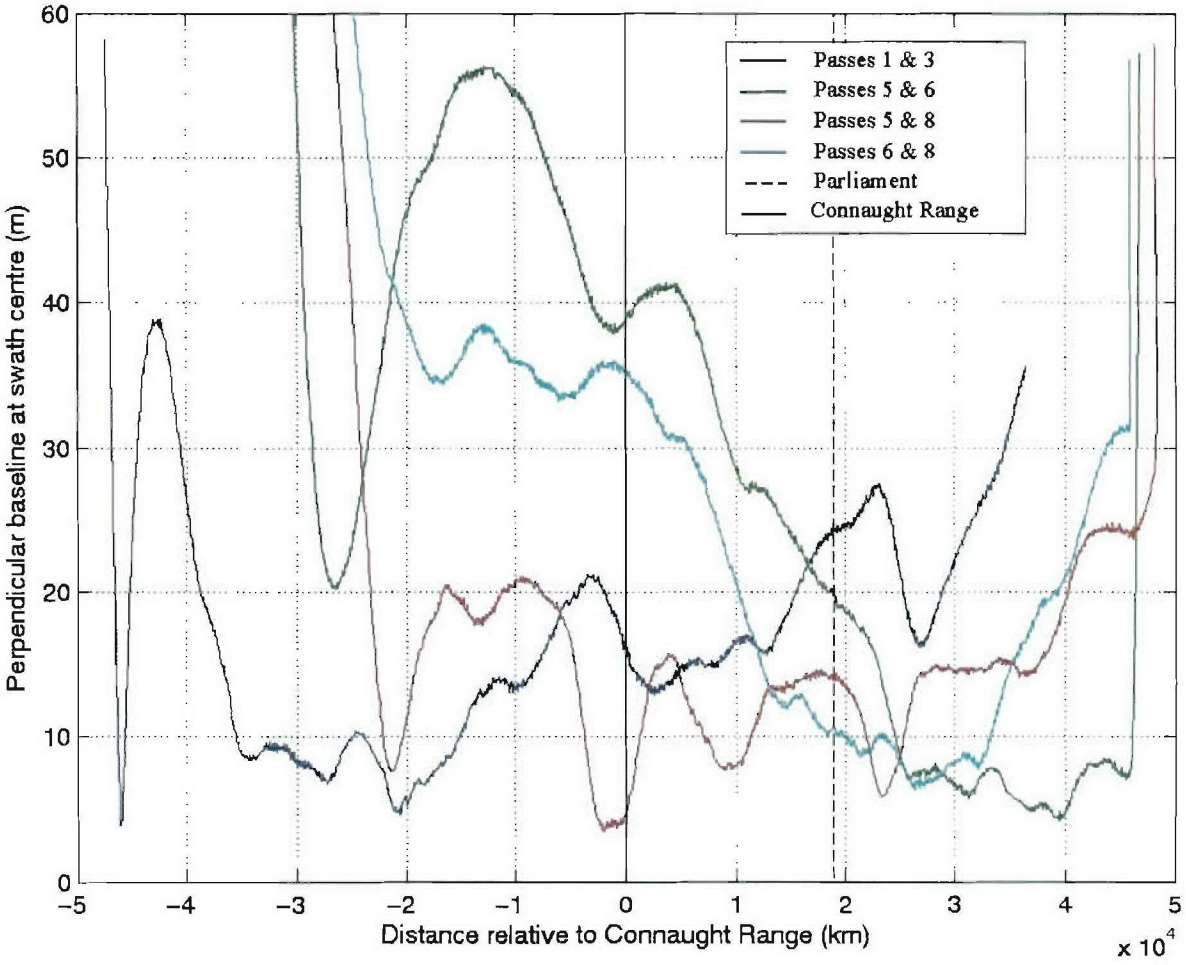

Figure 10: Perpendicular baseline estimates for other passes from the September 24, 2002 trial relative to the calibration site at Connaught Range.

Motion Compensation and Doppler Processing

Having reduced the number of passes to be processed to a more manageable level, processing continues with motion compensation and Doppler processing, and are detailed elsewhere [26]. The magnitude of one of the Petawawa and Ottawa passes, both with HH polarization, appear in Figure 11 and Figure 12. The motion compensation requirements for this experiment are particularly stringent. Repeat-pass interferometry requires knowledge of platform history to sub-wavelength accuracy [2]. Repeat-pass interferometry using the EC CV-580 was first attempted in 1993 [22]. The results showed that motion compensation fell short of the required accuracy, mainly due to limitations of the INS in use on the aircraft [22, 39]. Uncompensated aircraft motion caused undulations in the interferometric phase. With this current Pol-InSAR dataset, it is hoped that phase filtering will remove a sufficient amount of these phase artefacts to permit assessment of the results. In addition, since these phase undulations are common to the polarimetric signal, suitable phase differencing may also be employed to remove these artefacts.

The range focussing portion of the SAR processing of this dataset was carried out in real-time on board the CV-580 [39]. This had the unfortunately consequence of limiting the dynamic range of the data. As a result, bright targets have a tendency to saturate, distorting the phase of the signal. This could potentially also adversely affect polarimetric calibration.

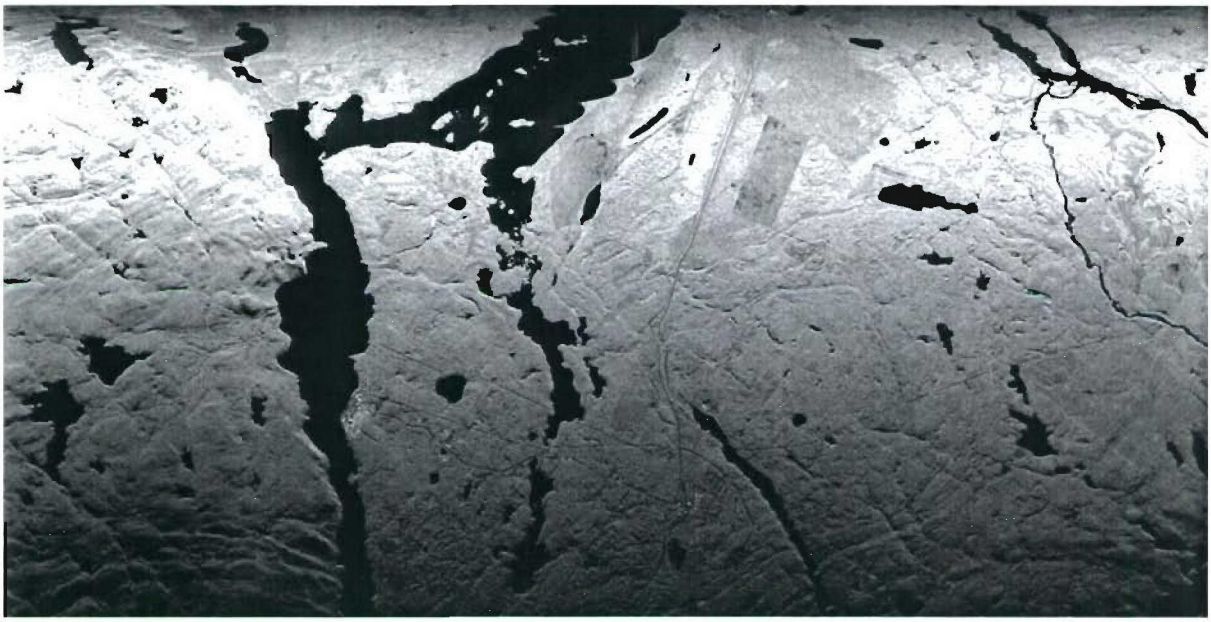

Figure 11: The magnitude of the pass 6 flight line with HH polarization from June 8, 2002 Petawawa trial. Near range is at the bottom of the image. The scene covers an area approximately 27 km long and 20 km wide.

Figure 12: The magnitude of the pass 6 flight line with HH polarization from September 24, 2002 Ottawa trial. Near range is at the bottom of the image. The Gatineau Hill are visible near the top central portion of the image. The scene covers an area approximately 38 km long and 20 km wide.

Polarimetric Calibration

The SAR data from both trials were polarimetrically calibrated using methodologies developed at CCRS [26]. Each pass included one, and only one, calibration site. The calibration equipment included at least one CR and one ARC. In all cases the flight lines were chosen so the calibration site would be located near the centre of the first half of the swath, at an incidence angle of approximately 57.5 degrees. The data can be considered calibrated within an incidence angle range of ±20° of the calibrated target location [79]. This range covers all except the nearest portion of the swath. Multipath effects between the antenna and its radome also corrupt the radar data at the near portion of the swath. The minimum incidence angle for good polarimetrically calibrated data remains uncertain. An RGB image of a chip of data from pass 6 of September 24, 2002 Ottawa trial is shown in Figure 13. The magnitude of the HH channel is portrayed in red; the VV channel is portrayed in blue; and the HV channel is portrayed in green.

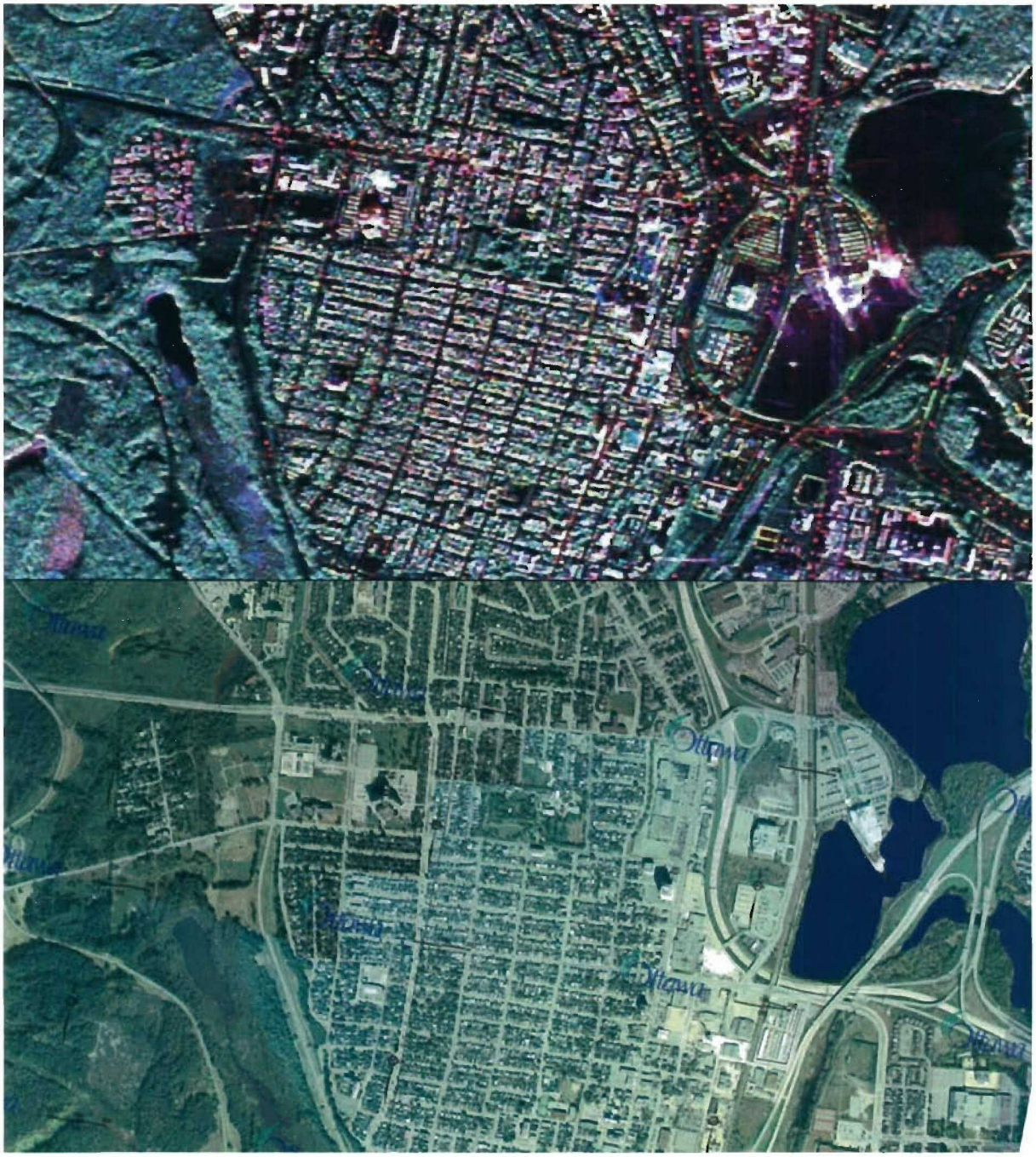

Figure 13: The top image is a small data chip from the pass 6 of September 24, 2002 Ottawa trial. The RBG image includes the magnitude of HH (red), VV (blue), and HV (green). Near range is at the bottom. The lower image is an aerial photograph of roughly the same region covered by the radar image. The scene covers an area approximately 38 km long and 20 km wide. The Gatineau Hill are visible on the left; the Casino de Lac Leamy is visible on the right. The aerial photograph is copyright The City of Ottawa and used by permisison.

Chip Selection and Interferometric Processing

The interferometric processing steps are outlined in Figure 14. All the interferometric (as well as the polarimetric interferometric) software were programmed in house and accept command line arguments. The interferometric processing is undertaken only on a small chip of the flight line at a time. The typical chip size is 8192 lines by 512 pixels, measuring approximately 3.3 km x 2.4 km at swath centre. For chip selection, the user identifies the geodetic coordinates (in latitude and longitude) of the region of interest, and identifies two passes that meet the perpendicular baseline requirements. The processor extracts the two chips of interest, and proceeds with the interferometric processing. Each of the four polarimetric channels undergo the same resampling and interferometric processing.

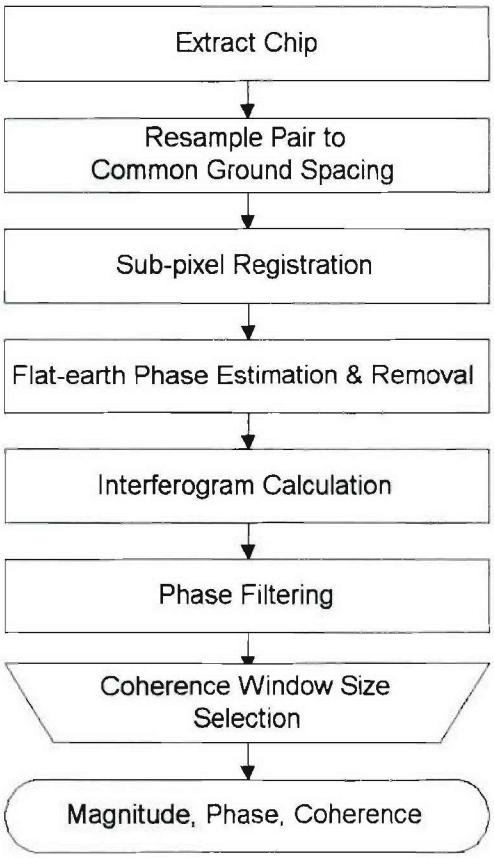

Figure 14: Flow chart of the Interferometry portion of the Pol-InSAR processing.

Data resampling is undertaken in two steps. The two chips are first resampled in azimuth to a common ground speed. Although the pulse repetition frequency (PRF) of the CV-580 is slaved to the ground speed and ideally should ensure the same azimuth spacing for the two passes, in these datasets the azimuth ground spacing differed by up to 10%.

The second stage in the resampling processing is two-dimensional sub-pixel registration of the interferometric pair. The magnitude of the two chips are correlated. The cross-correlation maximum is searched for within ±20 range pixels and ±1 azimuth lines. The cross-correlation results are fit to a polynomial. The chip designated as the slave chip is then resampled to a

quarter pixel accuracy to the master chip using a cubic spline interpolation. Resampling is first carried out in the range direction, and subsequently repeated in the azimuth direction.

The flat-earth phase removal eliminates the component of the interferometric phase due to a terrain of constant height above the ellipsoid. The flat-earth correction is calculated using the estimated antenna phase center positions. The main component of the variability in this phase correction originates from the constantly changing baseline along the line of flight. Residual errors in this phase correction are due to deficient compensation of the baseline variations, and are directly related to motion compensation limitations of the system. Some of these can be removed with phase filtering.

The flat-earth phase correction is applied to the designated slave chip prior to calculation of the complex interferogram and coherence calculation. Residual phase errors can be subsequently removed through phase filtering. The final outputs from this stage of the processing are the magnitudes of the master and slave chips, the interferometric phase, and the coherence for each of the four polarimetric channels. The coherence images are in comparatively reduced resolution because of the statistical nature of the coherence calculation.

Figure 15 shows images from various stages of the interferometric portion of the processing. The data chip was extracted from the VV channel of the Ottawa dataset. The scene is in the City of Gatineau, just north of Ottawa. Gatineau Park is visible on the left hand side of the image. Lac-Leamy is visible on the right-hand portion of the scene. The first row of images includes, from the left, the magnitude of pass 6 and the coherence between passes 6 and 8. White indicates high coherence: black indicates a total lack of coherence. The second row includes the raw interferogram phase and the estimated flat-earth phase. The third row shows flat-earth corrected phase, before and after phase filtering.

The interferometric phase and coherence between HV and VH from a single pass also provide useful information. Figure 16 shows the interferometric phase (top) and coherence (bottom) between pass 6 HV and pass 6 VH. The chip of data is the same as used for Figure 15. In general the coherence is very high and the phase is zero. The exceptions are for non-stationary targets (e.g. lakes and rivers) where the symmetry between HV and VH is lost, and those targets with a very low return (and therefore high SNR; e.g., some streets). The coherence can in turn be used to mask out non-stationary regions.

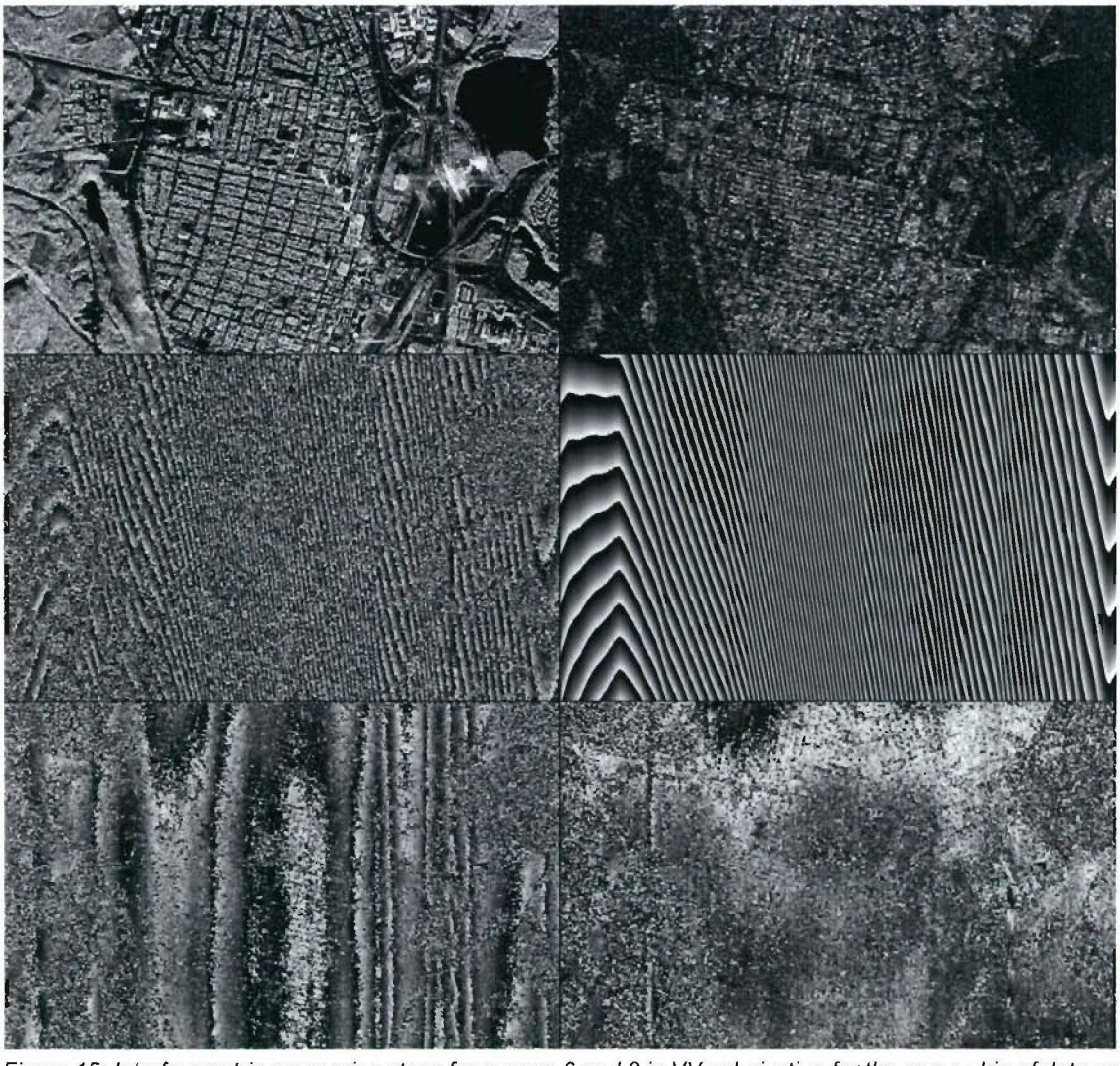

Figure 15: Interferometric processing steps for passes 6 and 8 in VV polarization for the same chip of data as Figure 13. In the first row are the magnitude of pass 6 and the coherence of passes 6 and 8. White indicates a high coherence; black a low coherence. In the second row are the raw interferogram phase and the estimated flat-earth phase. The phase is wrapped between $-\pi$ (in black) and $+\pi$ (in white). In the last row: the flat-earth corrected phase before and after filtering.

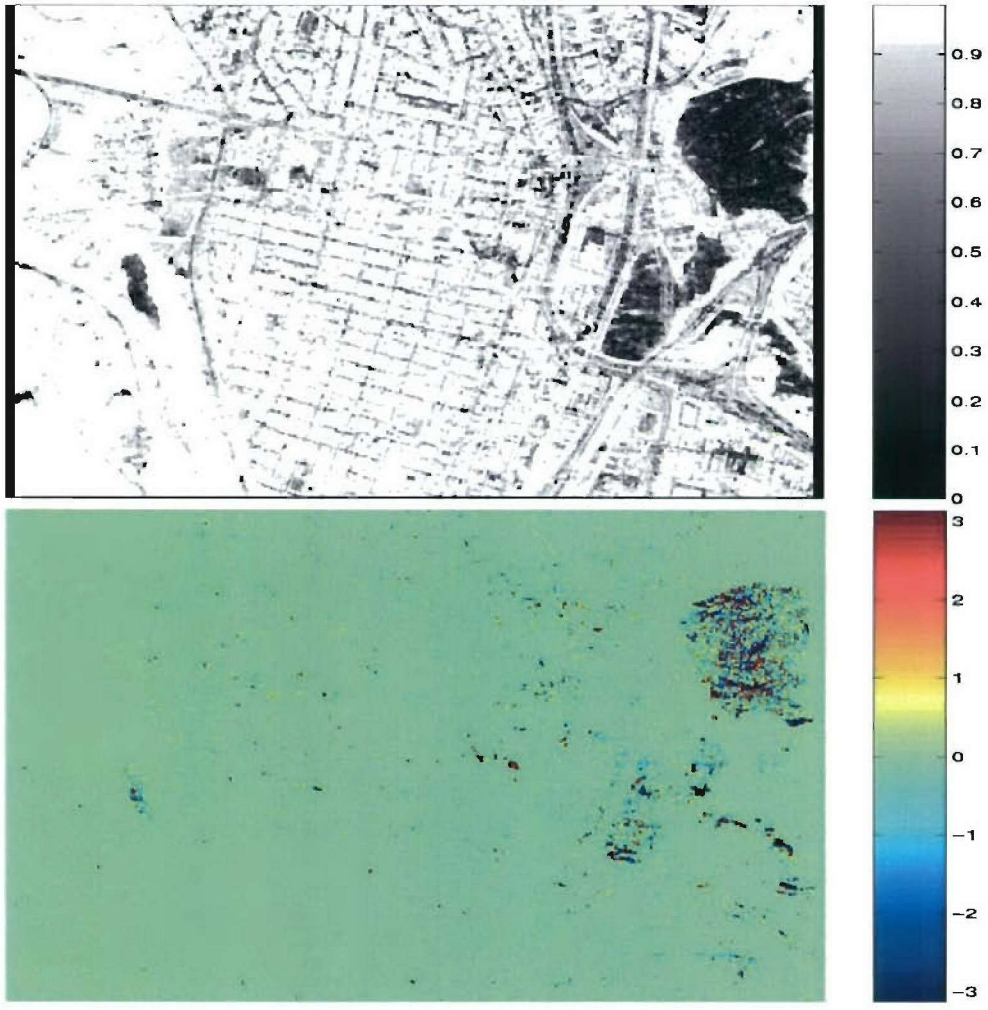

Figure 16: The coherence (top) and interferometric phase (bottom) between p6HV and p6VH for the same image chip as Figure 13. The phase varies between $-\pi$ and $+\pi$. The coherence varies between 0 for absence of coherence to 1 for fully coherent.

Polarimetric Interferometric Processing

At this stage, most of the polarimetric and interferometric processing has been accounted for. The various passes have been polarimetrically calibrated. Interferometric pairs with suitable baselines have been selected and processed. Given that each pair is polarimetric, the number of possible interferometric combinations between the two passes is very large. All these various channels of complex coherence (coherence magnitude and phase) are now available for comparison and analysis.

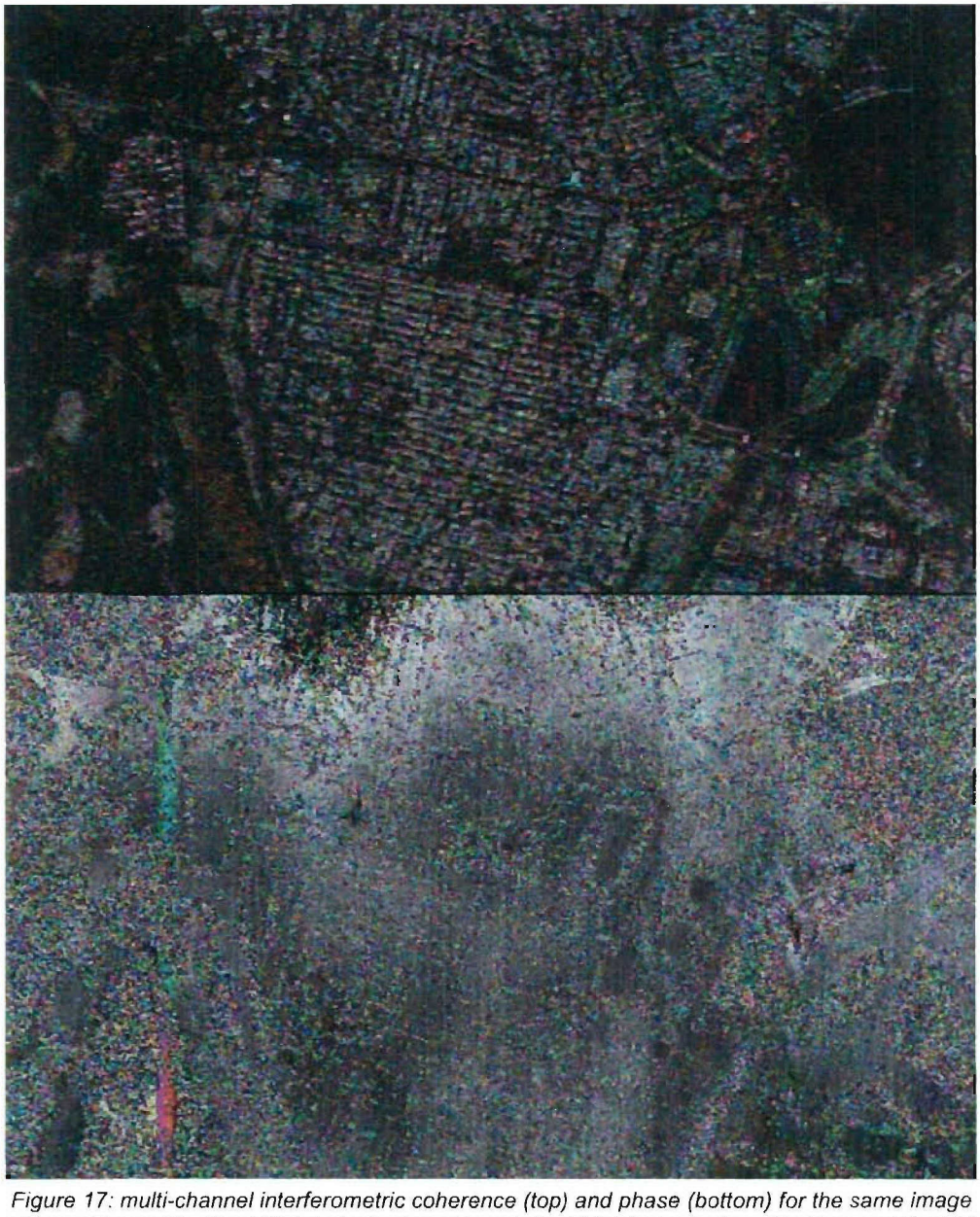

Figure 17: multi-channel interferometric coherence (top) and phase (bottom) for the same image chip as Figure 13. The HH data is displayed in red, the VV data is displayed in blue, and the HV data is displayed in green.

One quick way to compare three of the various polarimetric channels of the interferometric phase or coherence for an extended area is through the creation of a synthetic RGB image. The two images in Figure 17 show such a comparison, using the same chip of data selected in Figure 13. The top image is a comparison of the flat-earth corrected and filtered phase. The bottom image is a comparison of the coherence. In both cases HH, VV, and HV channels have been encoded in red, blue, and green, respectively. When the three channels are combined equally, the resulting color will be a shade of grey. Otherwise, the color displayed will point to the dominant (or subordinate) channel or channels. The colour wheel shown in Figure 18 will help in the interpretation of the interactions between the colours. An absence

of red appears cyan: the absence of green: magenta; and the absence of blue: yellow. For example, a relatively strong HH scatterer will appear red; relatively weak HH scattering will appear cyan.

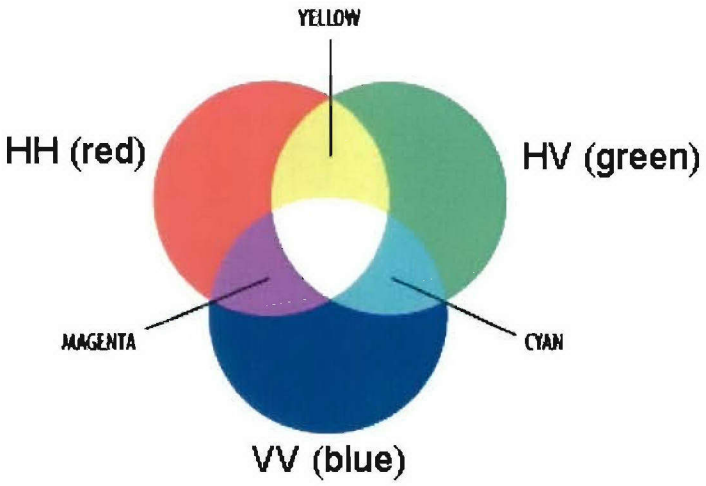

Figure 18: This colour wheel aids in the interpretation of the interaction between the RGB colours.

Data Analysis

Following data collection and processing, several polarimetric repeat-pass data collects acquired over 3 days using the CV-580 radar are available for analysis. Six passes were collected on June 5 before the mission had to be aborted due to strong winds. Of the six, one pass was collected flying the wrong track, leaving five passes for potential Pol-InSAR use. Because of the limited number of available passes, the June 5 dataset set aside in favour of the June 8 dataset.

Nine flight lines were collected June 8. These nine passes lead to 36 possible repeat-pass combinations. Out of these (as seen in Figure 7 and Figure 8), only three pairs had a perpendicular baseline less than 30 meters in the general region of interest, and therefore suitable for interferometry. One of these pairs, namely passes 1 and 6, was found to have a very poor coherence (high phase noise), and was not suitable for further interferometric processing. The Petawawa data set provides Pol-InSAR data in a rural setting, with large regions of variable forest cover. Passes 6 and 9 had good coherence, and was the main pair used for the Pol-InSAR analysis. The general coverage of the pass (see Figure 11) included many rivers and lakes, a large cleared area at the CFB Petawawa, isolated structures, and a few radio and water towers. Unfortunately the coverage just missed the town of Petawawa. Two chips were extracted from this interferometric (and polarimetric) pair. This chips are approximately 2.0 km x 3.3 km in size. One is centred on the calibration site at the clearing of CFB Petawawa. The other chip is centred close to Perch Lake. The RGB magnitudes, coherence, and phase images for both are shown in Figure 19 and Figure 20 respectively. In the magnitude images, the HH data has been coded red, the VV data has been coded blue, and the HV data has been coded green. In the interferometric phase and coherence images, the HH–HH pair has been coded red, the VV–VV pair has been coded blue, and the HV–HV pair has been coded green. It is a succinct, though at times confusing way of representing the results from the Pol-InSAR processing.

The third and last day of data collection occurred over the city of Ottawa on September 24, 2002. Eight passes were collected that day, under relatively low wind conditions (Figure 3). The eight passes lead to 28 possible repeat-pass combinations. Out of these (as seen in Figure 9 and Figure 10), four pairs had perpendicular baseline suitable for further Pol-InSAR study. The perpendicular baselines spanned a range between just less than 5 meters to over 30 meters. From (4), this provides for a variety of height to phase sensitivities. The coverage (shown in its entirety in Figure 12) includes many interesting sites. It includes large portions of the cities of Ottawa and Gatineau, the Gatineau Park, the experimental farm in Ottawa, and more rural regions to the west of Ottawa.

In this chapter, the data collected during these trials will be analyzed for potential applications. The chapter is divided into four sections: vegetation and forest cover, buildings and the urban environment, isolated and manmade targets, and finally velocity estimation. For each of these sections, the impact of the three key variables of wavelength of the radar, resolution of the sensor, and temporal separation of the InSAR pair will be emphasized. The analysis of this CV-580 data together with published results, will help establish potential future applications using upcoming radar systems, such as RADARSAT-2 and PolSAR.

Vegetation and Forest Cover

The main portions of the recent literature on polarimetric SAR interferometry focuses on forestry applications. Pol-InSAR has found some success in measuring forest height and estimation of biophysical parameters (such a biomass) of forested areas [54, 80]. Pol-InSAR has also successfully been used to enhance the detection of scatterers (or targets) hidden beneath foliage [7]. These applications are very wavelength dependent. The applications are made possible by the different scattering signatures at L-band (or S-band) between, on one hand, the main volume of the tree (the leaves and branches), and on the other hand, the principal tree trunks and ground.

By contrast, at the C-band wavelength of the CV-580 radar, the leaves and small branches of trees normally completely attenuate the signal [81]. The ground beneath the forest, and therefore scatterers on the forest floor, are generally invisible to the sensor at C-band or shorter wavelength. Estimation of the biophysical parameters of the trees using Pol-InSAR is therefore not feasible at C-band.

On the other hand, retrieval of the physical parameters of short crops at C-band, or possibly detection of a strong scatterer beneath the crops, is achievable. In a recent article [2], the ground vertical position and crop height (but not the extinction coefficient) for corn crop were retrieved using an inversion technique similar to the method used for forests. For this type of scatterer the C-band wavelength could prove ideal, although applications for such a tool seem rather limited.

The data obtained from both the Petawawa and Ottawa sites generally support these conclusions. The two chips of data extracted from the Petawawa mission, shown in Figure 19 and Figure 20, reveal that the coherence from the three polarimetric channels is totally lost in forested areas. The radar signal has apparently been unable to penetrate the canopies in the area. In contrast, areas of clearing that are often covered by grasses of various kinds, have a relatively high coherence. In some of these clearings (especially the ones shown in Figure 20) the RGB coherence image is also coloured. This signifies that the coherence of one or two of the RGB channels is higher than the other(s). In turn, this indicated that there are multiple sources and types of scatterers within the same footprint in these regions. It is likely there are two sources of scattering: one from the vegetation itself; the other from ground beneath the vegetation.

Data from the Ottawa trial also supports these general conclusions. Portions of the Gatineau Park appear along the left side of Figure 13. The corresponding RGB phase and coherence images (with HH coded as red, VV coded as blue, and HV coded as green) are given in the top and bottom images (respectively) of Figure 17. The regions of the Park covered by trees are decorrelated in all three channels. There are a few openings visible in the forest. These do have relatively high coherence, and correspondingly low phase noise. A closer look at the coherence reveals that the coherence is coloured. The two clearings in the lower left portion of the image have pinkish and reddish tones, signifying (see Figure 18) a lack of green and correspondingly a lack of HV return. HV is normally associated with scattering from a random media. Hence, the inference is that these two clearings are covered with low vegetation that has a strong orientation. The difference between the pink and red colours, when intermixed with noise is rather subtle. A red coherence would signify strong HH return, whereas the pink would signify strong HH and VV returns.

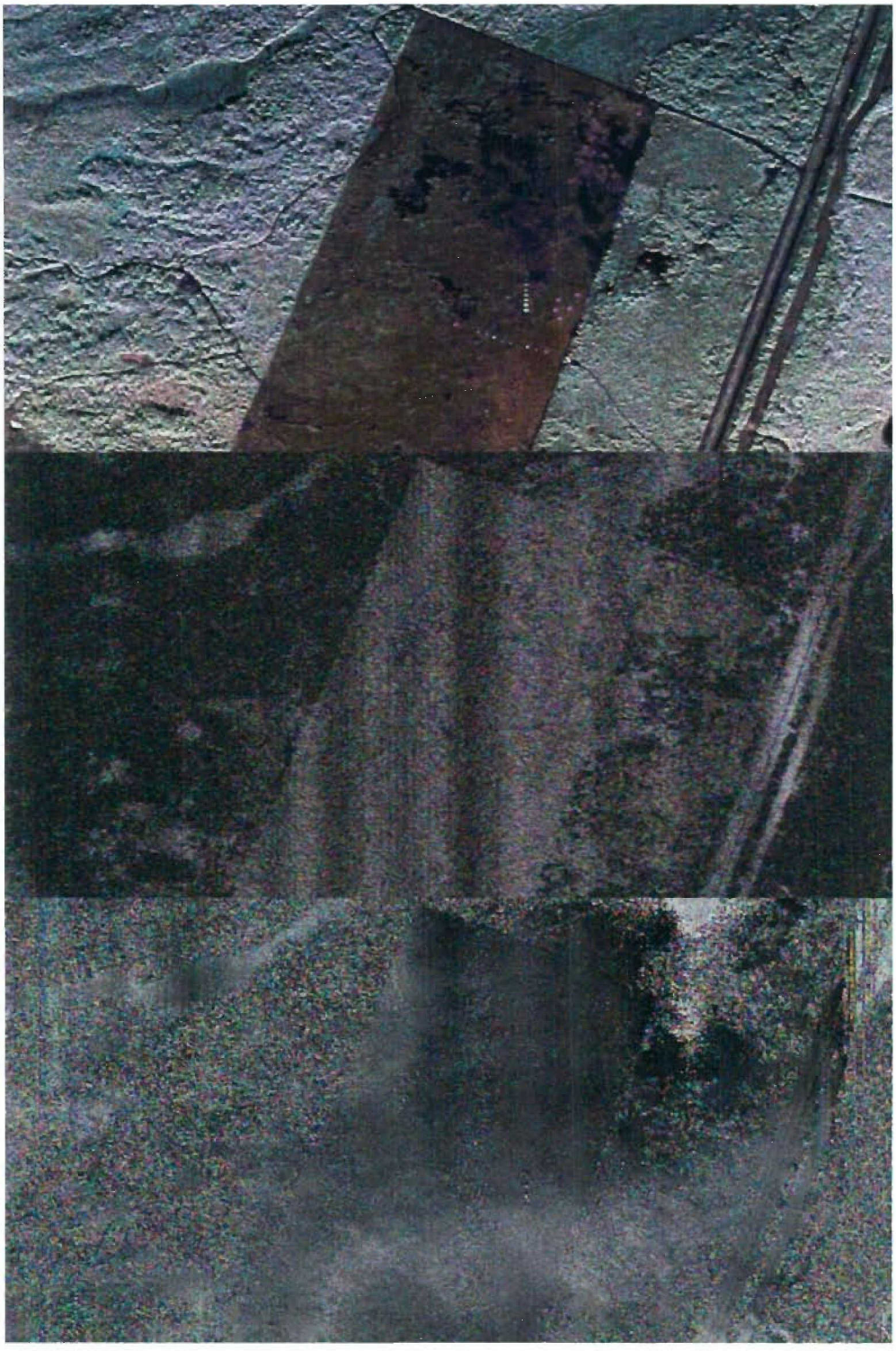

Figure 19: From the top, are the magnitude, coherence, and phase from the passes 6 and 9 Petawawa pair. In each image, the HH, VV, and HV channels are coded as red, blue, and green, respectively (see Figure 18). The scene includes the calibration site, just left of centre.

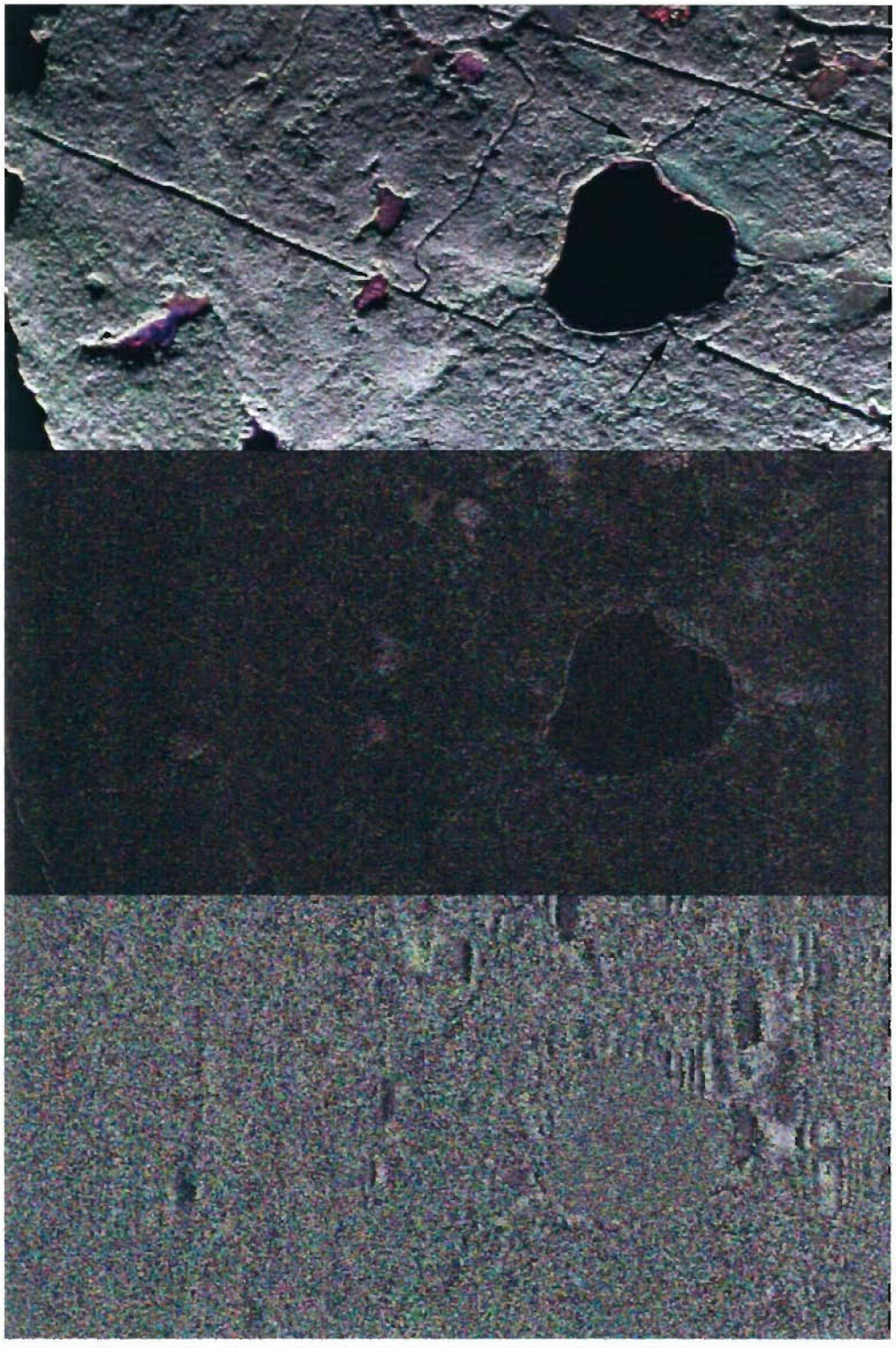

Figure 20: From the top, are the magnitude, coherence, and phase from the passes 1 and 9 Petawawa pair. In each image, the HH, VV, and HV channels are coded as red, blue, and green, respectively (see Figure 18). The scene includes Perch Lake and two radio towers that are 46 metres high by the lake (see arrows).

Pol-InSAR has been successful in retrieving the height and topography of cornfields [2]. Similarly, there is the potential to use Pol-InSAR to estimate the height of low vegetation such as those that cover some of these clearings near Petawawa and in Gatineau Park. There is also the potential for using Pol-InSAR to filter out the scattering from the vegetation, thereby accentuating the signal scattered from the beneath the vegetation.

RADARSAT-2 and PALSAR are two upcoming satellites that will be polarimetric. They will also be capable of interferometry, though with a large temporal baseline of 24 and 46 days, respectively. They are both also capable of Pol-InSAR. For vegetation and forest cover applications, RADARSAT-2, with its C-band sensor, should have similar characteristics to the CV-580, and a similar 20 km swath width. Its lower 9-meter resolution is not a limitation in imaging extended areas. The 24-day minimum repeat for SRI will severely impact temporal decorrelation, as it has impacted RADARSAT-1.

PALSAR's L-band wavelength is much more suited to the Pol-InSAR forestry applications elaborated by Cloude and Papathanasiou [11, 51]. Its 46-day repeat pass is largely tempered by its longer wavelength. Using Pol-InSAR to accentuate scatterers from the forest floor may be one of its useful applications.

Buildings and the Urban Environment

The literature contains very few references to urban environment and building characterisation using Pol-InSAR tools. Zandoná Schneider *et al.* [86] describe a theoretical study where single-baseline Pol-InSAR data is used to estimate the height of buildings. Guillaso *et al.* [23] detailed an experiment estimating the height profile of buildings using Pol-InSAR techniques with DLR's L-band E-SAR airborne sensor (having a slant-range resolution of 2.5 m and an azimuth resolution of 1.5 m [30]). The site chosen for their experiment was a semi-urban setting. It is noteworthy that Guillaso *et al.* made multiple use of the Pol-InSAR data. They used an unsupervised PolSAR classifier to distinguish regions of single bounce, double bounce, and volume scattering. They spectrally combined the repeat-pass InSAR data to achieve super resolution. Finally, they used the full Pol-InSAR dataset to distinguish the heights of the scatterers. The combination of these three components provided them with tools for improved accuracy of determining the shape, orientation, and height profile of local buildings.

The Ottawa dataset collected on September 24, 2002 contains many urban and semi-urban scenes. The Casino chip depicted in Figure 13, Figure 15 and Figure 17 shows parts of the City of Gatineau. The coherence (upper image in Figure 17) is relatively high over the buildings. Besides loss of coherence over treed areas due to temporal decorrelation, the coherence is also relatively low over the road network. The backscatter from streets tends to be low, resulting in higher phase noise and consequently lower coherence. The coherence over buildings is multicoloured reflecting the large variety of scatterers within the scene.

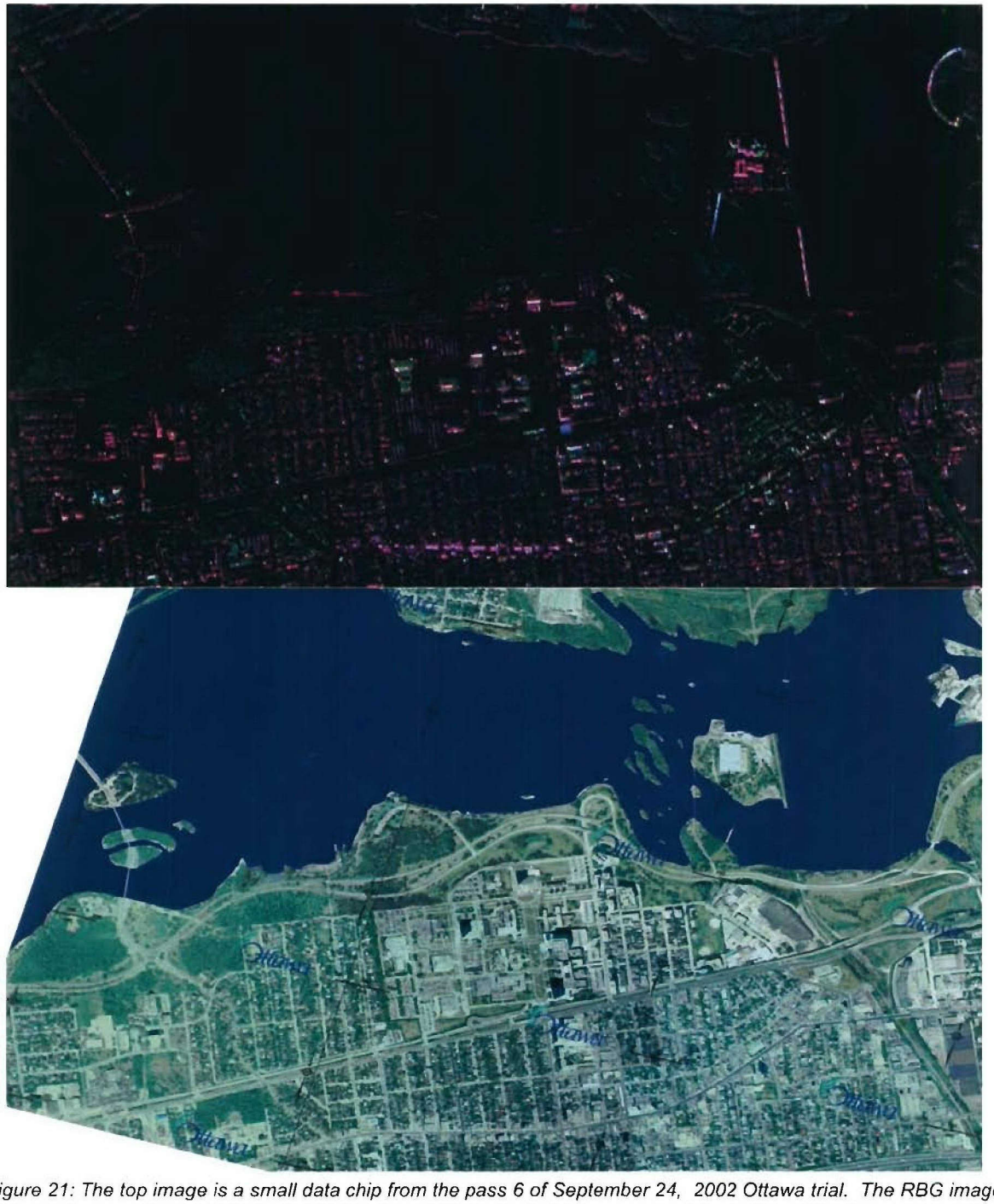

Figure 21: The top image is a small data chip from the pass 6 of September 24, 2002 Ottawa trial. The RBG image includes the magnitude of HH (red), VV (blue), and HV (green). Near range is at the bottom. The lower image is an aerial photograph of roughly the same region covered by the radar image. The scene covers an area approximately 38 km long and 20 km wide. Tunney's Pasture is at the scene centre. The aerial photograph is copyright The City of Ottawa and is used with permisison.

Figure 22: This water plant complex is situated just north of Tunney's Pasture, on the Ottawa River. The aerial photograph at the top was taken in June 2003. The lower three images are the magnitudes of |HH+VV, |HH-VV|, and |HV| from Ipass 6 of September 24, 2002 acquisition. These are generally interpreted as scattering from odd number of radar bounces, from even number of radar bounces, and volumetric or random scattering.

The water treatment plant in the middle of the Ottawa River in Figure 21, is shown in detail in Figure 22. At the top is an aerial photograph of the treatment plant. At the bottom (from left) are the magnitude radar image of |HH+VV|, |HH−VV|, and |HV|. Comparing the three radar images clearly demonstrates that different parts of the structures have different scattering characteristics. Given sufficient SNR, a suitable perpendicular baseline, and accurate knowledge of that baseline (and adequate resolution of the sensor), the height difference between the various scatterers that are distinguished by polarimetry, could potentially be measured.

Another chip of data from the same passes 6 and 9 pair, Figure 21, shows the Tunney's Pasture region of the City of Ottawa. The upper image is the magnitude of HH, HV, and VV depicted in the RGB colours. Near range is along the bottom of the image. The lower image is an aerial photograph of the same region. Tunney's Pasture is located in the central portion of the image. The neighbourhood of Westboro is located to its south, and the Ottawa River to its north. In the middle of the Ottawa River is Ottawa's Water Treatment Plant. The urban area is predominantly pink in tone in the magnitude image, reflecting the strong HH and VV (odd and even bounce) nature of the dominant scatterers in the scene. The notable exceptions are buildings that are oriented roughly at a 45° angle to the sensor. These appear predominantly green in the magnitude image, signifying dominant HV, or random scattering. Kimura *et al* observed similar polarization orientation effects in urban areas on SAR data as X- and L-bands [33]. The aerial photograph shows that these neighbourhoods are not significantly different physically from the others. Their particular orientation with respect to the sensor obviously results in the predominance of HV scattering.

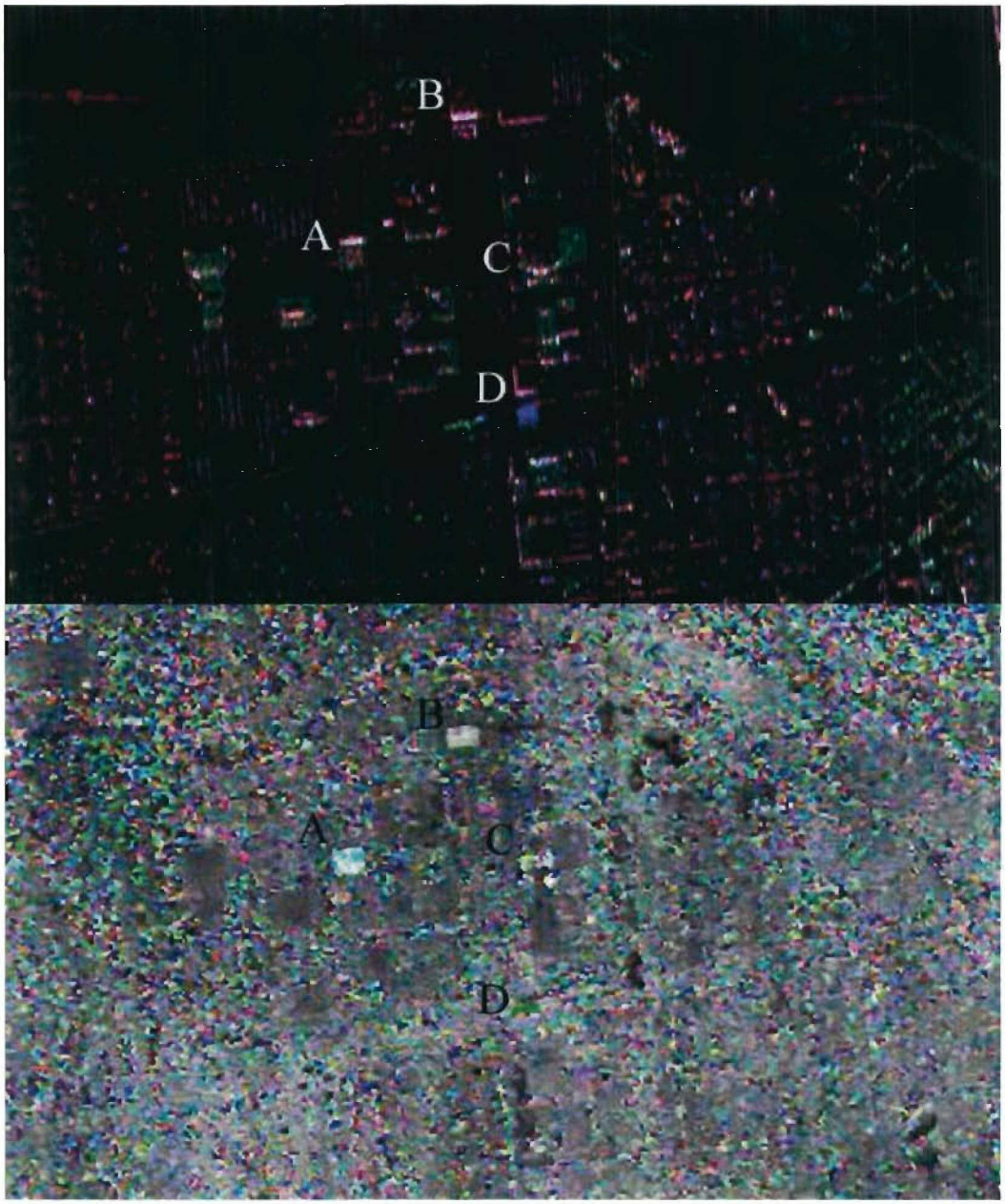

Figure 23: This detail from Figure 21 focuses on the buildings of Tunnery's Pasture. The RGB magnitude is on top; the RGB phase from the passes 6 and 8 Pol-InSAR pair on bottom. See Figure 18 for an interpretation of the colours. 'A' is the Jeane Mance Building at 77m in height, 'B' is the Brooke Claxton Building at 57 m, 'C' is the Jean Talon Building at 53 m, 'D' is the R.H. Coats Building at 99 m [19, 74].

A more detailed view of the buildings in Tunney's Pasture is shown in Figure 23. The upper image is the magnitude of HH, HV, and VV depicted in the RGB colours. The lower image is the flat-earth corrected and filtered phase of the HH, HV, and VV InSAR pair, also depicted in the RGB colours. The phase of the Pol-InSAR image is very noisy in regions where the magnitude of the backscatter is low (e.g. the streets) or where volume decorrelation from trees

dominates the radar footprint. By contrast, scattering from buildings is generally characterized by relatively uniform phase.

The taller buildings that make up Tunney's Pasture are of particular note. Four of the taller of these buildings are clearly discernible in the phase image. These are marked 'A' through 'D' in the figure. 'A' is the Jeane Mance Building, 'B' is the Brooke Claxton Building, 'C' is the Jean Talon Building, 'D' is the R.H. Coats Building. In radar imaging, tall buildings are distorted and subject to significant layover. The top of the building, being closer to the sensor than the bottom, will be displaced closer to the sensor than the bottom of the building in the image. Furthermore, the top of the building, the side of the building facing the sensor, and the part of the ground immediately in front of the building (relative to the sensor) overlap in the radar image. This results in the radar footprint being dominated by one, two, or all three of these overlapping regions, depending on the relative strength of the scattered radar signal from each of the three components of the layover region.

The roof of the Brooke Claxton Building (building 'B' in the phase image of Figure 23) is clearly discernable by its distinctly lighter shade of grey from its surroundings. The clear delineation of the roof signifies that this component of the radar scattering is the dominant component in the layover region. The phase change between the roof and the surrounding area is proportional to the building height and given by (4). Table 5 lists estimates of the height change between elevated scatterers and the ground for the Jeane Mance Building (building 'A') and the Brooke Claxton Building (building 'B').

Table 5: Estimated height change between elevated scatterers and ground for targets labelled in Figure 23. Baseline uncertainly and phase noise are the primary contributors to the standard deviation.

SCATTERER	BUILDING HEIGHT (*m*) [19, 74]	$\Delta H_{2\pi}$ HEIGHT AMBIGUITY (*m*)	ΔH HEIGHT CHANGE (*m*)		
			HH	VV	HV
JEANE MANCE BUILDING (BUILDING 'A')	77	96±7	73±19	67±13	67±14
CYAN SCATTERER AT THE JEAN MANCE BUILDING	—	96±7	38±16	—	—
BROOKE CLAXTON BUILDING (BUILDING 'B')	57	77±16	62±15	61±11	59±12

The principle difficulties in estimating the height of the building from the phase change are threefold. First, the phase difference is known only modulo 2π. In this case, the small perpendicular baseline results in a relatively large 2π height ambiguity. This large height ambiguity makes it easier to determine the ambiguity and estimate of the height of the scatterer. From Table 5, the height ambiguity for building 'A' and 'B' are 96 ± 7 meters and 77 ± 16 meters, respectively.

The second difficulty in accurate estimation of the height is the uncertainty in the perpendicular baseline measurement. From (4), it can be seen that the height is very sensitive to uncertainties in the perpendicular baseline.

Finally the third difficulty is the phase noise. The important decorrelation factors are listed in (7). The resolution of the sensor is obviously also an important consideration.

The estimates for the height of building 'B' for each channel, using (4), are listed in Table 5. Building 'B' is approximately 20 stories tall. If each story is 10 feet, the building would be 61 meters high, which is very close to the value estimated from interferometry. The grey tone of the phase image of the roof of building 'B' also signifies that all three of polarimetric components that make up the RGB image are being scattered in roughly equal proportion from the roof of the building. This does not hold for the other tall buildings in Figure 23, marked 'A', 'C', and 'D'. The phase at the roof of building 'A' contains regions of cyan within the grey tones of the roof. Cyan represents a change in the HH scatterer. Within the layover region that includes the roof of building 'A' is another strong cyan scatterer. The estimates of the height above the ground of these two different scatterers are listed in the second row of Table 5. Building 'A' is 77 meters tall. This agrees very well with the height as calculated from the grey portions of the scatterers. The height of the cyan portions of the scatterering at and near the image of the roof of the building is an estimated 38 ± 16 meters. The large standard deviation reflects difficulty in estimating the phase because of the small size of the scatterer relative to the resolution of the sensor.

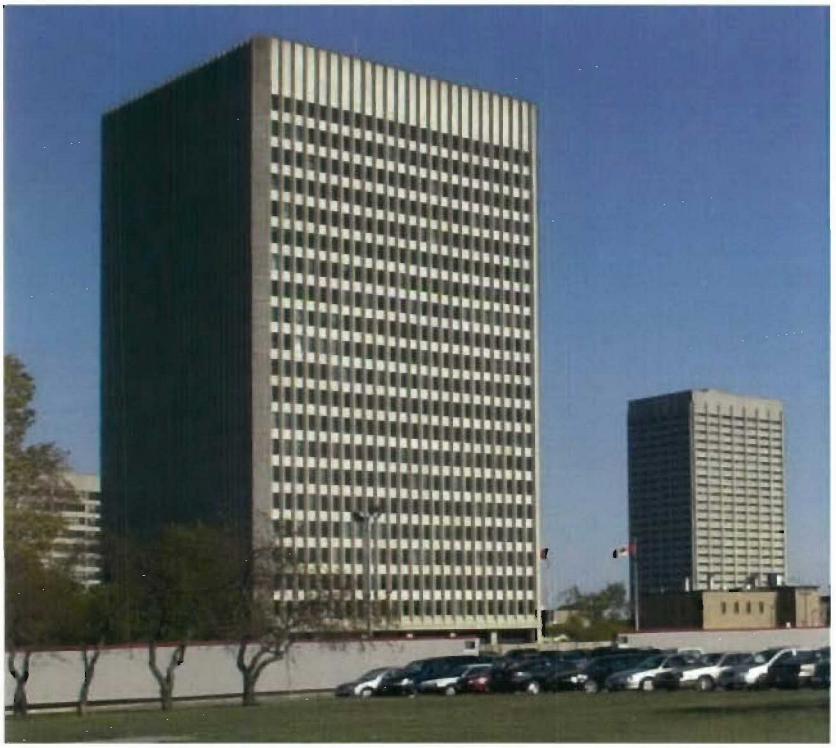

Figure 24: A photograph of the north-west side of buildings 'A' (on the left) and 'B' as labelled in Figure 23. The photograph was taken on the same day as the data acquisition; September 24, 2002 (photograph is courtesy of J. Lang). Note the two flag poles near the front (south side) of the building 'A' and lamp post on the west side.

There are scattering from tall light poles that are in front (south end) and on the west side of the building (see Figure 24). The light poles in front of building 'B' is 8-10 meters in height; the one to the west side is 10-14 meters high. The slight discrepancy between the observed

and measured heights may be due the HH scattering from the roof of building 'B' mixed in with the scattering from the light poles. Note, there are light poles in front of building 'A', but these are only approximately 3-4 meters high.

Scattering from buildings 'C' and 'D' show even more complex phase patterns. Unlike the previous two buildings, these two are behind (relative to the sensor) other shorter buildings and structures. The layover region from 'C' and 'D' are intermixed with scatterers from these smaller structures. This complexity is common in heavily urbanised neighbourhoods, and is a limiting factor for the applicability of Pol-InSAR in urban areas. The rather coarse resolution of the CV-580 sensor is also a limiting factor to potential applications in such regions.

Isolated Manmade Structures

There are few references in the literature describing the use of Pol-InSAR for detection or characterization of isolated and manmade structures. Dubois-Fernandez *et al.* [18] detail an experiment where X-band sub-meter resolution airborne Pol-InSAR data is collected over an urban area. They demonstrated that Pol-InSAR is potentially capable of identifying and characterizing manmade structures such as light and electric poles through their complex Pol-InSAR signatures. The top of light poles was found to be dominated by HH and VV scattering; whereas the ground contribution was dominated by HV scattering. The light poles were clearly identifiable from a combination of their polarimetry and complex coherence signatures.

Figure 25: SAR interferometric imagery pair from the CV-580 of Ottawa test field on September 24, 2002 (R: HH, G:VV, B:HV). The arrows indicates the site of the crashed airplane. (a) Pass 6. (b) Pass 8. (from [42])

Lukowski *et al.* [42] describe the use of the CV-580 Pol-InSAR data collect on September 24, 2002 as a tool for reducing the false alarm rate for detection of downed aircrafts. The Ottawa data collect detailed in this report included the site of a crashed Cessna-172. The crash site is located near the site used for calibration of the PolSAR data. The PolSAR imagery from pass 6 and pass 8 over the site is shown in Figure 25. According to statistics for crashes of small aircraft, the dihedral structure of the tail section, which is often the most readily detected, is the part of the airplane most likely to survive a crash intact. In Figure 25 the crashed airplane was oriented in the True North direction, in a direction that is over 60 degrees from the optimum heading for the radar to detect the dihedral structure of the tail. Using certain polarimetric tools, the dihedral scattering in the polarimetric image was accentuated. These scatterers are identified in Figure 26 (in blue) for the crash site from the line 1 pass 6 polarimetric data (top image, a), from the line 1 pass 8 polarimetric data (middle image, b). Dihedral scatterers with high coherence can be isolated using coherence analysis. These are shown in the bottom image, c, of Figure 26. Quite a few false alarms can be identified in each

of the three images. But by using a combined algorithm, the false alarm rate can be drastically reduced. In this case the false alarm rate was eliminated altogether, and the site of the crashed aircraft was uniquely identified.

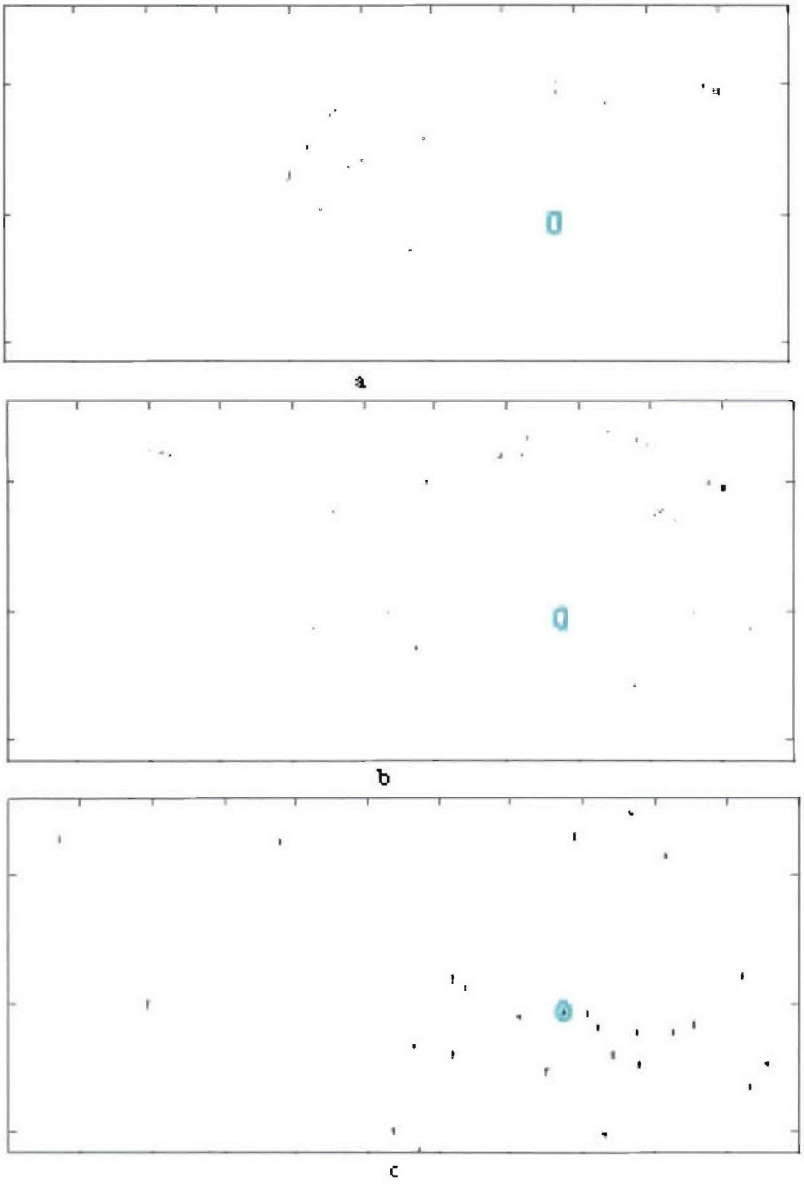

Figure 26: Target Maps. Blue ovals indicate the location of the crashed aircraft target. (a) Pass 6 from Pol. (b) Pass 8 from Pol. (c) Passes 6 and 8 from interferomeric coherence analysis (from [42]).

Besides the crashed Cessna-172, several other isolated and manmade targets of opportunity appear in the Petawawa and Ottawa imagery. Streetlights along the roads near Casino de Lac Leamy (top image of Figure 13) and on the bridge that connect the cities of Ottawa and Gatinueau (top image of Figure 21) can be clearly identified through their polarimetric signatures. They appear red (or pinkish red) in the RGB magnitude images; indicating relatively strong HH scattering. The strong HH (and weak HV) scattering is likely due to the

shape of the streetlights. Photographs of several streetlights along the road and bridges of the cities of Ottawa and Gatineau appear in Figure 4. Other targets of opportunity include two 46 metre tall radio towers near Perch Lake (indicated by the arrows in the top image of Figure 20), and several antenna dishes and towers on the CRC campus.

Unfortunately, characterizing these types of structures with the CV-580 Pol-InSAR is system limited. Resolution is one key limitation. Some of the parameters for the CV-580 sensor are summarised in Table 1. The resolution of the CV-580 is limited to 5.7 meters in range: the slant range pixel spacing to 4 metres (5 meter ground range spacing at swath centre). The backscatter from a 15 metre tall streetlight or 46 metre radio antenna stand is limited to only a very few range pixels; certainly an insufficient number for any statistical calculations or averaging for noise reduction.

Target saturation due to the limited dynamic range of the CV-580 data is another major system limitation. The CV-580 is unusual in accomplishing range focusing in real time using a Surface Acoustic Wave (SAW) technology [39]. After analog to digital conversion, the data is then stored on tape using 6-bit real and 6-bit imaginary samples per pixel. The combination of small storage space per pixel and relatively large dynamic range of range-focused data puts a severe limitation on the dynamic range of the backscatter. Isolated man-made structures in an environment of low backscatter are particularly prone to signal saturation. When the signal saturated, the polarimetric signature of the scatterer is lost. Several of the isolated man-made targets that were targets of opportunity do appear to be saturated. Recent upgrades to the CV-580 have removed the real-time range processing of the CV-580 data (though only at the expense of range resolution).

Due to a combination of these two, and other limitations, the CV-580 Pol-InSAR data collected in 2002 was not suitable for isolated manmade structure characterisation. The conclusions of Dubois-Fernandez *et al.* [18] could not be duplicated with this dataset.

Velocity Estimation

From the Ottawa trial of 24 September 2002, target detection and velocity estimation from PolSAR data are investigated, and the results are presented in this section. As discussed previously, a total of eight images were acquired during the experiment. Out of these, the known moving targets can be seen in six of the images. Each of these images is analyzed. In addition, several techniques to estimate the target velocity are studied.

Target Detection

Several methods of detecting the presence of moving targets exist [6], of which two are adapted in this study. If the target is sufficiently strong, the target trajectory can be seen in the range compressed data. For a static target, the trajectory will be nearly horizontal with a slightly hyperbolic shape. If it is moving, it will have a noticeable slope. The velocity can be estimated from the slope of the trajectory.

Another detection method is clutter cancellation analysis. If reciprocity is assumed, then HV = VH (i.e. the HV channel signal is identical to the VH channel signal), then the formation of |HV−VH| for the final image should cancel the clutter if the PolSAR system is perfect. HV

and VH are measured at slightly displaced times, but the images are co-registered by interpolation of the range compressed data. For this study, the |HV−VH| was formed to determine whether there were any imperfections in the co-registration process or other non-reciprocal effects which could aid in the detection of a moving target. This method will cancel static clutter, which is a great advantage since the moving targets will be smeared and their amplitude correspondingly reduced. We will consider these two methods in greater detail.

Trajectory Analysis

The motion compensated, range compressed (non-azimuth compressed) images are shown in Figure 27. A few trajectories can be seen in these images. Target trajectories can be seen in range compressed images only when the target returns are very strong. For this reason, most moving target trajectories are not visible. The trajectories from static targets have no slope. However, some are from moving targets. Figure 28 is a part of Figure 27. In these Figures, the trajectories of *Tr1* and *Tr2* are horizontal along 2 range bins with a slightly parabolic shape. These two trajectories are from static targets. However, there is a clear slope across slant range over 4 range bins of trajectory *Tr3*. This slope is due to velocity of the target and can be used to estimate the velocity. The trajectory from a moving target is also smeared; therefore, the magnitude is lower than that from a static target.

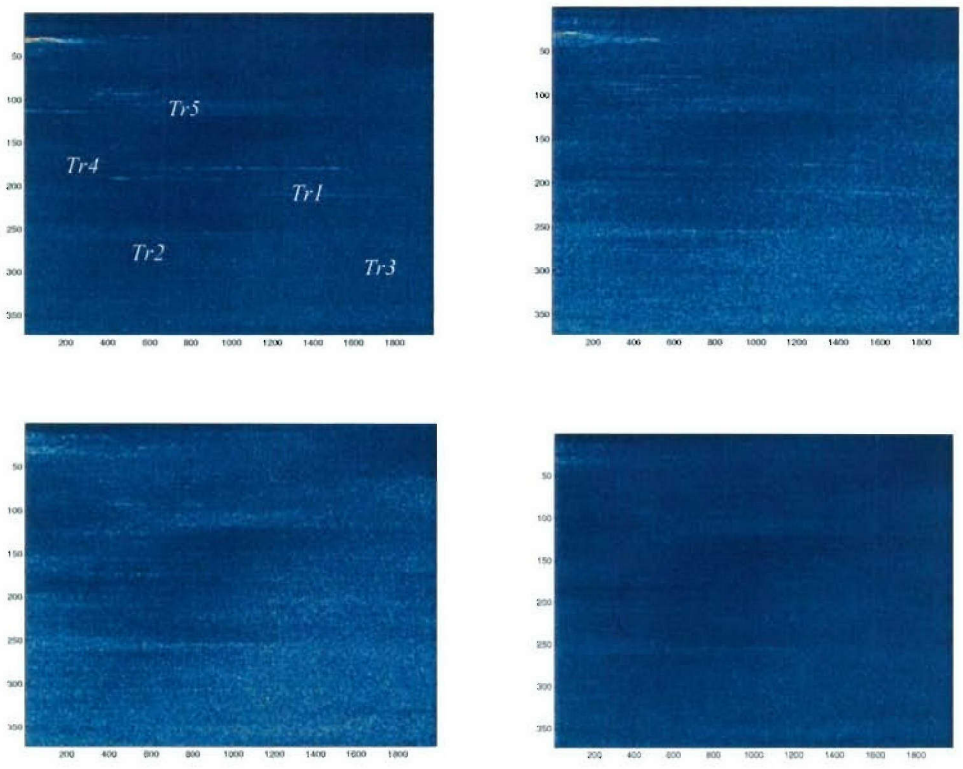

Figure 27: Range compressed and motion compensated (non-azimuth compressed) images of the moving target site in pass 8 from September 24, 2002 trial. Clockwise from top left are the |HH|, |VV|, |HV|, and |VH| images. The vertical axis represents range pixels; the horizontal axis represents azimuth lines. Tr1 through Tr5 are five different visible trajectories.

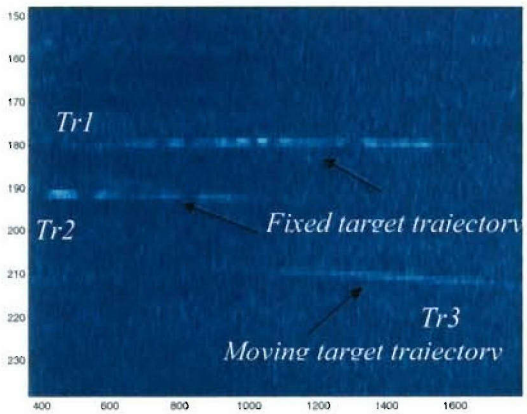

Figure 28: A detail from the target trajectories of Figure 27 showing the |HH| images. The vertical axis represents range bins; the horizontal axis represents azimuth samples.

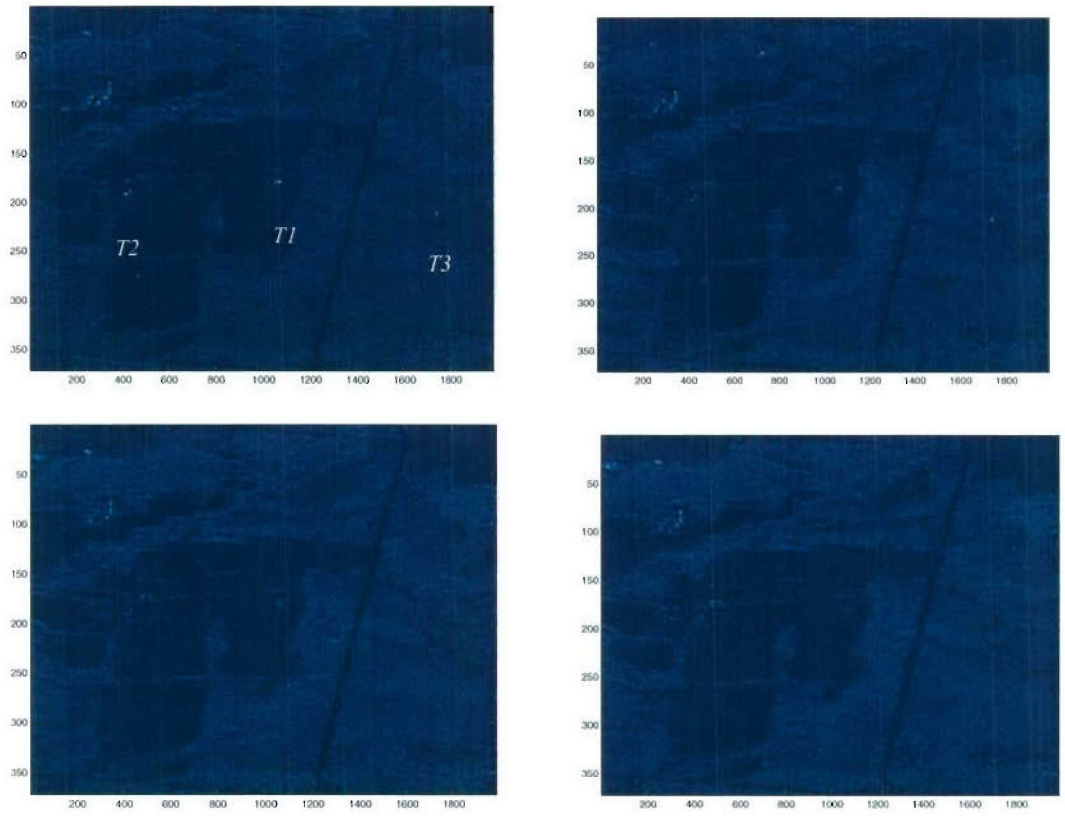

Figure 29: Range and azimuth compressed images of the moving target site in pass 8 from September 24, 2002 trial. Clockwise from top left are the |HH|, |VV|, |VH|, and |HV| images. The bright targets are visible in the |HH| image and are labelled T1 through T3.

Target trajectories can be seen in range compressed images only when the target returns are very strong. For this reason, most moving target trajectories are not visible.

Clutter Cancellation Analysis

The correlation coefficient of between polarization channels indicates the degree of similarity between them. The high correlation leads to substantial cancellation of clutter. The correlation coefficients for this scene are calculated and listed in Table 6, in which, we can see that the correlation coefficient between HV and VH channels is 0.97. The co-registration process compensates for the fact that the HV and VH images are formed at slightly different times ($\Delta t=1/(2xPRF)$)

Table 6: Correlation coefficient for the scene imaged in Figure 27.

	HH	HV	VH	VV
HH	1.00	0.03	0.06	0.37

HV	0.03	1.00	0.97	0.02
VH	0.06	0.97	1.00	0.03
VV	0.37	0.02	0.03	1.00

When |HV−VH| is calculated from the final images, many of them show 4 targets because the surrounding clutter is cancelled. However, they are not on the road and appear to be shifted to the right. Because the trucks were moving away from the aircraft, the images of the trucks should be shifted to the left of the road. However, the targets appear to be the shifted azimuth ambiguities, rather than the images themselves.

An image of |HV−VH| is shown in Figure 30. The image on the right is an enlargement of a portion of the image on the left. The four moving targets are observed and labelled *Tm1* through *Tm4*. The structures of each target mounted on the moving vehicles are shown in Figure 5. *T3* is the only designed moving target observed in |HH| and |VV| images of Figure 29. The structure of this target is a trihedral. The images of the other moving targets can not be seen in the |HH| or |VV| image because the targets are smeared and immersed in the surrounding clutter. However, the targets contain not only the designed reflectors, but also the vehicles themselves, which also produce returns. The normalized scattering matrix of a trihedral is [5]:

$$S = \frac{1}{\sqrt{2}}\begin{bmatrix} 1 & 0 \\ 0 & 1 \end{bmatrix} \tag{34}$$

Four designed moving targets are seen in |HV−VH| image because the clutter level is reduced by cancellation. In the |HV−VH| image, the magnitude of *Tm3* is higher than *Tm2* (*T3* in HH and VV images), but *Tm3* is not seen in |HH| or |VV| image. *Tm3* is a tilted dihedral corner reflector (tilted 45°), which has a strong cross-polarization component. The trihedral theoretically has no cross-polarization components, but there are system imperfections. There are also returns from the vehicle themselves.

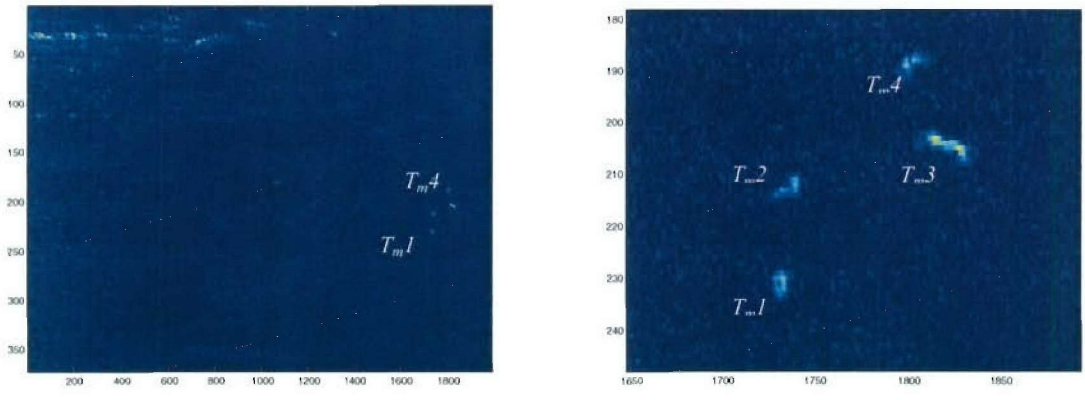

Figure 30: The |HV−VH| image from pass 8. The image on the right is a detail from the image on the left.

The normalized scattering S matrix of a rotated dihedral (diplane) can be deduced as [5]:

$$S = \frac{1}{\sqrt{2}}\begin{bmatrix}\cos\varphi & -\sin\varphi \\ \sin\varphi & \cos\varphi\end{bmatrix}\begin{bmatrix}1 & 0 \\ 0 & -1\end{bmatrix}\begin{bmatrix}\cos\varphi & \sin\varphi \\ -\sin\varphi & \cos\varphi\end{bmatrix} \tag{35}$$

For $\varphi = 45°$, $$S = \frac{1}{\sqrt{2}}\begin{bmatrix}0 & 1 \\ 1 & 0\end{bmatrix} \tag{36}$$

For $\varphi = -45°$, $$S = \frac{1}{\sqrt{2}}\begin{bmatrix}0 & -1 \\ -1 & 0\end{bmatrix} \tag{37}$$

where φ is the orientation angle of the target, i.e. the angle of rotation around the line-of-sight. It is clear that a 45° tilted dihedral has a strong cross-polarization component.

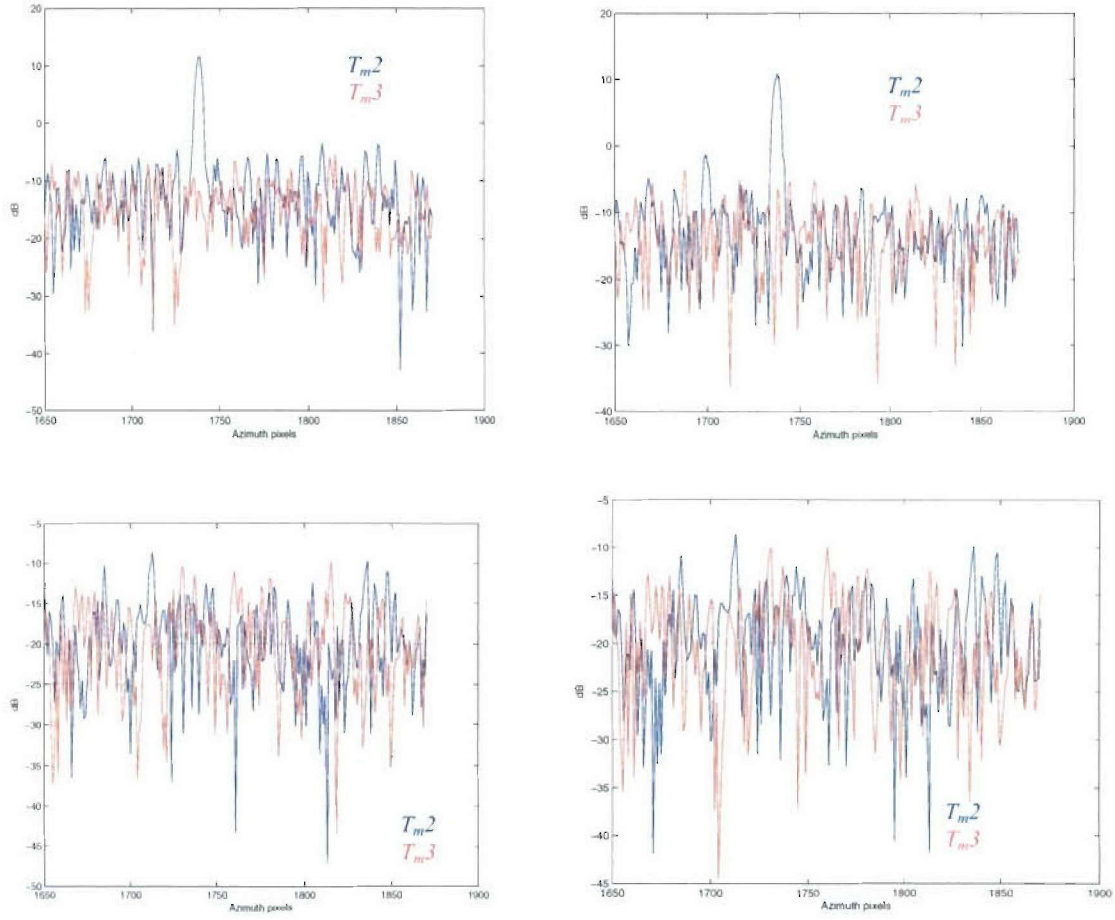

Figure 31: Range line magnitude plot through one of the targets. Clockwise from top left are the |HH|, |VV|, |VH|, and |HV|.

The |HV–VH| image in Figure 30 also shows the distances between the targets: 20 range pixels between *Tm1* and *Tm2* (80 m), 7 between *Tm2* and *Tm3* (28 m) and 17 between *Tm3* and *Tm4* (68 m). The relative order of magnitude of separations estimated from the image are similar to those calculated from dGPS data. The nominal separations were supposed to be 50 m (12.5 range steps).

This analysis can also be verified in the signal plots shown in Figure 31 and Figure 32, which correspond to HH, VV, HV, VH and |HV–VH| respectively. These graphs show *Tm2* and *Tm3*. The range values are 212 for *Tm2* and 202 for *Tm3*, which give the highest returns. For *Tm3*, there is another peak of the same level at range pixel 205. The HH and VV graphs show approximately equal *Tm2* target levels as expected since this a trihedral. The clutter level is –2 to –8 dB. No targets are seen in the HV and VH graphs and the clutter level is –8 to –15 dB. In |HV–VH| graph, *Tm2* and *Tm3* are seen at levels of –12 to –8 dB respectively and the clutter level is –23 to –28 dB.

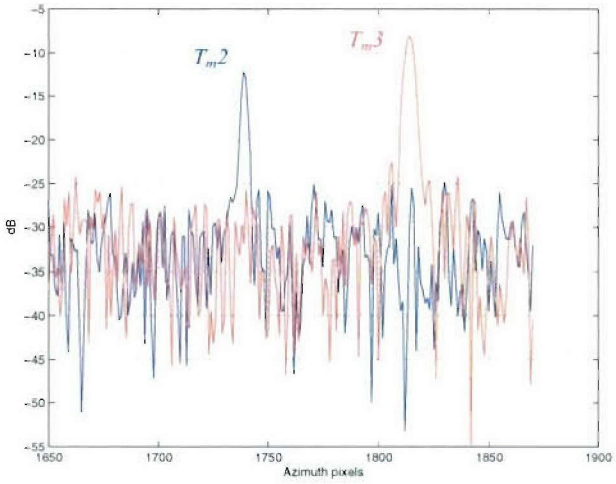

Figure 32: Range line magnitude plot of |HV–VH| through one of the targets.

The targets are moving from the top of the image to the bottom. It is interesting to note that, if the target velocity is constant, the target appears as a vertical smear. If it is accelerating it appears to slope downward and to the left. If it is decelerating, it slopes downward to the right. Thus, *Tm1* seems to have constant velocity. *Tm2* and *Tm4* may be accelerating while Tm3 may be decelerating (perhaps because it is too close to *Tm2*). *Tm3* is also farthest from the road, indicating its velocity is lower. The fact that *Tm3* has 2 peaks may also be consistent with a strong deceleration.

Velocity Analysis

The velocity of the targets can be estimated in at least three ways. The velocity can be estimated from a trajectory analysis. *Tr1* in Figure 27 (*Tm2* in Figure 30) gives a slope from range pixel of 210 to 213, and the azimuth smearing from azimuth pixel of 1200 to 1700. From the total number of smeared azimuth pixels, the time of the moving target can be

estimated (1700–1200)/prf = 1.51 s (where prf is about 332.2 Hz), and the radial velocity can be estimated from the trajectory across the range distance (213–210)*4/1.51 = 7.97 m/s or 28.7 km/h. This gives ground velocity V_{Ty} of 39.2 km/h in the range direction. This is similar to the expected velocity. The results of estimated velocity for each target of each flight pass are presented in Table 7. However, the beginning and the end of the trajectory is not very clear in the image, so the estimation gives only a rough idea of the velocity.

The velocity of the targets can also be estimated by taking advantage of the apparent azimuth shift of the target due to its motions. From the visible images in the images of |HV–VH|, the velocities necessary to shift them back to the road were calculated, assuming that they are ambiguities. All the visible moving targets in the image are actually ambiguities. When the target is shifted due to the movement, the ambiguity is shifted in the same way. Therefore, the velocity of the target can be estimated according to equation (33) and using the simplifying assumption that $v_x << V_a$ and $v_y << V_a$.

An example of key parameters used in calculation of the azimuth shifts are aircraft altitude of 5170 m, aircraft ground speed of 142 m/s and incidence angle Θ of 47°. These parameters were obtained from the flight pass 11p6. However, these parameters are slightly different for each flight pass. We also assume along-track velocity is zero, since the targets were moving away from the aircraft in cross-track. The velocities of targets estimated from the azimuth shift of each flight pass are given in Table 7. The aircraft parameters varied for each flight pass, and were obtained from the aircraft flight log data.

This method appears to provide good estimation of the target radial velocity. However, it is necessary to know the original target location.

The velocity of the targets can also be estimated using a velocity matched filter. SAR processors are usually designed to image static targets. The range compressed data is usually processed by application of an azimuth matched filter. Here, we will use a general velocity matched filter, which is matched to the range history given by equation (30). The velocity matched filter used for this study is given by:

$$H_i = \exp\left[j \frac{4\pi}{\lambda} (R(t_i) - R_0) \right] \tag{38}$$

The time $t = 0$ is defined here as the time at which the target is broadside to the radar. $R_0 = R(0)$ is the slant range at time $t = 0$, $t_i = i/f_p$ (the values of t_i are the sampling instants in "slow time"). f_p is the radar pulse repetition frequency (PRF), and the subscript i indicates the i^{th} radar pulse ($i = 0, \pm1, \pm2, \ldots$). For a static target, $dR/dt = 0$ at $t = 0$. For a moving target, $dR/dt \neq 0$ if the target velocity has a radial component. The range of t_i for this filter is restricted so that $R(t_i)$ values are limited to one range bin. In this case, 200 azimuth samples have been used. In general, for a complete synthetic aperture, range walk would have to be considered [40].

The range compressed data were processed with a matched filter matched to a specific velocity using equation (38). The filter was applied in a trial and error fashion until the correct velocity was approximately determined by maximizing the target amplitude and minimizing the azimuth smearing. Examples of images using matched filter analysis for the HH channel are illustrated in Figure 33 and Figure 34. In Figure 33, the target velocity is assumed to be zero ($V_T = 0$), while in Figure 34, $V_T = 8.8$ m/s (32 km/h). In this case, the target is shifted back to pixel 1837. The approximate road center location from Figure 33 is

1845, which is close to the target location. However, it was observed that it was not always straightforward to determine the maximum amplitude and minimum smearing conditions. The matched filter length should be optimized to minimize this effect.

The PolSAR system also has a number of advantages. Since velocity affects all polarimetric components, velocity information can, in principle, be obtained from any component. In particular, the component with the largest target to clutter ratio can be used to provide the best possible velocity estimate. Single and dual channel spaceborne SAR systems do not have this capability.

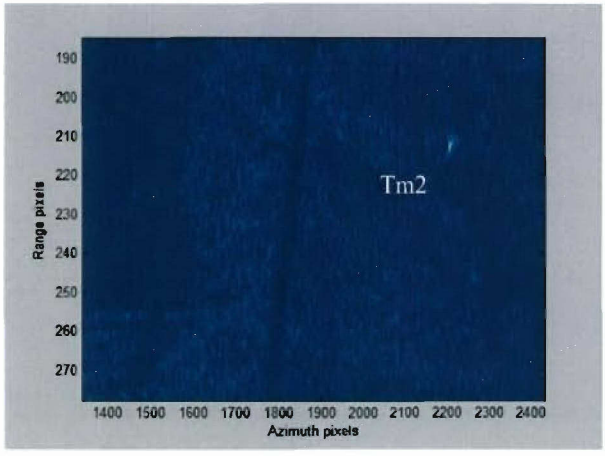

Figure 33: |HH| SAR image (V_{Ty} = 0).

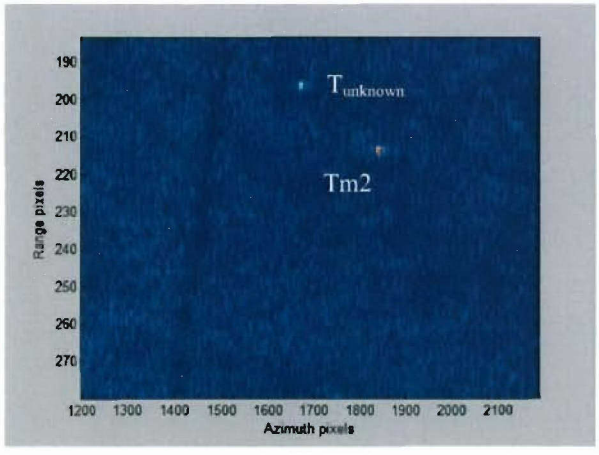

Figure 34: |HH| SAR image (V_{Ty} = 8.8 m/s).

Table 7: Summary of the measured and estimated truck velocities listed by method.

Flight Line / Pass	Target No.	Moving target v_{Ty} (km/h)				
		Designed	dGPS	Trajectory Analysis	Azimuth Shift Analysis	Matched Filter
l1p2	1 (grid)	35	31		32	31
	2 (trihedral)		31	29	31	31
	3 (dihedral)		32		34	32
	4 (dihedral)		33		34	33
l1p3	1	20	21		23	21
	2		20		23	20
	3		23		26	23
	4		22		23	22
l1p4	1	30	29		30	29
	2		29	30	30	29
	3		31		33	31
	4		30		31	30
l1p5	1	35	34		34	34
	2		31	28	33	31
	3		37		38	37
	4		35		35	35
l1p6	1	20	20		22	20
	2		21	22	23	21
	3		23		25	23
	4		20		23	20
l1p8	1	35	32		33	32
	2		32	39	33	32
	3		29		31	29
	4		31		32	31

Recommendations for future work

Due to time constraints and the departure of some key personnel involved with this project, only a portion of the CV-580 repeat-pass polarimetric data collected was processed and analyzed. Eight repeat-pass polarimetric flight lines were collected over Valcartier, Quebec, on September 7, 2001. None of these data have been reviewed to date. Only a limited number of scenes from the Ottawa and Petawawa Pol-InSAR collect have been fully explored. A second moving target experiment held in Petawawa on June 8, 2002 also awaits analysis.

There will be many opportunities to collect Pol-InSAR data from space in the near future. PALSAR is scheduled for launched in the fall of 2005. Its polarimetric L-band sensor will be capable of repeat-pass interferometry. Currently RADARSAT-2 is scheduled for launched in the spring of 2006. Its polarimetric C-band sensor will also be capable of repeat-pass interferometry.

The long wavelength (L-band) of PALSAR has several key advantages with regards to Pol-InSAR compared with the shorter wavelength (C-band) of RADARSAT-2. At L-band volume decorrelation is reduced, thereby increasing the likelihood of coherence between the long interval that makes up repeat-pass interferometric pair. The lower volume decorrelation also makes it a good candidate for biomass estimation and for detection of scatterers beneath the forest cover.

Urban environments and man-made structure characterization would benefit most from high-resolution sensors. The polarimetric mode on RADARSAT-2 has a higher resolution than PALSAR, and therefore will be more suitable for urban characterization. But its 9-meter resolution is still not quite sufficient for characterization of small man-made structures.

Further research and development into tools designed for exploitation of satellite repeat-pass Pol-InSAR would be beneficial. Specifically, applications may include detection of scatterers hidden beneath the forest canopy using PALSAR and characterization of the urban and semi-urban environments using RADARSAT-2.

Summary and Conclusion

Polarimetric SAR interferometry (Pol-InSAR) combines the technologies of polarimetric SAR and interferometric SAR, enabling applications that neither can achieve alone. Pol-InSAR can be used to differentiate scatterers within a single footprint or within a layover region based on their polarimetric signature and height above the terrain. It has been used, in an experimental setting, for tree height calculation, biomass estimation, and detection as well as characterization of scatterers hidden by a forest canopy, measurement of bare earth topography in forested terrain, among others. It can also potentially be useful to help urban building and manmade structure characterization. Recent articles have shown that forest height determination and biomass estimation can potentially be accomplished using a dual-mode Pol-InSAR, though full-mode Pol-InSAR provides for greater accuracy and sensitivity.

The method by which PolSAR normally collects data creates a synthetic along-track InSAR baseline between the HV (H transmit and V receive) and VH channels. This can be potentially exploited for target velocity detection and estimation. This provides a potential means of velocity estimation within a regular polarimetric data collect.

Pol-InSAR applications are highly dependent on the sensor characteristics. Unfortunately, the CV-580 radar sensor is not an optimal sensor for Pol-InSAR application exploitation due to the combination of its C-band wavelength and relatively low resolution. Long wavelength L-band Pol-InSAR sensors may be best suited for forest height determination or biomass estimation, since these applications are dependent on scattering from several layers of the forest including small branches, tree trunks and the forest floor. Urban and man-made structure characterization benefits most from high-resolution sensors. The large swath that low-resolution sensors provide may best suite distributed target applications.

Pol-InSAR also unfortunately has the technological challenges of both PolSAR and InSAR. Accurate polarimetric calibration is a necessity. Satellite polarimetric data can be subject to Faraday rotation effects. Ionospheric and tropospheric effects can degrade satellite interferometry. InSAR also requires a suitable baseline for phase to height conversion. Repeat-pass InSAR is subject to temporal decorrelation. Only within the past year has a sensor become available that is capable of single-pass Pol-InSAR.

With the advent of RADARSAT-2 PolSAR, access to PolSAR repeat-pass InSAR data will become much more readily available. In the horizon 2 or 3 timeframe, the Sarlupe or a cartwheel constellation of SAR satellites could be a source of single-pass Pol-InSAR data (in either polarimetric or dual-pol mode).

References

1. Alberga, V. Chandra, M. and Papathanassiou, S.R., "An analysis of volume decorrelation in polarimetric SAR interferometry," 4th *European Conference on Synthetic Aperture Radar (EUSAR)*, Cologne, Germany, June 4-6, 2002.

2. Ballester-Berman, J.D., and Lopez-Sanchez, J.M., "Retrieval of height and topography of corn fields by polarimetric SAR interferometry," *IGARSS'04*, Toulouse, France, August, 2004.

3. Bamler, R. and Hartl, P., "Synthetic aperture radar interferometry," *Inverse Problems*, vol. 14, pp. R1-R54, 1998.

4. Brennan, D.G., "Linear diversity combining techniques", *Proceedings of IEEE*, vol. 91, no. 2, Feb. 2003, pp 331-356.

5. Cameron, W.L. and Youssef, N.N., "Simulated polarimetric signatures of primitive geometrical shapes", *IEEE Trans. Geosc. & Rem. Sens.*, vol. 34, no. 3, May 1996.

6. Campbell, J.W.M., Gray, A.L., Mattar, K.E., Clarke, J.H., and van der Kooij, M. W.A., "Ocean surface feature detection with the CCRS along-track InSAR,". *Canadian Jr. of Rem. Sens.*, vol. 23, no. 1, pp. 24-37, 1997.

7. Cloude, S.R., Corr, D., Williams, M, "FOPEN using polarimetric SAR interferometry," *EUSAR '04*, pp. 255, Ulm, Germany, May 25-27, 2004.

8. Cloude, S.R., "Robust parameter estimation using dual baseline polarimetric SAR interferometry," *IGARSS '02*, Toronto, Ontario, Canada, June 24-28, 2002.

9. Cloude, S.R. and Papathanassiou, K.P., "A 3-stage inversion process for polarimetric SAR interferometry," 4th *European Conference on Synthetic Aperture Radar (EUSAR)*, Cologne, Germany, June 4-6, 2002.

10. Cloude, S.R., Papathanassiou, K.P., Reigber, A. and Boerner, W.M., "Multi-frequency polarimetric SAR interferometry for vegetation structure extraction," *IGARSS '00*, Honolulu, Hawaii, USA, July 24-26, 2000.

11. Cloude, S.R. and Papathanassiou, K.P., "Polarimetric SAR interferometry", *IEEE Trans. Geosc. & Rem. Sens.*, vol. 36, no. 5, pp. 1551 to 1565, 1998.

12. Cloude, S.R. and Pottier, E., "An Entropy based classification scheme for land applications of Polarimetric SAR," *IEEE Trans. Geosc. & Rem. Sens.*, vol 35, no 1, pp. 68-78, 1997.

13. Cloude, S.R. and Papathanassiou, K.P., "Coherence optimisation in polarimetric SAR interferometry," *IGARSS '97*, Singapore, August 3-8, 1997.

14. Cloude, S.R. and Pottier, E., "A review of target decomposition theorems in radar polarimetry," *IEEE Trans. Geosc. & Rem. Sens.*, vol. 34, no. 2. pp. 498-518, 1996.

15. Colin, E., Titin-Scnaider, C. and Tabbara, W., "Investigation on different interferometric coherence optimization methods," *POL-INSAR Workshop*, http://earth.esa.int/polinsar, Frascati, Italy, January 14-16, 2003.

16. Corr, D.G., Cloude, S.R., Ferro-Famil, L., Hoekman, D.H., Partington, K., Pottier, E. and Rodrigues, A., "A review of the applications of SAR polarimetry interferometry – An ESA funded study," *POL-INSAR Workshop*, http://earth.esa.int/polinsar, Frascati, Italy, 14-16 January 2003.

17. Curlander, J.C., McDonough, R.N., "Synthetic aperture radar – systems and signal processing," John Wiley & sons, Inc. 1991.

18. Dubois-Fernandez, P., Dupuis, X., Garestier, F. and Paillou, P., "Using Pol-INSAR at X-band: preliminary observations," *POL-INSAR Workshop*, http://earth.esa.int/polinsar, Frascati, Italy, 14-16 January 2003.

19. Emporus, http://www.emporis.com/en/wm.

20. Freeman, A. and Dobson, M., "A three-component scattering model for polarimetric SAR data," *IEEE Trans. Geosc. & Rem. Sens.*, vol. 36, pp. 963-973, May 1998.

21. Gatelli, F., Guarnieri, A. M., Parizzi, F., Pasquali, P., Pratti, C. and Rocca, F., "The wavenumber shift in SAR interferometry," *IEEE Trans. Geosc. & Rem. Sens.*, vol. 32, no. 4, pp. 855-865, July 1994.

22. Gray, A.L. and Farris-Manning, P., "Repeat-pass interferometry with airborne synthetic aperture radar," *IEEE Trans. Geosc. & Rem. Sens.*, vol. 31, no. 1, pp. 181-191, January 1993.

23. Guillaso, S., Ferro-Famil, L., Reigber, A., and Pottier, E., "Building characterisation using polarimetric interferometric SAR data," EUSAR 2004, Ulm, Germany, pp. 407-410, May 25-27, 2004.

24. Hajnsek, I., Alvarez-Perez, J.-L., Papathanassiou, K.P., Moreira, A. and Cloude, S.R., "Surface parameter estimation using interferometric coherences at different polarisations," *POL-INSAR Workshop*, http://earth.esa.int/polinsar, Frascati, Italy, January 14-16, 2003.

25. Hajnsek I., Papathanassiou, K.P., Moreira, A. and Cloude, S.R., "The potential of surface parameter estimation from interferometric SAR," 4th *European Conference on Synthetic Aperture Radar (EUSAR)*, Cologne, Germany, June 4-6, 2002.

26. Hawkins, R.K., Touzi, R. and Livingstone, C., "Calibration and use of CV-580 airborne polarimetric SAR data,"*Proc. 4th International Airborne Rem. Sens. Conference and Exhibition, 21st Can. Symp. Rem. Sens.*, vol 2, II.32-II.40, 1999.

27. Henry, C. , Souyris, J.C., Adragna, F., and Marthon, P., "On the use of SAR image spectral analysis for target and change detection. Assessment in the case of natural risks monitoring," *Proc. 8th Int. Symp. RemoteSensing, Toulouse*, France, Sept. 2001.

28. Hoekman, D.H., "A new polarimetric classification approach evaluated for agricultural crops," *POL-INSAR Workshop*, http://earth.esa.int/polinsar, Frascati, Italy, January 14-16, 2003.

29. Hoen, E.W. and Zebker, H.A., "Penetration depths inferred from interferometric volume decorrelation observed over the Greenland ice sheet", *IEEE Trans. Geosc. & Rem. Sens*, vol. 38, no. 6, pp. 2571-2581, November 2000.

30. Horn, R., Scheiber, R., Buckreuss, St., Zink, M., and Moreira, A, "E-SAR generates level-3 SAR products for ProSmart," *IGARSS'99*, Hamburg, Germany, June 28 to July 2, 1999.

31. Huynen, J.R., "Phenomenological theory of radar targets," Ph.D. Thesis, P.Q. Research, Polarimetric Quest, Los Altos Hills, Ca, USA, pp. 216, 1987.

32. Jackson, J.D., "Classical electrodynamics", Third Edition, John Wiley & Sons, NY, 1999.

33. Kimura, H., Papathanassiou P., Hajnsek, I, "Polarization Orientation Effects in Urban Area on SAR Data," *IGARSS '05*, Seoul, Korea, July 25-29, 2005.

34. Können, G.P., Polarized light in nature, Cambridge University Press, Cambridge, UK, 1985.

35. Krogager, E. and Boerner, W-M., "On the importance of utilizing complete polarimetric information in radar imaging and classifications," *AGARD Symposium: Remote Sensing – A valuable source of information*, AGARD Proc. , 528, Toulouse, France, April 22-25, 1996, pp. 17-1 to17-12.

36. Lee, J.S., Cloude, S.R., Grunes, M.R. and Papathanassiou, K.P., "Speckle filtering of polarimetric SAR interferometry data," *POL-INSAR Workshop*, http://earth.esa.int/polinsar, Frascati, Italy, January 14-16, 2003.

37. Lee, J.S., Cloude, S.R., Papathanassiou, K.P., Grunes, M.R., Ainsworth, T.L. and Schuler D.L., "Speckle filtering of polarimetric SAR interferometry data," *IGARSS '02*, Toronto, Ontario, Canada, June 24-28, 2002.

38. Lee, J.-S., Grunes, M., Ainsworth, T., Du, L.-J., Schuler, D. and Cloude, S., "Unsupervised classification using polarimetric decomposition and the complex Wishart classifier," *IEEE Trans. Geosc. & Rem. Sens.*, vol. 37, pp. 2249-2258, September 1999.

39. Lee, J.S., Hoppel, K.W., Mango, S.A. and Miller, A.R., "Intensity and phase statistics of multiLook polarimetric and interferometric SAR imagery," *IEEE Trans. Geosc. & Rem. Sens*, Vol. 32, pp. 1017-1028, 1994.

40. Livingstone, C. E. and Sikaneta, I., "Focusing moving targets – Terrain imaged with moving-target matched filters: A tutorial", (DRDC Ottawa TN 2004-160). Defence R&D Canada – Ottawa.

41. Livingstone, C.E., Gray, A.L., Hawkins, R.K., Vachon, P., Lukowski, T.I., and Lalonde, M, "The CCRS airborne SAR systems: radar for remote sensing research," *Canadian Jr. of Rem. Sens.*, Vol. 21, No. 4, pp 468—491, 1995.

42. Lukowski, T., Yue, B., and Mattar, K., "Synthetic aperture radar for search and rescue polarimetry and interferometry," *IGARSS'04*, Toulouse, France, August, 2004.

43. Massmann, F.-H., Neumayer, J. C., Raimondo, K., Enninghorst, K. and Li, H., "Quality of the D-PAF orbits before and after the inclusion of PRARE data," in *Proc. 3rd ERS Symp.: Space at the Service of our Environment*, vol. 3, Florence, Italy, pp. 1655–1660, March 1997.

44. Mattar, K. and Gray, A.L., "Reducing ionospheric electron density errors in satellite radar interferometry applications," *Canadian Jr. of Rem. Sens.*, vol. 28, no. 4, pp. 593-600, 2002.

45. Mattar, K., Gray, A.L., Geudtner, D. and Vachon, P.W., "Interferometry for DEM and terrain displacement: effects of inhomogeneous propagation," *Canadian Jr. of Rem. Sens.*, vol. 25, no. 1, pp. 60-69, March 1999.

46. Mattar, K., Yeremy and M., Livingstone, C., "Polarimetric interferometic SAR: literature review and an assessment of its utility for DND," (DRDC Ottawa TN 2003-144). Defence R&D Canada – Ottawa,.2003.

47. Mattar, K., Gallop, L. and Lang., J., "Alert 2002 ground truth missions for Arctic shoreline delineation and feature extraction," (DRDC Ottawa TM 2002-147), Defence R&D Canada – Ottawa, 2002.

48. Mattar, K., Buchheit, M. and Beaudoin, A., "Shoreline mapping using interferometric SAR", (DREO TR 2001-078), Defence Research Establishment Ottawa, 2001.

49. Moccia, A., and Rufin, G., "Spaceborne along-track SAR interferometry: Performance analysis and mission scenarios," *IEEE Transactions on Aerospace and Electronic Systems*, vol. 37, pp. 199–213, 2001.

50. Mohr, J.J. and Madsen, S.N., "Geometric calibration of ERS satellite SAR images", *IEEE Trans. Geosc. & Rem. Sens.*, vol. 39, no., 4, pp. 842-840, April 2001.

51. Moreira, A., "Real-time synthetic aperure radar (SAR) processing with a new subaperture approach," *IEEE Trans. Geosc.& Rem. Sens.*, vol. 30, pp. 714-722, July 1991.

52. Papathanassiou, K.P., Hajnsek, I., Moreira, A., Cloude, S.R., "Forest parameter estimation using a passive polarimetric microsatellite concept," 4th *European*

Conference on Synthetic Aperture Radar (EUSAR), Cologne, Germany, June 4-6, 2002.

53. Papathanassiou, K.P., Hajnsek, I., Moriera, A., Cloude, S.R., "Forest parameter estimation using a passive polarimetric microsatellite concept," *IGARSS '02*, Toronto, Ontario, Canada, June 24-28, 2002.

54. Papathanassiou, K.P. and Cloude, S.R., "Single-baseline polarimetric SAR interferometry", *IEEE Trans. Geosc. & Rem. Sens.*, vol. 39, no 11. pp. 2352–2363, 2001.

55. Papathanassiou, K.P., Cloude, S.R., Reigber, A. and Boerner, W.M., "Multi-baseline polarimetric SAR interferometry for vegetation parameters estimation," *IGARSS '00*, Honolulu, Hawaii, USA, July 24-28, 2000.

56. Papathanassiou, K.P., Reigber, A. and Cloude, S.R., "Vegetation and ground parameter estimation using polarimetric interferometry part I: The role of polarisation," *CEOS SAR Workshop*, Toulouse, France, October 26-29, 1999.

57. Papathanassiou, K.P., "Polarimetric SAR interferometry," Doctoral Thesis, Technische Universität Graz, DLR-Forschungsbericht 99-07, Germany, 1999.

58. Papathanassiou, K.P., Reigber, A. and Cloude, S.R., "Vegetation and ground parameter estimation using polarimetric interferometry part II: parameter inversion and optimal polaisation," *CEOS SAR Workshop*, Toulouse, France, October 26-29, 1999.

59. Papathanassiou, K.P. and Cloude, S.R., "Phase decomposition in polarimetric SAR interferometry," *IGARSS '98*, Seattle, USA, July 6-10, 1998.

60. Papathanassiou, K.P., Reigber, A., Scheiber, R., Horn, R. Moreira, A. and Cloude, S.R., "Airborne polarimetric SAR interferometry," *IGARSS '98*, Seattle, USA, July 6-10, 1998.

61. Papathanassiou, K.P. and Cloude, S.R., "Polarimetric effects in repeat-pass SAR interferometry," *IGARSS '97*, Singapore, August 3-8, 1997.

62. Papathanassiou, K.P., Cloude, S.R. and Coltelli, M., "On the interferometric coherence: A multifrequency and multitemporal analysis," *ESA Workshop on Applications of ERS SAR Interferometry*, University of Zurich, Switzerland, Sep 30 – Oct 2, 1996.

63. Papathanassiou, K.P. and Moreira, J.R., "Interferometric analysis of multifrequency and multipolarizaiton SAR data," *IGARSS '96*, Lincoln, Nebraska, May 27-31, 1996

64. Pottier, E., "On Dr. J.R. Huynen's main contributions in the development of polarimetric radar techniques, and how the 'radar targets phenomenological concept' becomes a theory," *SPIE* vol. 1748, Radar Polarimetry, pp 72-85, 1992.

65. Pottier, E., "Unsupervised classification scheme and topography derivation of polsar data based on the h/z/α polarimetric decomposition theorem," *Proc. 44rth Int. Radar Polarimetry, PIERS '98*, pp. 535-548, 1998.

66. Quegan, S., Le Toan, T.L., Skriver, H., Gomez-Dans, J., Gonzalez-Sampedro, M.C. and Hoekman, D.H., "Crop classification with multitemporal polarimetric SAR data," *POL-INSAR Workshop*, http://earth.esa.int/polinsar, Frascati, Italy, January 14-16, 2003.

67. Reigber, A., "First demonstration of airborne SAR tomography using multibaseline L-band data," *IEEE Trans. Geosc. & Rem. Sens.*, vol. 38, no. 5, pp. 2142-2152, September 2000.

68. Rosen, P.A., Hensley, S. and Joughin, I.R., Li, F.K., Madsen, S.N., Rodriguez, E. and Goldstein, R.M., "Synthetic aperture radar interferometry," *Proc. IEEE*, vol. 88, no. 3, pp.332-381, March 2000.

69. Rufenacht, H., Proulx, R.J. and Cefola, P.J., "Improvement of RADARSAT image localization," *The International Symposium on Geomatics in the Era of RADARSAT (GER '97)*, Ottawa, Canada, May 25-30, 1997.

70. Santoro, M. *et al.*, " Monitoring urban areas by means of coherence levels", *ESA FRINGE '99 Conference Proceedings* (see http://www.esa.int/fringe99), 1999.

71. Scheiber, R. and Moriera, A., "Coregistration of interferometric SAR images using spectral diversity," *IEEE Trans. Geosc. & Rem. Sens.*, vol. 38, no. 5, pp. 2179-2190, September 2000.

72. Scheiber, R., Reigber, A., Ulbricht, A., Papathanassious K.P., Horn, R., Buchreub, S., and Moriera, A., "Overview of interferometric data acquisition and processing modes of the experimental airborne SAR system of DLR," Proc. Of IGARSS'99, pp. 35-37, Hamburg, 1999.

73. Secker, J., English, R., Yeremy, M. and Lévesque, J., "CAMEVAL-2002 land forces signature reduction trials: ground truthing, calibration and mutli-sensor data acquisition for DRDC experiments," *DRDC Technical Memorandum*, DRDC Ottawa TM 2002-121.

74. SkyscraperPage, http://www.skyscraperpage.com.

75. Soumekh, M., "Moving target detection in foliage using along-track monopulse synthetic aperture radar imaging," *IEEE Transactions on Image Processing*, Vol. 6, pp. 1148–1163, 1997.

76. Stockburger, E.F., and Held, D.N., "Interferometric moving ground target imaging," *IEEE international radar conference*, 1995, pp. 438–443.

77. Swartz, A.A., Yuen, H.A., Kong, J.A., Novak, L.M. and Shin, R.T., "Optimal polarizations for achieving maximum contrast in radar images," *J.Geoghr.Res.*, vol. 93, no. B13, pp. 15252-15260, 1988.

78. Tarayre-Oriot, H. and Massonnet. D., "Atmospheric artifacts on interferograms," *ESA FRINGE'96 Conference Proceedings* (see http://www.geo.unizh.ch/rsl/fringe96/) 1996.

79. Touzi, R., "Calibrated polarimetric SAR data for ship detection," *IGARSS'00*, Honolulu, Hawaii, 24-28 July 2000.

80. Treuhaft, R.N. and Siqueira, P.R., "Vertical structure of vegetation land surfaces from interferometric and polarimetric radar," *Radio Science*, vol. 35, no. 1, pp. 141-177, January-February, 2000.

81. Ulaby, F.T., Moore, R.K. and Fung, A.K., "Microwave remote sensing, active and passive, volume II: radar remote sensing and surface scattering and emission theory," Ch. 11, Addison-Wesley, Reading MA, 1982.

82. Ulbricht, A., Papathanassiou. K.P. and Cloude, S.R., "Polarimetric analysis of SAR-Interferograms in L- and P-band," *IGARSS '98*, Seattle, USA, July 6-10, 1998.

83. van Zyl, J.J, "Unsupervised classification of scattering behavior using radar polarimetry data," *IEEE Trans. Geosci. And Remote Sensing*, vol. 27, pp. 36-45, 1989.

84. Wang, G., Xia, X.G., Chen, V.C., "Radar imaging of moving targets in foliage using multifrequency multiaperture polarimetric SAR," *IEEE Trans. Geosci. And Remote Sensing*, Vol. 41, pp. 1755-1764, 2003.

85. Yeremy, M., Livingstone, C., Mattar, K., Gallop L., Lang, J. and Beaudoin A., "Polarimetric interferometry experiment trials for years 2001 and 2002: Experiment design, ground truthing, data quality and analysis," (DRDC TN 2003-142), Defence R&D Canada – Ottawa, 2003.

86. Zandoná Schneider, R., Liseno, A., Papathanassiou, K.P., and Hajnsek I., "Polarimetric SAR interferometry over urban areas: First results," *EUSAR 2004,* Ulm, Germany, pp. 755-759, May 25-27, 2004.

87. Zebker, H.A., and Van Zyl, J.J., "Imaging radar polarimetry: a review," Proceedings of the IEEE, Vol. 79, pp. 1583-1606, 1991.

88. Zebker, H.A., Van Zyl, J.J., Durden, S.L. and Norikane, L., "Calibrated imaging radar polarimetry: Technique, Examples, and Applications," IEEE Trans. Geosci. Remote Sensing, Vol. 29, pp. 942-961, 1991.

89. Zebker, H.A., van Zyl, J.J. and Held, D.N., "Imaging radar polarimetry from wave synthesis," *J. Geophys. Res.*, vol. 92, pp. 683-701, 1986.

List of symbols/abbreviations/acronyms/initialisms

ARC	Active Radar Calibrator
BSA	Back Bistatic Scattering Alignment
CAMEVAL	CAMouflage EVALuation
CCRS	Canada Centre Remote Sensing
CF	Canadian Forces
CFB	Canadian Forces Base
CR	Corner Reflector
CSA	Canadian Space Agency
CV	Convair
DEM	Digital Elevation Model
dGPS	Differential Global Positioning System
DND	Department of National Defence
DPCA	Displaced Phase Center Antenna
DRDC	Defence Research and Development Canada
DREO	Defence Research Establishment Ottawa
DREV	Defence Research Establishment ValCartier
EC	Environment Canada
EM	Electromagnetic
ERS	European Remote Sensing
ESA	European Space Agency
GCP	Ground Control Point
GMTI	Ground Moving Target Indicator
HAE	Height above the ellipse
HAG	Height above the ground
INS	Inertial Navigation System
InSAR	Interferometric SAR
Mocomp	Motion Compensation
MSL	Mean Sea Level
PALSAR	Phased Array type L-band SAR
PFC	Pacific Forestry Centre
Pol-InSAR	Polarimetric Interferometric SAR
PolSAR	Polarimetric SAR
PRF	Pulse Repetition Frequency
QC	Quality Control
RCS	Radar Cross Section
SAR	Synthetic Aperture Radar
SCR	Signal to Clutter Ratio
SLC	Single Look Complex
SRI	Satellite Radar Interferometry
TCR	Target-to-Clutter Ratio
TIF	Technology Investment Fund
UTM	Universal Transverse Mercator
WGS	World Geodetic System

DOCUMENT CONTROL DATA

(Security classification of title, body of abstract and indexing annotation must be entered when the overall document is classified)

1. ORIGINATOR (the name and address of the organization preparing the document. Organizations for whom the document was prepared, e.g. Establishment sponsoring a contractor's report, or tasking agency, are entered in section 8.)

Defence R&D Canada – Ottawa
Ottawa, Ontario, Canada K1A 0K2

2. SECURITY CLASSIFICATION (overall security classification of the document, including special warning terms if applicable)

UNCLASSIFIED

3. TITLE (the complete document title as indicated on the title page. Its classification should be indicated by the appropriate abbreviation (S,C or U) in parentheses after the title.)

Polarimetric SAR Interferometry: Investigations using EC CV-580 SAR data (U)

4. AUTHORS (Last name, first name, middle initial)

Mattar, Karim E., Liu, Chen, Sabry, Ramin

5. DATE OF PUBLICATION (month and year of publication of document)	6a. NO. OF PAGES (total containing information. Include Annexes, Appendices, etc.)	6b. NO. OF REFS (total cited in document)
March 2005	90	89

7 DESCRIPTIVE NOTES (the category of the document, e.g. technical report, technical note or memorandum. If appropriate, enter the type of report, e.g. interim, progress, summary, annual or final. Give the inclusive dates when a specific reporting period is covered.)

Technical Report

8. SPONSORING ACTIVITY (the name of the department project office or laboratory sponsoring the research and development. Include the address.)

DRDC Ottawa, DND

9a. PROJECT OR GRANT NO. (if appropriate, the applicable research and development project or grant number under which the document was written. Please specify whether project or grant)	9b. CONTRACT NO. (if appropriate, the applicable number under which the document was written)
15es21	

10a. ORIGINATOR'S DOCUMENT NUMBER (the official document number by which the document is identified by the originating activity. This number must be unique to this document.)	10b. OTHER DOCUMENT NOS. (Any other numbers which may be assigned this document either by the originator or by the sponsor)
DRDC Ottawa TR 2005-165	

11 DOCUMENT AVAILABILITY (any limitations on further dissemination of the document, other than those imposed by security classification)

(x) Unlimited distribution
( ) Distribution limited to defence departments and defence contractors; further distribution only as approved
( ) Distribution limited to defence departments and Canadian defence contractors; further distribution only as approved
( ) Distribution limited to government departments and agencies; further distribution only as approved
( ) Distribution limited to defence departments; further distribution only as approved
( ) Other (please specify):

12. DOCUMENT ANNOUNCEMENT (any limitation to the bibliographic announcement of this document. This will normally correspond to the Document Availability (11). However, where further distribution (beyond the audience specified in 11) is possible, a wider announcement audience may be selected.)

13. ABSTRACT (a brief and factual summary of the document. It may also appear elsewhere in the body of the document itself. It is highly desirable that the abstract of classified documents be unclassified. Each paragraph of the abstract shall begin with an indication of the security classification of the information in the paragraph (unless the document itself is unclassified) represented as (S), (C), or (U). It is not necessary to include here abstracts in both official languages unless the text is bilingual).

This study examines the potential applications of polarimetric SAR interferometry (Pol-InSAR). Pol-InSAR is a new and unique methodology that combines the resources of polarimetric synthetic aperture radar (PolSAR) for target classification with the capability of interferometric SAR (InSAR) for height discrimination. In this report, the Pol-InSAR literature is reviewed. Two field trials in Ottawa and Petawawa are described that collected Pol-InSAR data in 2002 using the Environment Canada's Convair-580 in repeat-pass mode. Calibration and processing of the data are detailed. Finally data analysis and potential application are discussed, particularly in view to the upcoming RADARSAT-2 and PALSAR missions. (U)

14. KEYWORDS, DESCRIPTORS or IDENTIFIERS (technically meaningful terms or short phrases that characterize a document and could be helpful in cataloguing the document. They should be selected so that no security classification is required. Identifiers such as equipment model designation, trade name, military project code name, geographic location may also be included. If possible keywords should be selected from a published thesaurus. e.g. Thesaurus of Engineering and Scientific Terms (TEST) and that thesaurus-identified. If it is not possible to select indexing terms which are Unclassified, the classification of each should be indicated as with the title.)

Pol-InSAR
Polarimetric Radar Interferometry
Polarimetric Interferometry
Polarimetry SAR
Interferometry SAR
Coherence

Defence R&D Canada

Canada's Leader in Defence
and National Security
Science and Technology

R & D pour la défense Canada

Chef de file au Canada en matière
de science et de technologie pour
la défense et la sécurité nationale

www.drdc-rddc.gc.ca